



**HAL**  
open science

# Electronic structure and magnetism of transition metal oxides : the case of Fe<sub>3</sub>O<sub>4</sub>

Weimin Wang

► **To cite this version:**

Weimin Wang. Electronic structure and magnetism of transition metal oxides : the case of Fe<sub>3</sub>O<sub>4</sub>. Other [cond-mat.other]. Université de Cergy Pontoise, 2012. English. NNT : 2012CERG0608 . tel-00841671

**HAL Id: tel-00841671**

**<https://theses.hal.science/tel-00841671>**

Submitted on 27 Nov 2014

**HAL** is a multi-disciplinary open access archive for the deposit and dissemination of scientific research documents, whether they are published or not. The documents may come from teaching and research institutions in France or abroad, or from public or private research centers.

L'archive ouverte pluridisciplinaire **HAL**, est destinée au dépôt et à la diffusion de documents scientifiques de niveau recherche, publiés ou non, émanant des établissements d'enseignement et de recherche français ou étrangers, des laboratoires publics ou privés.

# THÈSE

Pour obtenir le titre de  
Docteur de l'Université de Cergy-Pontoise  
(Spécialité : physique)  
présentée par

**Weimin WANG**

Electronic structure and magnetism  
of transition metal oxides: the case of  $\text{Fe}_3\text{O}_4$

**Thèse soutenue le 28 septembre 2012 devant le jury composé de :**

<b>M. Eric Beaurepaire</b>	<b>Président</b>
<b>M. Yves Dumont</b>	<b>Rapporteur</b>
<b>M. Januze Kanski</b>	<b>Rapporteur</b>
<b>Mme. Christine Richter</b>	<b>Examineur</b>
<b>M. Nick Barrett</b>	<b>Examineur</b>
<b>M. Karol Hricovini</b>	<b>Directeur de thèse</b>

# Acknowledgement

When I was still a college student in physics, I never thought that I would do research work. But now I am thinking to do it as a career for my whole life. This significant change occurred in the recent four years that I have spent in France.

Looking at the word “Acknowledgement”, there are many people coming into my mind. First of all, I would like to show my sincere appreciation to my supervisor, Karol Hricovini. Thank him for giving me the opportunity to work on this interesting project of thesis; thank him for continuous help and support during the last four years, especially on the writing of thesis and paper; thank him for the kind help in my life in the difficult period when I just arrived in France without any knowledge of French.

I have majored in optical engineering when I was in Shanghai. My experience in advanced experimental techniques was a piece of white paper. I am grateful to Olivier Heckmann, Cephise Cacho and the scientists in Elettra and Max-Lab for their patient explanation that gave me the basic knowledge of laser system, UHV techniques, ARPES and SRPES etc.

I also had a lot useful discussion with Juraj Krempasky in the data simulation and experimental ideas. The theoretical calculation came from Peter Blaha, based on which I could do my simulation work.

A special thanks goes to Jean-Michel Mariot, Christine Richter and Paola De Padova for their help in paper writing and publication.

I am also grateful to the jury members for spending the time reading my thesis during the vacation and for their interest in the work.

Last but not least, I would like to thank Prof. Wang Zhanshan for giving me the opportunity to study in France.

There is an old precept in China: Never be far away from your parents. I have been in France for four years. I spent little time with my family. At this moment of my first achievement in my life, I would like to tell my mother and father: I love you all the time.

My ability of English may hold back my genuineness. Please allow me to use my mother language to express my gratitude to all of you.

## 致谢：

当我还是一名本科生的时候，我从未想过有一天能够有机会获得博士学位，而现在我终于完成了我的博士论文。这将是人生第一个成就。我要感谢所有在此期间帮助过我的人。

首先，我必须向我的导师，Karol Hricovini 教授表达我最诚挚的谢意。正是他不断地鼓励和帮助才促使我完成了博士期间的工作以及论文的写作。更令我感激的是，Karol 在生活上给予我的帮助，尤其是在最初的一段语言不通的时期，让我摆脱了手足无措的窘境。

从应用光学转到凝聚态物理是个艰难的过程，作为曾经的一张实验物理领域的白纸，我要感谢 Olivier Heckmann, Cephise Cacho 以及在 Elettra 和 MAX-Lab 的工作人员对各种先进实验设备的讲解，让我对激光系统，超高真空系统，自旋分辨角分辨光谱仪等设备有了基本的认识。

特别地，我要感谢 Jean-Michel Mariot, Christine Richter 和 Paola De Padova. 感谢他们在发表文章上巨大的帮助。尤其是 Jean-Michel 不断反复仔细的核对和纠正。还要感谢 Juraj Krempasky 在实验以及数据处理过程中提供的非常有用的想法和建议。感谢 Peter Blaha 提供理论模型计算的数据，为我大部分工作的提供了良好的基础。

当然我还要感谢答辩委员会的全体成员，在对我的论文工作进行审核时表现出的专业而敬业的态度。

最后感谢王占山教授当初提供我来法国学习工作的机会，并且在我对前途感到迷惘的时候给予的支持。感谢 Eric Somson 租给我那间漂亮的小屋，让我在论文写作的整个过程中有个安静舒适的环境。

中国人有句古话：双亲在，不远行。在过去的四年中，我一直与我的父母相隔着小半个地球，但我希望在我完成人生第一件大事的时候告诉你们：我爱你们，每时每刻。

<b>Acknowledgement</b>	<b>I</b>
<b>Contents</b>	<b>III</b>
<b>Introduction</b>	<b>1</b>
<b>1. Theoretical aspects</b>	
<b>1.1 Basic theory</b> .....	3
<b>1.2 Half-metallic ferromagnets</b> .....	4
<i>1.2.1 Introduction</i>	
<i>1.2.2 Examples of half-metallic ferromagnets</i>	
<b>1.3 Theoretical approaches</b> .....	8
<i>1.3.1 Landau Fermi liquid</i>	
<i>1.3.2 Non quasi-particle states (NQP)</i>	
<b>2. Overview of Fe<sub>3</sub>O<sub>4</sub></b>	
<b>2.1 Atomic structure</b> .....	15
<i>2.1.1 Bulk crystal</i>	
<i>2.1.2 Surface structure</i>	
<b>2.2 Magnetic properties</b> .....	17
<b>2.3 Electronic structure</b> .....	20
<i>2.3.1 Band structure calculation</i>	
<i>2.3.2 Experimental determination of the electronic structure by photoemission</i>	
<i>2.3.3 Half-metallic properties: spin resolved photoemission</i>	
<i>2.3.4 Verwey transition</i>	
<b>3. Experimental aspects</b>	
<b>3.1 Synchrotron Radiation Source</b> .....	33
<b>3.2 Laser Source</b> .....	34
<b>3.3 Experimental techniques</b> .....	36
<i>3.3.1 Low Energy Electron Diffraction (LEED)</i>	
<i>3.3.2 X-ray based absorption spectroscopy techniques</i>	
<i>3.3.3 Photoemission Spectroscopy (PES)</i>	
<b>4. Simulation methods</b>	
<b>4.1 Electronic structure calculation</b> .....	48
<b>4.2 Effect of U-parameter</b> .....	50
<b>4.3 Parameters used in simulation</b> .....	51

<b>5. Results and Discussion</b>	
<b>5.1 Sample preparation and characterization</b> .....	57
5.1.1 <i>Sample preparation</i>	
5.1.2 <i>Characterization of samples</i>	
<b>5.2 Angle-resolved photoemission</b> .....	61
5.2.1 <i>Introduction</i>	
5.2.2 <i>Determination of <math>V_0</math></i>	
5.2.3 <i>ARPES analysis in critical points of the bulk Brillouin zone</i>	
5.2.4 <i>ARPES analysis at photon energy of 21eV</i>	
5.2.5 <i>Fermi surface map by ARPES</i>	
<b>5.3 Spin-resolved photoemission</b> .....	74
5.3.1 <i>“Static” spin polarization measurement</i>	
5.3.2 <i>Measurements of the spin dynamics</i>	
<b>Conclusion</b> .....	84
<b>References</b> .....	86
<b>Appendix A</b> .....	94
<b>Appendix B</b> .....	96
<b>Appendix C</b> .....	98

# Introduction:

In the solid-state physics, there are still some roadblocks until nowadays [1], which give us difficulties in the research work but also continual surprises. Two recent ones are introducing the existence of “half-metal” and the development of “spintronic devices”, which is the background for this thesis. I would like to introduce my thesis by answering three questions:

*What is Spintronics and why is it interesting?*

Thin films of magnetic materials, from hundreds of atomic layers to the ultimately single atomic layer have been studied for many years and have shown a lot interesting properties. The research field of investigation and use of such materials in electronic devices is called spintronics or magneto-electronics.

Spintronics involves the study of active control and manipulation of the spin degrees of freedom in solid-state systems. The control of spin is then a control of either the population and the phase of the spin of a set of particles, or a coherent spin manipulation of a single or a few-spin system. The purpose of spintronics is to understand the interaction between the particle spin and its solid-state environment to make useful devices. Fundamental studies of spintronics include investigations of spin transport in electronic materials, as well as understanding spin dynamics and spin relaxation.

An outstanding success of the spintronic device is in a large part based on the giant magneto-resistance (GMR)[2][3]. Current efforts in designing and manufacturing spintronic devices is to optimize the existing GMR-based technology by either developing new materials with larger spin polarization of electrons or making improvements or variations in the existing devices that allow for better spin filtering and try to find new ways to generate and utilize the spin-polarized currents.

Furthermore, except the magneto-resistance effects, the spintronics may also be applied to make spin transistor, spin laser and even spin-based quantum computers.

*What is a Half-Metallic Ferromagnet and why is it important for spintronics?*

1983, de Groot *et al* first postulated the existence of this new kind of material, a half-metal [4]. By definition, such materials have the Fermi level within the energy gap of the partial density of states for one spin orientation but possess metallic character for the other spin orientation, which means theoretically we can have 100% polarization near Fermi level (see Fig.1.1).

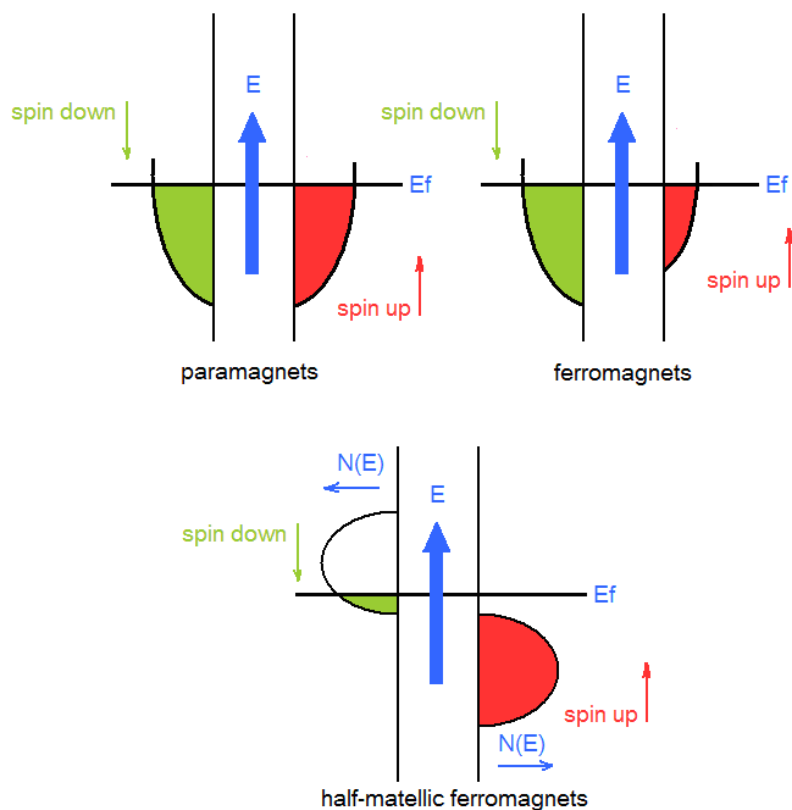


Fig.1.1 Schematic view of density of states of magnetic materials.

Half-metallic ferromagnet (HMF) is a subject of growing interest. HMFs have order-of-magnitude different spin contributions to electronic transport properties that can result in a perfect injection of polarized carriers. Half-metallic materials are therefore promising to make spintronic devices.

#### *Why we choose $Fe_3O_4$ as our object to study?*

Very few experiments have verified the theoretical predictions of 100% polarization for half-metallic ferromagnets up till now. There are a lot of reasons for this. One of them is the limitation of the theoretical model. The complex crystallographic structure of the candidates is not inherent to theory, and the strong electron correlation makes the standard one-electron model unsuitable. Another aspect is that the experimental conditions are not always satisfied, including the contamination, surface termination, and reconstruction. Notwithstanding these theoretical and experimental difficulties,  $Fe_3O_4$  has come to our research table. Because it has a very high Curie temperature (858 K) and its half metallicity is still under debate. Furthermore, taking into account its long history of application, its preparation technique and properties have been already relatively well understood. Recently thin film deposition has been mastered.

In this thesis, we used angle-, spin- and time-resolved photoemission spectroscopy to characterise the band structure, half-metallic properties and spin dynamic of  $Fe_3O_4$ .

# Chapter 1

---

---

## Theoretical aspects:

---

---

### 1.1 Basic theory

The basic theory explaining the behaviour of the electrons in the solid state is the non-relativistic Schrodinger's equation for electrons and nuclei that interact via the Coulomb force [5]. This basic Hamiltonian determines almost all the physical properties, but we cannot solve it in many real complicated cases. In particular, it cannot be solved accurately when the number of particles exceeds about 10. No computer existing can break this barrier, because it is a catastrophe of dimension.

Of course, we can reduce the complexity by using simple model and hope the simplified equation can still give the essential properties. The most famous one is “one-electron band theory”, which gives a considerably accurate description of the electronic structure of a lot of materials. In such a model, the electron-electron interaction and the interaction between nuclei are neglected. We consider only one electron propagating through a static periodic potential coming from the periodic crystal lattice. We can trace this model to 1930's by the work of Bloch and Wilson [6]. Then Landau gave out the description of quasi-particles and the adiabatic continuity of the quasi-particle liquid to the non-interacting Fermi gas [7][8]. The concept of quasi-particle describes equilibrium properties and excitations of the electronic, phononic and magnetic subsystems of condensed matter. To understand the Landau Fermi liquid, we can imagine turning on the interaction between electrons slowly, and observing how the eigenstates of the system evolved. There would be a one-to-one mapping of the low energy eigenstates of the interacting electrons with the those of the non-interacting Fermi gas. One can vividly imagine that the “one-electron band theories” (non-interacting Fermi gas) supposes the eigenstates in the infinite square well while the “Landau Fermi liquid theory” (interacting quasi-particle liquid) supposes the eigenstates in the parabolic potential well. Therefore, we retain the picture of Fermi particles carrying the same quantum numbers as their electron counter-parts in the free Fermi gas. These labels are not to be associated with electrons but to “quasi-particles” to remind us that the wavefunctions and energies are different from the corresponding electron in the non-interacting problem. [10]

Where there is a successful model, there is exception. For example, the Mott insulator, transition metal oxides with partially filled d-bands, cannot be explained by “one-electron band theories” or “Landau Fermi liquid theory”. [9] In this case, the electrostatic interaction between the conduction electrons takes more contribution and leads to insulating behaviour.

The insolubility and complexity tell us that the reality is full of phenomena and elegant laws. In consequence, a lot of new states have been found that encourage us to discover the higher organizing principles. One of those systems is the half-metal, which is the central interest in this thesis.

## 1.2 Half-metallic ferromagnets

### 1.2.1 Introduction

Since its introduction by de Groot and colleagues in the early 1980s [4], the concept of half metallic ferromagnetism has attracted great interest. Idealized, half-metals have only one spin channel for conduction: the spin-polarized band structure exhibits metallic behaviour for one spin channel, while the other spin band structure exhibits a gap at the Fermi level. Due to the gap for one spin direction, the density of states at the Fermi level has, theoretically, 100 % spin polarization. This gap in the density of states in one spin at the Fermi level, for example spin down, so  $N_{\downarrow}(E_F) = 0$ , also causes the resistance of that channel to go to infinity. The expected 100% spin polarization of the charge carriers in a half-metallic ferromagnet (HMF) is a hypothetical situation that can only be reached in the limit of vanishing temperature and neglecting spin-orbital interactions.

But debate concerning half-metals remains, because there is no clear experimental proof of half-metallicity. The most direct measurement is spin-resolved positron annihilation [11]. We should not confuse half-metallicity and the ability to produce a 100% polarized electron beam. The latter means ejecting electrons in the material crossing a surface or at interface into medium where the spin polarization is measured. In other words, the measured spin polarization is not an intrinsic materials' property. Crystal imperfection interfaces and surfaces make static perturbation of the ideal periodic potential which affect the states in the half-metallic gap and finally decrease the polarization dramatically in many promising half-metallic systems. The only proven half-metallic ferromagnet so far within the precision of the experiment is NiMnSb [12].

Spin dynamics can be understood in terms of the two magnetic excitations that occur in an itinerant magnet. Stoner excitations are spin-flip excitations across the Fermi surface that creates a hole of a given spin and an electron with opposite spin. These excitations occur primarily in a continuum of states called the Stoner continuum. Consequently, the class of half-metallic ferromagnets is characterized by the presence of well-defined local moments and also by the absence of the Stoner continuum of electron-hole excitation by a weak damping of the collective spin-waves throughout the Brillouin zone. The interaction of charge carriers at the Fermi level with well-defined magnons\* (spin-waves) will make the spectrum very different that of the weak itinerant magnetic materials. In fact, if the spin-up sub-band is completely filled, the spin-up electrons cannot freely move but form spin polaron (electron-magnon interaction) states and scatter the carriers of magnons. This is the reason for the non-Fermi-liquid nature limited only to half-metallic ferromagnets, because in the conventional itinerant magnets, they are masked by the paramagnon (quasi-particles which describe the paramagnetic fluctuation in the Landau Fermi-liquid theory) contributions [13].

### 1.2.2 Examples of half-metallic ferromagnets

#### (a) Heusler alloys and zinc-blende structure compounds

A Heusler alloy is a ferromagnetic metal alloy based on a Heusler phase. Heusler phases are intermetallics, i.e. compounds containing two or more metallic elements, with optionally

\*magnon: a collective excitation of electrons' spin structure in a crystal lattice. It can be viewed as a quantized spin wave [14].

one or more non-metallic elements, with particular composition and face-centred cubic crystal structure. The constituting elements are not necessarily ferromagnetic, the double-exchange mechanism between neighboring magnetic ions can make the structure ferromagnetic. There are two structures of Heusler alloys, named  $L2_1$  and  $C1_b$ , which represent a full Heusler alloy ( $X_2YZ$ ) and a semi-Heusler alloy ( $XYZ$ ) respectively. [15]

The Heusler  $C1_b$  structure consists of the zinc-blende structure with an additional occupation of the  $(1/2, 1/2, 1/2)$  site. Atoms at the latter position, as well as those in the origin, are tetrahedrally coordinated by the third constituent, which itself has a cube coordination consisting of two tetrahedra. The Heusler  $L2_1$  structure is obtained by an additional occupation of the  $(3/4, 3/4, 3/4)$  by the same element already present on the  $(1/4, 1/4, 1/4)$  site (Fig. 1.1). This results in occurrence of an inversion centre that is not present in the zinc-blend and Heusler  $C1_b$  structures. This difference has important consequences for the half-metallic band gaps. Electronic structure of the Heusler alloys has been reviewed recently [4].

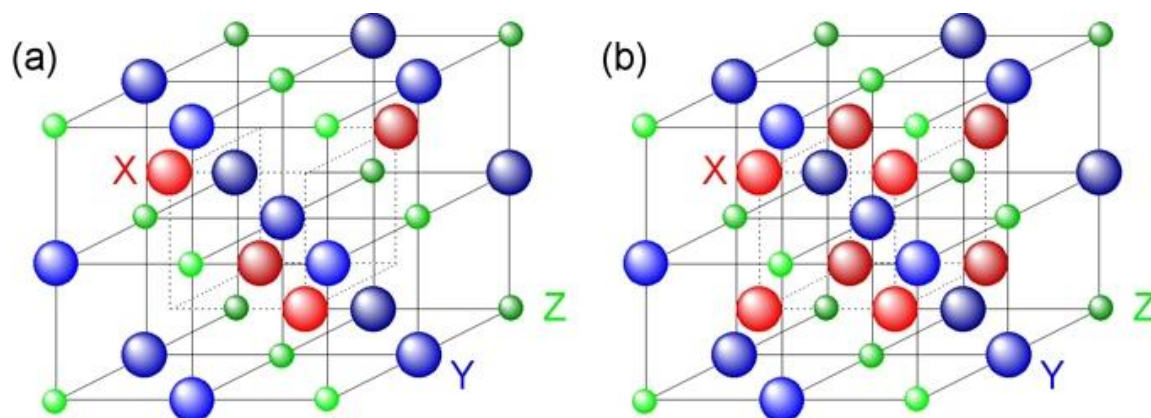


Fig.1.1 Crystal structure of Heusler  $C1_b$  (a) and  $L2_1$  (b) alloys

### (b) Sulfides

According to calculation of Zhao, Callaway and Hayashibaran [16] pyrites may have half-metallic properties. Their results for  $CoS_2$  show that near the Fermi level, there is a partial filled  $e_g$  majority band as well as a minority  $e_g$  band are overlapping at the Fermi level. But only a small number of minority spin states are occupied. Hence, they describe  $CoS_2$  an almost HMF. It is also supposed that half-metallic magnetism can be obtained in the ternary system  $Fe_xCo_{1-x}S_2$  [17]. A detailed study, both computational and experimental [18], reveals a strong dependence of the spin polarization at the Fermi level on the composition. Theoretically, 100% spin polarization is obtained for  $x = 0.25$ , whereas the maximal polarization (85%) determined with Andreev reflection at 4.2K is obtained at  $x = 0.15$ . The polarization drops with higher concentrations of iron. The Fermi level is located very close to the bottom of the conduction band. This can lead to thermal instabilities of the half-metallicity. Recently half-metallic properties of compounds with pyrite-structure have been reviewed by Leighton et al [19].

**(c) Strongly magnetic half-metals with majority spin gap**

In contrast to the more conventional case of partially filled  $d$  (or  $f$ ) electronic shells, the magnetic properties of strongly magnetic half-metals with majority spin gap arise from partially filled  $p$  orbitals. Until recently, the heavy alkali oxides ( $\text{RbO}_2$ ) are calculated to be this type of HMF. [20] See Fig.1.2, the magnetic moment is carried by complex oxygen ions. Besides the oxygen molecule, that has two unpaired electrons, the oxygen molecular ions ( $\text{O}_2^-$ ) give partially filled  $p$  electron levels. Unfortunately there is no direct experimental evidence yet. In most cases the corresponding phenomena are induced by the defects in experimental data. To further explore  $p$  electron magnetism as promising choice for applications, it is therefore desirable to study intrinsic  $p$  electron magnetism in defect-free bulk materials.

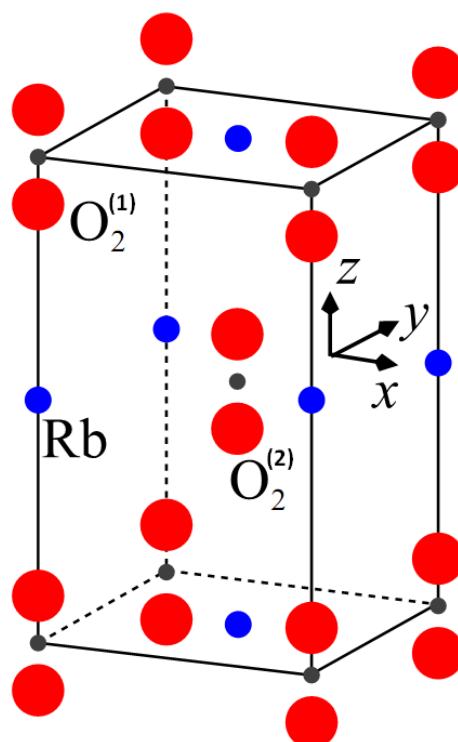


Fig.1.2 Averaged tetragonal structure of  $\text{RbO}_2$ . Oxygen and rubidium atoms are represented by large (red) and small (blue) spheres, respectively. The two  $\text{O}_2$  molecules within the tetragonal unit cell will be denoted as  $\text{O}_2^{(1)}$  and  $\text{O}_2^{(2)}$  [21]

**(d) Strongly magnetic half-metals with minority spin gap**

One of the most important half-metal with minority spin gap is  $\text{CrO}_2$ . The origin of the half-metallicity of  $\text{CrO}_2$  comes from the  $\text{Cr}^{4+}$  ions where the two remaining  $d$  electrons occupy the majority  $d$  states. The valence band for the majority-spin is filled to  $2/3$  and therefore it is bringing the metallic properties. The minority-spin  $d$  states are at significantly higher energy due to the exchange splitting. For this reason the Fermi level falls in a band gap between the (filled) oxygen  $2p$  states and the (empty) chromium  $d$  states. Thus the half-metallic properties of chromium dioxide are due to properties of chromium and its valence band. As long as the crystal-field splitting is not changed too drastically, these half-metallic properties are conserved. The influence of impurities appears not be dramatic and a number of crystallographic surfaces retain the half-metallicity of the bulk. As a matter

of fact, all the surfaces of low index are half-metallic with a possible exception of one of the (101) surfaces [20][22].

Although first measurements did not confirm these expectations [23], they were confirmed later by experiments like tunnelling [24] or Andreev reflection [25]. Recently, a technique called chemical vapour deposition was used to grow single-crystal films of chromium dioxide. 96 % spin polarization of the chromium dioxide films has been found [26].

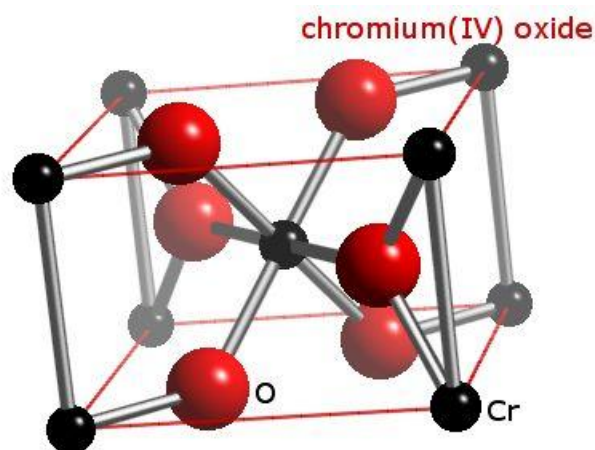


Fig.1.3 Crystal structure of chromium dioxide

#### (e) Weakly magnetic half-metals with majority spin gap

HMFs belonging to this group crystallize in the perovskite structure. A perovskite structure is any material with the same type of crystal structure as calcium titanium oxide ( $\text{CaTiO}_3$ ), known as the *perovskite structure*, or  $^{XII}A^{2+VI}B^{4+}X^{2-}_3$  with the oxygen in the face centers. The general chemical formula for perovskite compounds is  $\text{ABX}_3$ , where 'A' and 'B' are two cations of very different sizes, and X is an anion that bonds to both. The 'A' atoms are larger than the 'B' atoms. The ideal cubic-symmetry structure has the B cation in 6-fold coordination, surrounded by an octahedron of anions, and the A cation in 12-fold cuboctahedral coordination. The relative ion size requirements for stability of the cubic structure are quite stringent, so slight buckling and distortion can produce several lower-symmetry distorted versions, in which the coordination numbers of A cations, B cations or both are reduced.

Magnetite is also a candidate for this group of HMFs. It is one of the most wide-spread natural iron compounds and the most ancient magnetic material known to humanity. However, till now, we still have no complete explanation of its magnetic, electronic and even structural properties, many issues about this substance remaining controversial. As demonstrated by the band-structure calculation [27], at room temperature magnetite having inverse cubic spinel structure is a rare example of HMF with majority spin gap. Since it is the subject of this thesis, more details will be introduced in next chapter.

### 1.3 Theoretical approaches

In all metallic ferromagnets, interaction between conduction electrons and spin fluctuation is of crucial importance for physical properties. Particularly, the scattering of charge carriers by magnetic excitations determines transport properties of itinerant magnets. For half-metallic ferromagnets (HMF) the electron-magnon interaction can considerably modify the energy spectrum in HMF. Because of the special band structure of HMF, the states near Fermi surface are incoherent, called non-quasi-particle states, which occur in the energy gap of one spin orientation [28]. It is one of the most interesting properties for HMF. In order to better describe the physical mechanism, I remind here some aspects of Landau Fermi liquid theory.

#### 1.3.1 Landau Fermi liquid

Lev Davidovich Landau introduced the Fermi liquid theory in 1956, with two key ideas behind it: the exclusion principle and the notion of adiabatic continuity. [29]

The Fermi liquid theory is based on the assumption that starting from the non-interacting system of particles one can analyze the interacting case by applying perturbation theory. If the excitations of the non-interacting system are connected to the excitations of the interacting system by a one-to-one correspondence (at least on short time scales) the two cases are said to be connected by “adiabatic continuity”. If you imagine that we start from the non-interacting system excited in some state and then turn on the interaction adiabatically, i.e. so slowly that the occupation numbers are not changed, then we would end up in a corresponding excited state of the interacting system. What we really are claiming is that the excited states of the interacting system can be labelled by the same quantum numbers as those we used to label the non-interacting system. [29]

Make a simplest example, a particle in a box with an infinitive potential wall. The eigenstates of this particle are illustrated in the Fig.1.4 (a). According to elementary quantum mechanics calculation, the eigenstates are standing sine waves with nodes on the walls, labeled by the number of additional nodes in the wave function as the energy increases. [8]

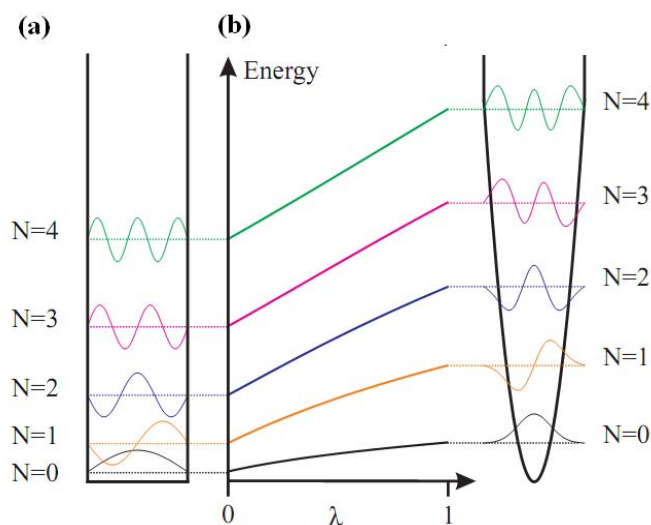


Fig.1.4 Adiabatic continuity concept for the quantum labels of eigenstates of a particle in a potential box. (a) in an infinite potential wall; (b) apply a quadratic potential to the particle in the box.

Now we introduce an additional weak quadratic potential:

$$-\frac{1}{2} \frac{d^2 \varphi}{dx^2} \Psi = E \varphi, \quad V(x) = \begin{cases} \frac{1}{2} \lambda x^2 & |x| < \pi \\ \infty & |x| \geq \pi \end{cases} \quad (1.1)$$

The new eigenstates are no more simple sine waves but are with a mixing of all the eigenstates of the original non-interacting system. It's clear in the Fig.1.4 (b) that the way of labeling the eigenstates by the number of nodes is still good for the more complicated situation. This is the essence of adiabatic continuity.

Now we discuss the interaction gas of electrons. Suppose that the interaction between electrons affects the system slowly and so the eigenstates evolves slowly. There would be a one-to-one mapping of the low energy eigenstates of the interacting electrons with those of the non-interacting Fermi gas. The good quantum numbers associated with the excitations of the non-interacting system would still remain. In order to indicate the difference of the wave function and energies between the corresponding electrons and the non-interacting electrons, "quasi-particle" is used to name the former. It accounts for the measured temperature dependences of the specific heat and Pauli susceptibility, because these properties require only the presence of a well-defined Fermi surface, and are not sensitive to whether electrons or quasi-particles form it. That means the quasi-particle distribution function is unchanged from the free particle result. Because the interacting state has same label as the non-interacting state, the configurational entropy doesn't change. Each quasi-particle contributes additively to the total entropy of the system. This is not true for the energy in interacting system. It should be taken into account that the energy of individual excitation will not generally add to yield the total system energy for the interacting system. Landau used two terms to modify this energy. First, when a quasi-particle moves, there will be a back-flow in the filled Fermi sea as the quasi-particle 'pushes' the ground state out of the way. This modifies the inertial mass of the quasi-particle  $m$  to  $m^*$ . Second, one quasi-particle's energy depends also on the distribution of other quasi-particles. Landau called it 'f function'. Now the total energy of the interacting system for an isotropic system can be written as a functional of the quasi-particle distribution ( $\delta n_{\vec{k},\sigma}$ ). [8]

$$E = \sum_{\vec{k},\sigma} \frac{p_F}{m^*} (\hbar k - p_F) \delta n_{\vec{k},\sigma} + \frac{1}{2} \sum_{\vec{k}',\sigma'} f_{\vec{k}\sigma\vec{k}'\sigma'} \delta n_{\vec{k},\sigma} \delta n_{\vec{k}',\sigma'} \quad (1.2)$$

Where  $p_F$  is the Fermi momentum,  $\vec{k}$  is the wavevector and  $\sigma$  is spin.

In the equation above, it is neglected that measuring the energy with the Hamiltonian could change the quasi-particle distribution, which forms matrix elements in the Hamiltonian. Since the quasi-particles and holes are only approximately eigenstates of the system, we can estimate a lifetime for them. As Fermi Golden rule:

$$\frac{1}{\tau_\varepsilon} = \frac{2\pi}{\hbar} \sum_f |V_{if}|^2 \delta(\varepsilon - \varepsilon_f) \quad (1.3)$$

The sum is all over the possible final states  $f$ . For the time being, the matrix elements  $|V_{if}|$  is assumed to be a constant. We should only consider the energy conservation and Pauli

Chapter 1: Theoretical aspects

principle for quasi-particles. At the temperature absolutely zero, the only electron-hole excitation allowed by Pauli principle lowers the energy of the original quasi-particle by an amount  $\omega$  by making a electron-hole pair in the Fermi sea (See Fig.1.5). It should be smaller than the scattered quasi-particle's energy  $\epsilon$  therefore only occupied states within  $\omega$  of Fermi surface could absorb this energy to go above the Fermi surface. Thus the sum of final states in the equation 1.3 is approximately written as  $\frac{1}{\tau_\epsilon} \approx \frac{\pi}{\hbar} |V|^2 g_F^2 \epsilon^2$ . ( $g_F$  is the density of states at the Fermi surface.)

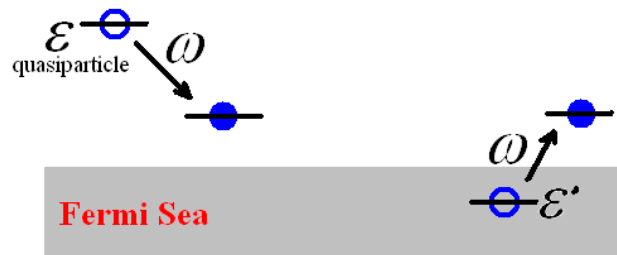


Fig.1.5 The scattering process for a quasi-particle with energy  $\epsilon$  above the Fermi surface involves the creation of a particle-hole excitation

The quasi-particle near the Fermi surface is clearly defined since the decay rate ( $\epsilon^2$ ) is much smaller than the excitation energy ( $\epsilon$ ), while the quasi-particle far from the Fermi surface is no more adiabatic continuity, the interaction is comparable too strong. At a low temperature, there is a minimum energy for the quasi-particles near the Fermi surface and the scattering rate is proportional to  $T^2$  (Temperature). All these above make Landau's theory valid for the interacting electron gas.

In the concept of adiabatic continuity, there remains a fraction ( $z$ ) of the original non-interacting excited state wave function in the quasi-particle wave function. This fraction acts like a weight of quasi-particles, in other words, plays the role of the order of the zero temperature Fermi liquid state. [18]

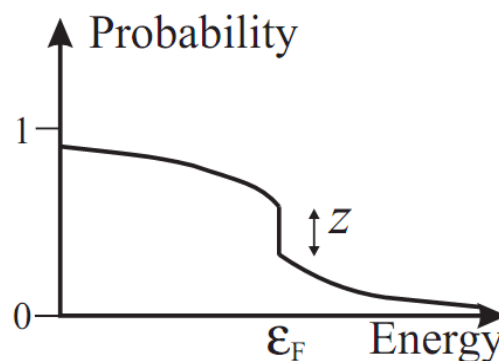


Fig.1.6 The probability that a state of a given energy is occupied at absolute zero temperature for interacting electron gas.  $z$  is the order of the Fermi liquid

How the order parameter affects the system can be clearly seen in the spectral function  $A(\omega, \mathbf{k})$ , which shows the probability that an electron with momentum  $\mathbf{k}$  can be found with

Chapter 1: Theoretical aspects

energy  $\omega$ . For non-interacting systems, the spectral function is a delta function  $\delta(\omega - \epsilon_k)$ , while for interacting systems, the spectrum is broadened in energy because every single electron may take part in many eigenstates.  $z$  is the probability that the electron may be found in the quasi-particle eigenstates, see Fig1.6. At zero temperature, the electron spectral function in a Fermi liquid is a sharp peak with width proportional to  $(k - k_F)^2$ , giving the lifetime and weight under the peak of  $z$  (Fig. 1.7).

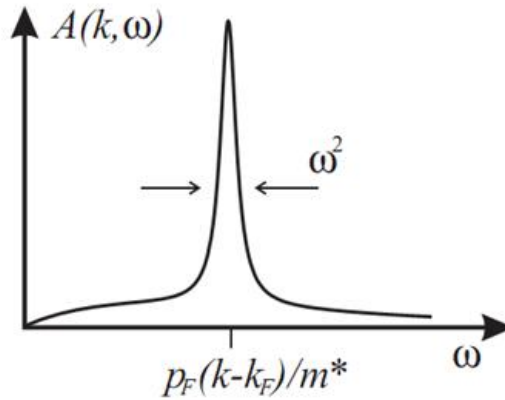


Fig.1.7 In the Fermi liquid theory, the probability that an electron with moment  $k$  may be found with a given energy is now spread out but retains a peak at the new quasi-particle energy. This peak sharpens as  $k \rightarrow k_F$

1.3.2 Non quasi-particle states (NQP)

The NQP states in the s-d exchange model of magnetic semiconductors have been considered [28]. It was shown that they can occur either only below the Fermi energy or only above it. Later on, it was realized that HMFs are natural substance for theoretical and experimental investigation of NQP effects. [30]

We consider the case where the spin-up electronic structure is metallic and the spin-down is semiconducting. The origin of these non-quasi-particle states comes from spin-polaron process: the spin down low energy electron excitations, which are forbidden for HMF in the one-particle picture, turn out to be possible as superposition of spin up electron excitations and virtual magnons. A polaron is a quasiparticle composed of a charge and its accompanying polarization field. A slow moving electron in a dielectric crystal, interacting with lattice ions through long-range forces will permanently be surrounded by a region of lattice polarization and deformation caused by the moving electron. Moving through the crystal, the electron carries the lattice distortion with it, thus one speaks of a cloud of phonons accompanying the electron.

According to the conservation laws, in the many-body theory the spin-down state with the quasi-momentum  $k$  can form a superposition with the spin-up states with the quasi-momentum  $k - q$  plus a magnon with the quasi-momentum  $q$  running through the whole Brillouin zone. Taking into account the restrictions from the Pauli principle (an impossibility to scatter into occupied states) one can prove that this superposition can form only above the Fermi energy. Oppositely, the non-quasi-particle states form only below the Fermi energy. If we neglect the magnon energy in comparison with the typical electron energy, the density of non-quasi-particle states will vanish abruptly right at the Fermi energy; more accurate

## Chapter 1: Theoretical aspects

treatment shows that it vanishes continuously in the interval of the order of the magnon energy according to a law which is dependent on the magnon dispersion. As a consequence, the non-quasi-particle states are almost currentless. [13][31]

It is worthwhile to mention that the existence of non-quasi-particle states is very crucial for spin-resolved photoemission spectroscopy in HMF. See Fig.1.8, for the cases that an energy gap exists for minority spin states, the non-quasi-particle states should arise above the Fermi energy. On the other hand, the cases with majority spin gap, one should expect the non-quasi-particle states below the Fermi energy. [32]

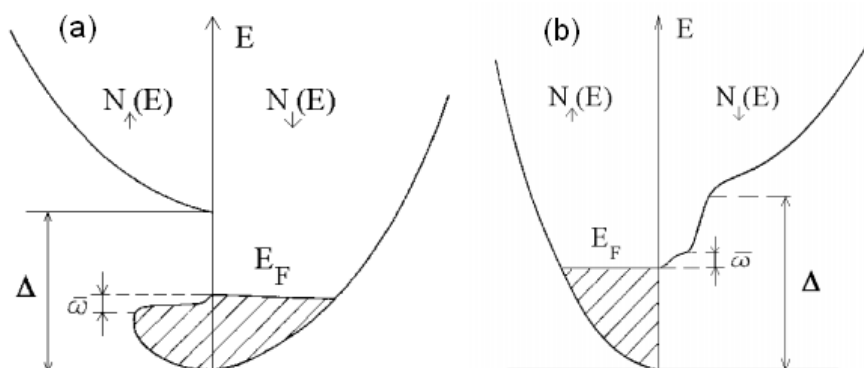


Fig.1.8 Density of states in HMF (schematically). (a) with majority spin gap, non-quasi-particle states with spin up occur below the Fermi level; (b) with minority spin gap, non-quasi-particle states with spin down occur above Fermi level.  $\bar{\omega}$  is the frequency of magnon.  $\Delta$  is exchange energy.

### 1.3.3 Decrease of spin polarization in HMF

100% spin polarization at Fermi level is the fingerprint of HMF. But, in experiments, it is almost impossible to measure such high values of polarization, because there are several depolarization mechanisms during the process of experiments.

Some of these depolarization mechanisms are suggested based on magnon and phonon excitations.[33] It was claimed that random inter-atomic exchange fields generated spin-disorder and rotated locally the spin direction which modified the local magnetic moment and spin polarization. The experimental results of spin-resolved photoemission spectra always give strong deviation from 100% polarization near the Fermi energy. This is at least partially related to NQP states. (NQP states are located in the band gap of one spin orientation near Fermi level, that reduces the spin polarization of density of states.) See Fig.1.8., for HMF with majority spin gap, the NQP should exist below the Fermi energy and thus be relevant for photoelectron spectroscopy (e.g.  $\text{Fe}_3\text{O}_4$ ). Since electron correlations in  $\text{Fe}_3\text{O}_4$  are quite strong, the spectral weight of NQP states should be considerable.

Let's now take a Hubbard ferromagnet with an infinitely strong correlation as an extreme case. The DOS calculation will give fully depolarized states below Fermi level of doubles (doubly occupied sites). It means that the current carrier electrons with spin up and down may be found with same probability. [34]

Furthermore, the temperature also plays a role in the decrease of spin polarization. For finite temperature, the NQP states at Fermi energy are proportional to the filling of the energy gap. It is very important for the application of HMF in spintronics. Generally, when the

temperature increases to be comparable with  $T_C$ , there is no essential difference between half-metallic and ordinary ferromagnets because of the totally filled gap. However this issue of finite-temperature spin polarization in HMF remains an open question.

## 1.4 Calculation of HMF

In this section, I briefly review the development of calculation models and several approximation approaches in use.

Hubbard model is the simplest model to investigate many-electron system with effects of electron correlation in metallic magnets. This model is widely used for itinerant electron ferromagnetism in which the Coulomb interaction is taken into account [35]. However stabilizing the ferromagnetic solution within the Hubbard model is very difficult and standard approaches in the itinerant electron magnetism theory don't work well for strong correlation systems, e.g. band calculation and spin-fluctuation, since correlations lead to a radical reconstruction of the electron spectrum (Hubbard's subbands). Although, Hubbard model is rich in physics, the correlation effects should be taken into account to calculate the band structure of HMF. The interaction of electrons with static nuclei and external potentials (defects, electronic field, magnetic field) and Coulomb interaction between electrons are considered. The solution of a general many-electron problem is based on its functional formulation in a framework of effective action approach. [36]

The most accurate scheme is the Baym-Kadanoff (Luttinger-Ward) [37][38] functional of the one-electron Green's function that allows us in principle to calculate not only free energy and thus thermodynamic properties of the system, but also the Green's function and the corresponding excitation spectrum. The reason why this scheme works very well for model many-body analysis and preserves its broad practical use in the electronic structure calculation is that it is related with difficulties to find an exact representation of free energy, even for simple systems.

In this situation, the density functional scheme of Kohn and Sham turns out to be the most successful one for the electronic structure calculation of an electronic system with not too strong correlation. The Kohn-Sham equation is the Schrödinger equation of a fictitious system of non-interacting particles that generate the same density as any given system of interacting particles [39]. This scheme describes the exact ground state energy as a functional of the electron density which is variably exploited once this functional is known. However, an exact form of the exchange-correlation functional is generally unknown.

Through the Kohn-Sham equations, Density functional theory (DFT) reduces the quantum mechanical ground-state many-electron problem to a self-consistent one-electron form.

$$\left( -\frac{\hbar^2}{2m} \nabla^2 + v_{eff}(r) \right) \phi_i(r) = \varepsilon_i \phi_i(r) \quad (1.4)$$

Here,  $\varepsilon_i$  is the orbital energy of the corresponding Kohn-Sham orbital,  $\phi_i$  is the density for the system. The corresponding constraint fields in the effective action are related to the Kohn-Sham interaction potential  $v_{eff}$ . It is well known that the Kohn-Sham equations can be regarded as a procedure to solve the exact Dyson equation for Green functions with a suitable

*Chapter 1: Theoretical aspects*

self-energy. Hence, the formulation of many-body theory with Green functions embeds DFT in its most frequently applied position. DFT calculations are usually based on the Local Spin Density Approximation (LSDA) or the Generalized Gradient Approximation (GGA). These approximations have been proved very successful to interpret or even predict material properties in many cases, but they fail notably in the case of strongly-correlated electron systems. For such systems the so-called LSDA+U (or GGA+U) method is used to describe static correlations, whereas dynamical correlations can be approached within the LSDA+DMFT (Dynamical Mean-Field Theory). An important dynamical many-electron feature of HMF is the appearance of non-quasiparticle states which can contribute essentially to the tunnelling transport in hetero-structures containing HMF. As introduced above, the origin of these states is connected with “spin-polaron” processes. The density of these non-quasiparticle states vanishes at the Fermi level but increases drastically at the energy scale of the order of a characteristic magnon frequency ( $\bar{\omega}$ ), giving an important contribution in the temperature dependence of the conductivity due to the interference with impurity scattering. Strong spin-flip excitation processes are responsible for these “spin-polaron” processes by modifying electronic self-energy in itinerant electron magnets [36]. The only way to consider the effects of spin-flip processes of real materials is LSDA+DMFT, in which the complicated many-body problem for a crystal is split into a one-body problem for the crystal and many-body problem for auxiliary system, so that we can hope to calculate the correlation effects more or less accurately. [40]

In this thesis, GGA+U is applied as a theoretical reference, because along with LSDA+U method, they are proved to be good enough to explain the experimental results of  $\text{Fe}_3\text{O}_4$ . The calculation and simulation details are introduced in chapter 4.

## Chapter 2

---

# Overview of Fe<sub>3</sub>O<sub>4</sub>

---

### 2.1 Atomic structure

#### 2.1.1 Bulk crystal

Fe<sub>3</sub>O<sub>4</sub> was discovered before 1500 B.C., and it is the first known magnet and extensively used for industrial applications. At room temperature Fe<sub>3</sub>O<sub>4</sub> has a cubic inverse spinel structure ( $a=8.397 \text{ \AA}$ ). (Fig. 2.1 and Fig.2.2)

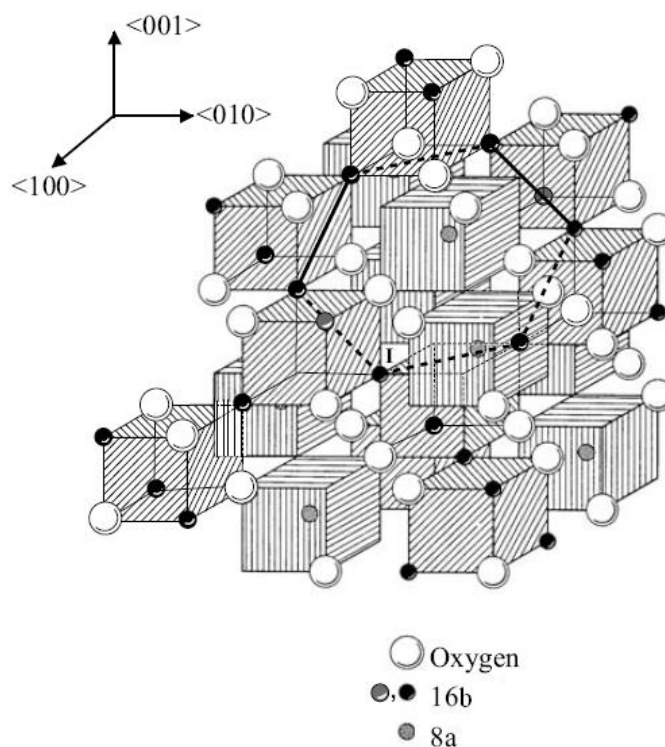


Fig.2.1 Inverse spinel lattice of Fe<sub>3</sub>O<sub>4</sub> (Anderson model)

The larger O<sup>2-</sup> anions form a close-packed face-centered-cubic structure, with the smaller Fe<sup>2+</sup>/Fe<sup>3+</sup> ions located at two distinct interstitial sites. In the O<sup>2-</sup> lattice, there are two sites, normally denoted as A and B. One third of the Fe ions occupy the tetrahedrally coordinated A sites, which consist only of Fe<sup>3+</sup> ions, while the remaining two thirds ions occupy the B sites, which are octahedrally coordinated and contain both Fe<sup>2+</sup> and Fe<sup>3+</sup>. It can be described by the formal chemical formula Fe<sub>A</sub><sup>3+</sup>[Fe<sup>2+</sup>Fe<sup>3+</sup>]<sub>B</sub>(O<sup>2-</sup>)<sub>4</sub>.

At 120 K, Fe<sub>3</sub>O<sub>4</sub> undergoes the so-called Verwey transition manifested by the occurrence of a spontaneous, inter-correlated change of both lattice symmetry and electric conductivity in

certain ionic crystals. In  $Fe_3O_4$ , such an abrupt change occurs at  $T_v \approx 120$  K. This is a typical first-order metal-insulator transition.

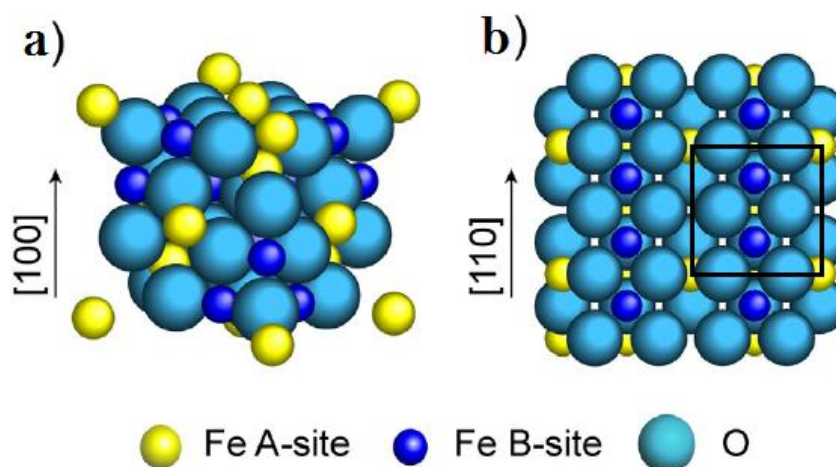


Fig.2.2 (a) side view of the inverse spinel  $Fe_3O_4$  structure.

(b) Top view of the  $Fe_3O_4(100)$  bulk B-termination. The black square in the (b) presents the  $p(1 \times 1)$  bulk unit cell

### 2.1.2 Surface structure

Many experimental techniques, like low energy electron diffraction (LEED), scanning tunneling microscopy (STM), X-ray photoelectron diffraction (XRD), low energy ion scattering (LEIS) etc., have been used to investigate natural or artificial single crystals and also thin films of  $Fe_3O_4$ .

According to the classification of the surfaces of ionic or partly ionic materials, the  $Fe_3O_4(001)$  surface is polar and therefore must reconstruct to minimize the surface energy. A lot of attention was focused on the study of the  $(\sqrt{2} \times \sqrt{2})R45^\circ$  reconstruction observed on the (100) surface. G. Tarrach et al observed the same LEED pattern on the surface of a single crystal. Later on Y. J. Kim found the same reconstruction on the molecular beam epitaxy thin film of magnetite. [22]. Tarrach suggested that the top-most surface layer of  $Fe_3O_4$  consists of a full monolayer of tetrahedral (A-site) Fe ions (i.e.  $Fe^{3+}$ ). They suggested that the surface charge is auto-compensated due to an ordered array of tetrahedral Fe vacancies.

The controversial understanding of the  $Fe_3O_4(001)$  surface led to many investigations. Using XPS, XRD, and STM, Chambers et al [23] suggested that the  $Fe_3O_4(001)$  surface is constituted by a half monolayer of tetrahedral  $Fe^{3+}$ . Mijiritskii et al [24] arrived at the same conclusion. They measured a thin epitaxial film (grown by  $O_2$  assisted MBE of Fe on a MgO (001) substrate) by LEED and LEIS. In contrast, Voogt et al [25] and Stanka et al [26] supported the B-terminated surface where auto-compensation is achieved by an array of oxygen vacancies accompanied by a variation in  $Fe^{3+}$  to  $Fe^{2+}$  ratio per unit cell or by the removal of one oxygen ion per unit cell and increase of the the charge of octahedral Fe ions from +2.5 to +2.7. Whatever the type of surface termination is, the  $(\sqrt{2} \times \sqrt{2})R45^\circ$  reconstruction was explained as an ordered array of Fe or O vacancies.

More recently, I.V. Shvets et al provided evidence of a highly ordered surface terminated

by octahedral planes (B layer: consists of  $Fe_B$  and O) [41]. They proposed that the reconstruction is due to charge ordering on the surface, rather than to a structural change of the surface (i.e. ordered array of Fe or O vacancies). The charge ordering result was supported by an electron diffraction experiment by Rudee et al. [42]

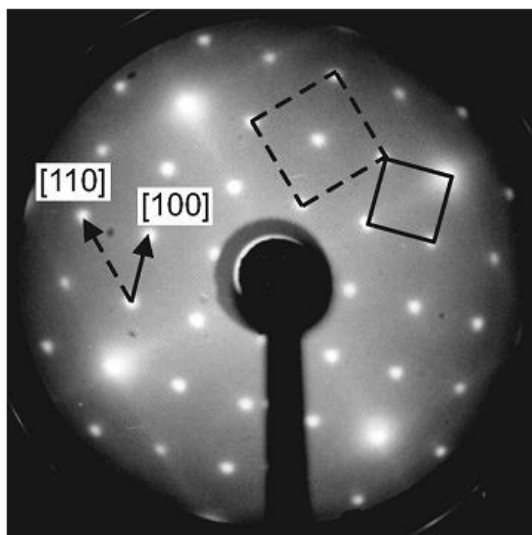


Fig.2.3 LEED pattern of a clean  $Fe_3O_4$  (001) surface observed with electron energy of 52eV. Dashed square represents the  $p(1 \times 1)$  unit cell and solid square represents the  $(\sqrt{2} \times \sqrt{2})R45^\circ$  reconstruction; the crystallographic axis are marked [41]

A quantitative analysis of surface is very difficult for LEED and other related techniques, because it involves a large number of atoms. An efficient procedure to resolve the surface structure is to combine diffraction analysis with DFT calculation. According to this method, R.Pentcheva et al [43] provide a new understanding of  $Fe_3O_4$  (001) surface. They support the idea that  $Fe_3O_4$  (001) surface is terminated by B layer. The stabilization of the surface involves a Jahn-Teller distortion with a wavelike displacement of iron and oxygen atoms, i.e.  $(\sqrt{2} \times \sqrt{2})R45^\circ$  reconstruction.

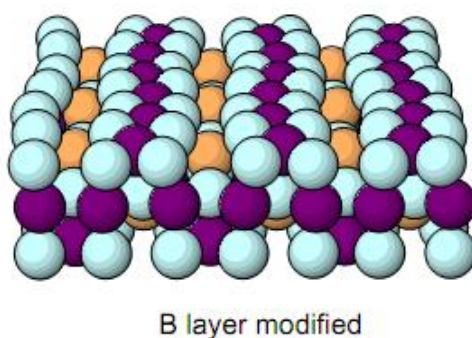


Fig.2.4 Structure of the modified B layer for  $Fe_3O_4$  (001) surface proposed in [43].

## 2.2 Magnetic properties

$Fe_3O_4$  is a ferrimagnet with a Curie temperature of 858 K. The magnetic moments inside each, A and B sub-lattices are ferromagnetically aligned and these two sub-lattices are antiferromagnetic with respect to each other, see Fig.2.5. The net magnetic moment is  $4.1 \mu_B$  per formula unit. This magnetic structure was used to explain the magnetization data by Néel

and confirmed later on by neutron scattering measurement.[44]

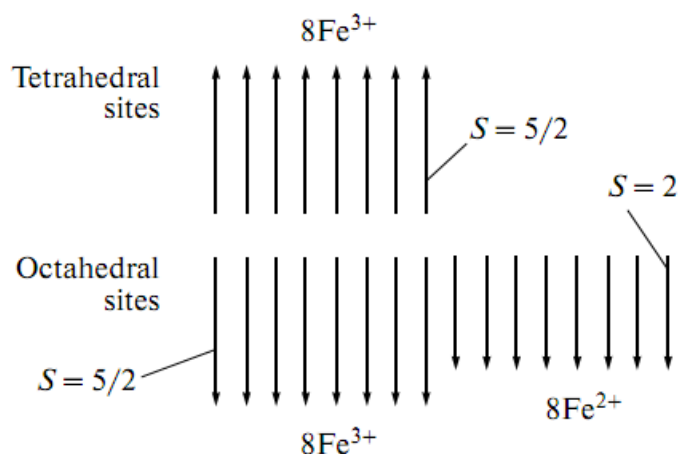


Fig.2.5 Schematic view of magnetic moments in  $Fe_3O_4$

Bulk magnetic properties of magnetite have been studied for many years; here I mention some recent studies done on thin layers. S.K. Arora *et al* [45] reported studies of the magnetic properties of  $Fe_3O_4$  films (2 nm to 55 nm) grown on MgO (001) (See Fig. 2.6 and 2.7).

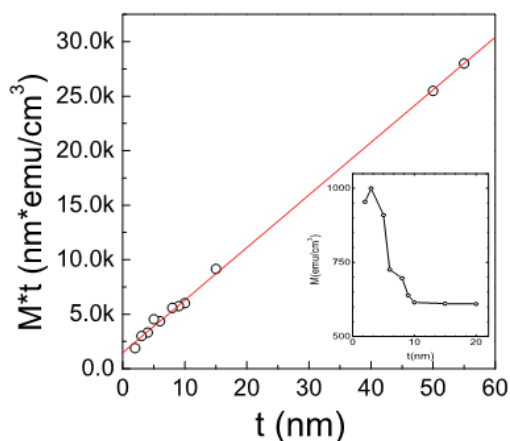


Fig.2.6 Magnetization of  $Fe_3O_4$  at 10 kOe multiplied by the film thickness as a function of film thickness. The solid line represents a straight line fit to the data. In the inset, Magnetization, measured at 10 kOe, as a function of film thickness for  $t < 20$  nm [45].

During the epitaxial growth of  $Fe_3O_4$  films on MgO substrate, when different “islands” getting bigger and bigger, even though the crystallographic direction remains the same, but each side of the “island” boundary could have an opposite phase. This so-called anti-phase boundary may lead to unusual magnetic properties of epitaxial  $Fe_3O_4$  films. They infer that the non-compensation of spin moments between A and B type planes is one of the major factors for the enhancement in magnetization in thin films, as deduced from the hysteresis loops shown in Fig 2.7.

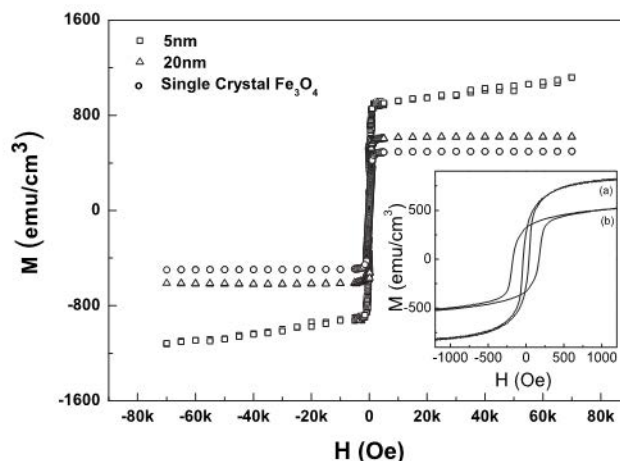


Fig.2.7 Hysteresis loops of 5 and 20 nm  $Fe_3O_4$  films and single crystal measured at 300 K with an in-plane magnetic field applied along the (001) direction. Magnetization values are normalized to the volume of  $Fe_3O_4$ . In the inset are the zoom at low magnetic field for (a)5 nm and (b)20 nm [45]

V.N. Petrov and A.B. Ustinov studied the magnetic properties of the  $Fe_3O_4$  (110) surface by spin resolved Auger electron spectroscopy (SRAES) [46]. A beam of unpolarized electrons with energy of 1500eV excited the Auger transitions. The problem related to magnetic moments of  $Fe^{2+}$  and  $Fe^{3+}$  ions on the  $Fe_3O_4$  (110) surface is discussed. They clearly observed two Auger peaks at 38 eV and 46 eV in a second derivative profile. (See Fig. 2.8) The polarization corresponding to the peak 46 eV is  $\sim 13\%$  and  $\sim 6\%$  for 38 eV. The authors concluded that the peak at 38 eV is associated with  $Fe^{3+}$  ions, the magnetic moments of which are opposite and then cancel each other. The magnetic moments of  $Fe^{2+}$  are not compensated and are responsible for the formation of the peak at 46 eV.

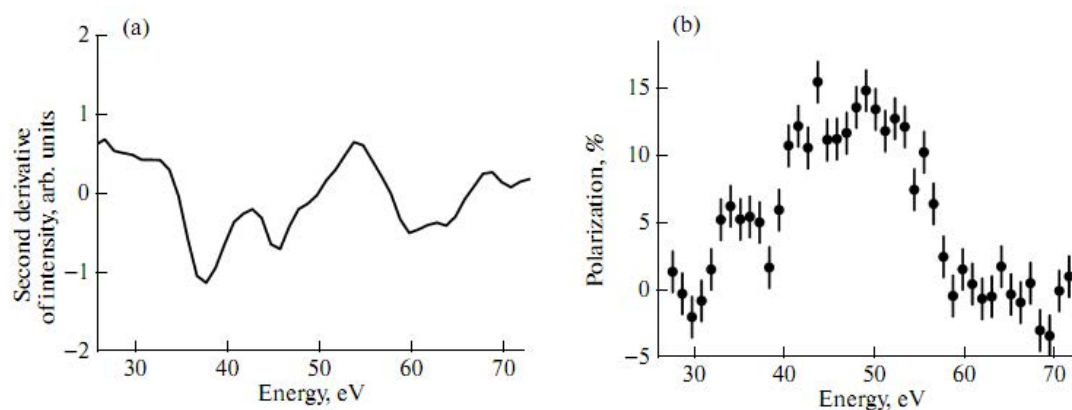


Fig.2.8 (a) second derivate iron Auger spectrum; (b) polarization of secondary electrons [46]

The  $L_{2,3}$  absorption spectra for different polarisation directions can be calculated using the method described by van der Laan & Thole (1991) and from these the X-ray Magnetic Circular Dichroism (XMCD) difference spectra can be derived. The XMCD spectrum of  $Fe_3O_4$  comprises three main components which are derived from the three sites occupied by iron:  $Fe^{2+}$  octahedral ( $d^6O_h$ ),  $Fe^{3+}$  tetrahedral ( $d^5T_d$ ) and  $Fe^{3+}$  octahedral ( $d^5O_h$ ). The  $Fe^{2+}$  and  $Fe^{3+}$  ions at the octahedral ( $O_h$ ) sites are aligned ferromagnetically and the  $Fe^{3+}$  ions at the

tetrahedral ( $T_d$ ) sites are coupled antiferromagnetically to those at the octahedral sites. See Fig.2.9, where the relative energy positions of the calculated spectra for the different Fe sites were shifted to obtain the best fit compared to experimental spectra; adding them with a ratio of 1 : 1 : 1 gives a good agreement with previously reported  $4.1 \mu_B$  per formula unit.

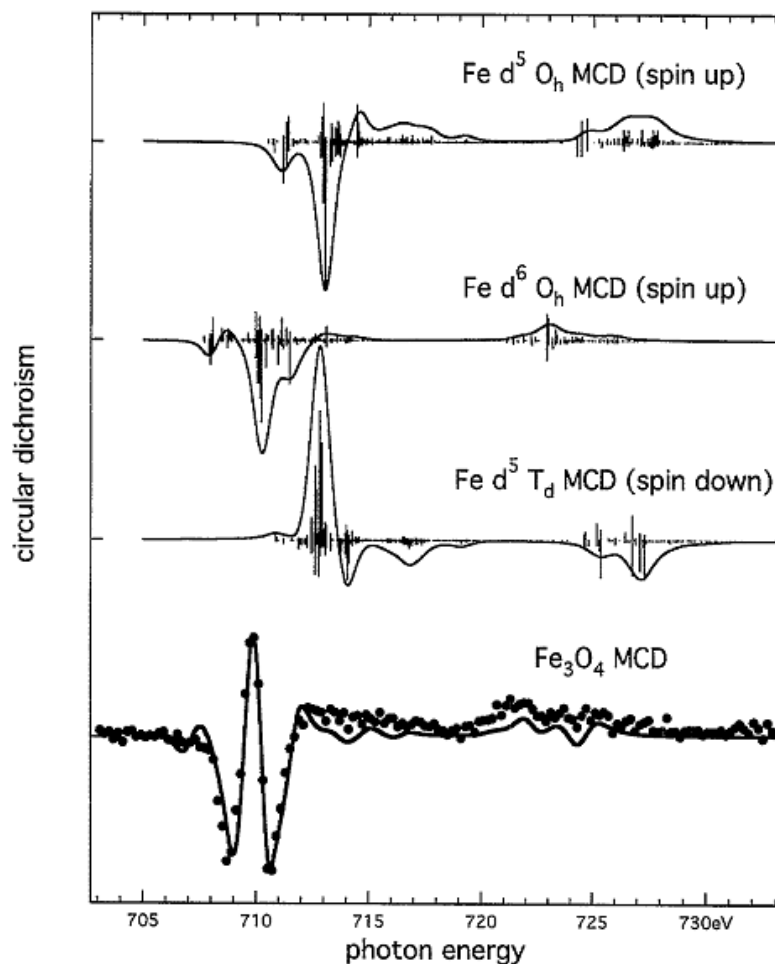


Fig.2.9 Calculated absorption diagrams for circularly polarized light at three different iron sites (upper panels). The bottom panel shows, the sum of individual spectra and is compared with experimental MCD.[47]

XMCD has been used in several experiments to determine the magnetic structure of magnetite in the literature. [48][49][50][51]

## 2.3 Electronic structure

### 2.3.1 Band structure calculation

As discussed in the first chapter, DFT is the most frequently used method for calculating strongly correlated systems, like  $Fe_3O_4$ . With this theory, the properties of a many-electron system can be determined by using functionals. The simplest approximation within DFT is the local-density approximation (LDA or LSDA if the spin is included), which is based upon exact exchange energy for a uniform electron gas, which can be obtained from the Thomas-Fermi model, and from fits to the correlation energy for a uniform electron gas.

Chapter 2: Overview of  $Fe_3O_4$ 

The first realistic band structure calculation of  $Fe_3O_4$  in the high temperature phase (i.e. above the Verwey transition) was carried out by Yanase and Siratori [52] in 1984 using the self-consistent augmented plane waves (APW) method. Only later on, Zhang and Satpahty [53] reported LSDA calculation using the self-consistent linear muffin-tin orbitals (LMTO) method. These two calculations show the metallic nature of magnetite. Electron band dispersion and the density of states (DOS) in the valence band calculated by LSDA are shown in Fig. 2.10 and 2.11. The oxygen 2p bands are located below -4 eV and from Fermi level to -4 eV is occupied by Fe 3d bands. The calculation predicts half metallic properties: by only one spin band ( $Fe_B t_{2g\downarrow}$ ) exists close to the Fermi level.

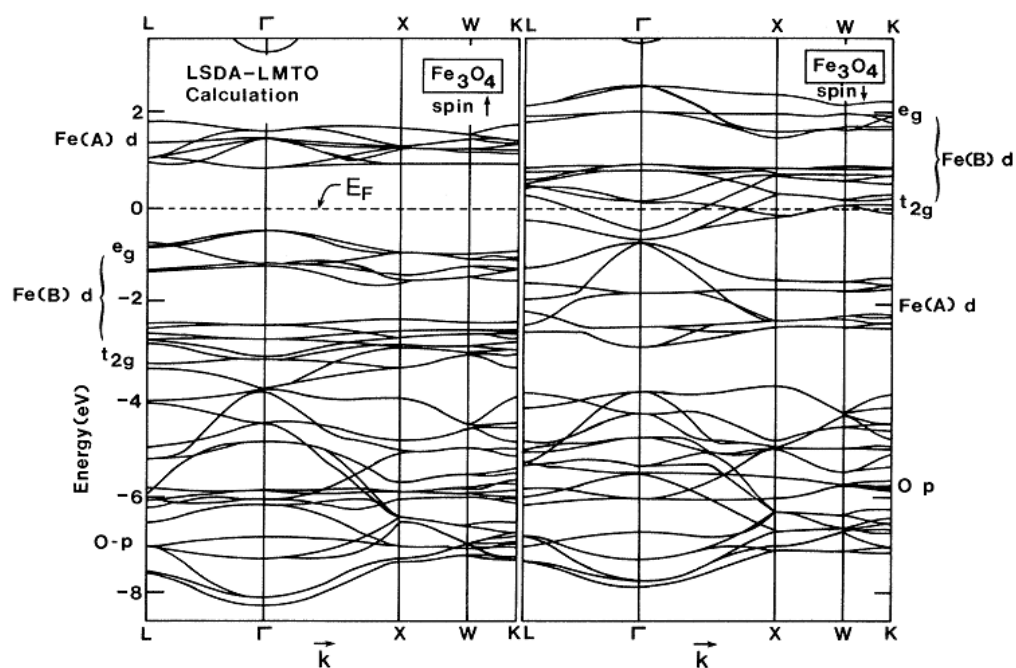


Fig.2.10 spin polarized electron bands obtained by LSDA [38].

In the band structure of  $Fe_3O_4$  the Hubbard-like effective potential,  $U_{\text{eff}}$ , is usually evaluated by comparison of theoretical and experimental positions of energy bands. Two types of Fe ions have different occupation numbers for 3d shell. As a consequence,  $U$  can be represented by Coulomb repulsion  $U_{\text{eff}}$ , describing the effective repulsion of 3d electrons (the strong on-site d-d electron-electron correlations) and depends on the number of holes in the shell. It will not influence the electronic structure, but the value of the energy gap. The LSDA+ $U$  method is started from a  $d^5(t_{2g\uparrow}^3 e_{g\uparrow}^2)$  configuration for  $Fe_A^{3+}$  ions on the tetrahedral site of the sub-lattice A and  $d^6(t_{2g\downarrow}^3 e_{g\downarrow}^2 a_{1g\uparrow}^1)$  and  $d^5(t_{2g\downarrow}^3 e_{g\downarrow}^2)$  for  $Fe_B^{2+}$  and  $Fe_B^{3+}$  ions on octahedral site of the sub-lattices  $B_1$  and  $B_2$  respectively [54].

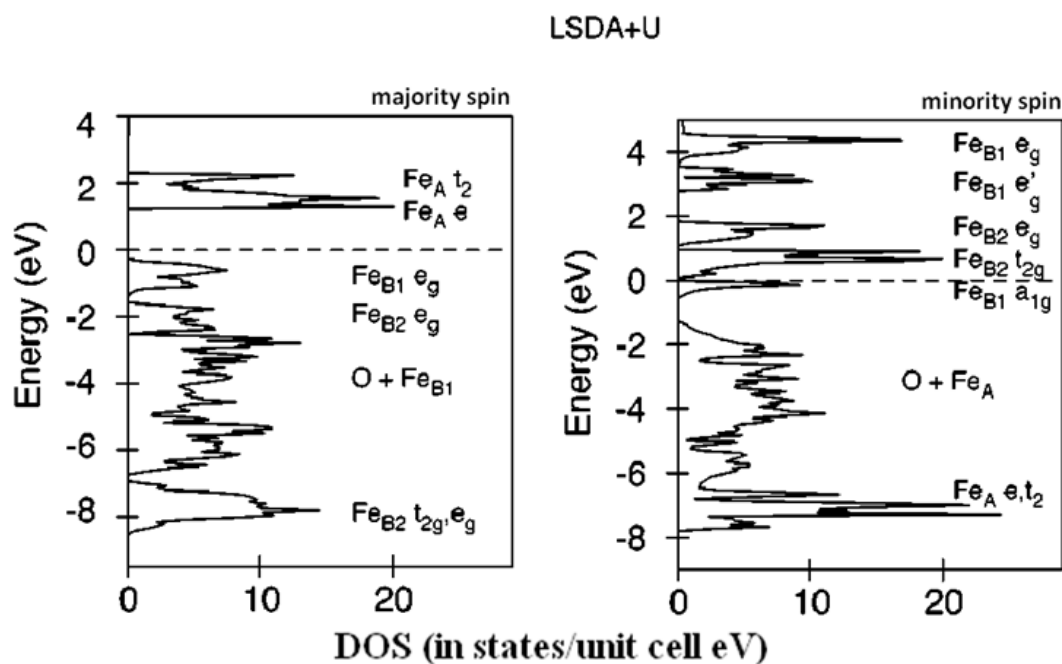


Fig.2.11 DOS of  $Fe_3O_4$  calculated by LSDA+U method [54]

The Fermi surface and the charge density were calculated in 1999 by Yanase and Hamada with a full potential linearized APW calculation within the LSDA [55]. The charge density obtained in the calculation is found to agree well with results from X-ray diffraction (XRD) studies and therefore supports the LSDA used in the calculation.

At temperatures below Verwey transition ( $T < T_V$ ) the calculation should be different from room temperature due to the different crystal structure of  $Fe_3O_4$ . In references [56][57] (See Fig.2.12) the bulk crystal below  $T_V$  was considered to be monoclinic Cc. The LSDA approach gives only a half-metallic ferrimagnetic solution without charge ordering. Partially filled bands at the Fermi level originate from the minority spin 3d- $t_{2g}$  orbitals of  $Fe_B$  cations. Apparently, only crystal structure distortion from cubic to monoclinic phase is not sufficient to explain metal-insulator transition and charge ordering in  $Fe_3O_4$ . In order to take into account the strong electronic correlations in the Fe 3d shell, the LSDA+U method can be used [57]. In contrast to LSDA, a charge ordered insulator with an energy gap of 0.03 eV was obtained. It is important to note that LSDA+U calculations performed for an undistorted P2/c phase of  $Fe_3O_4$  result in an insulating charge ordering solution that is compatible with the Verwey charge-ordering model.

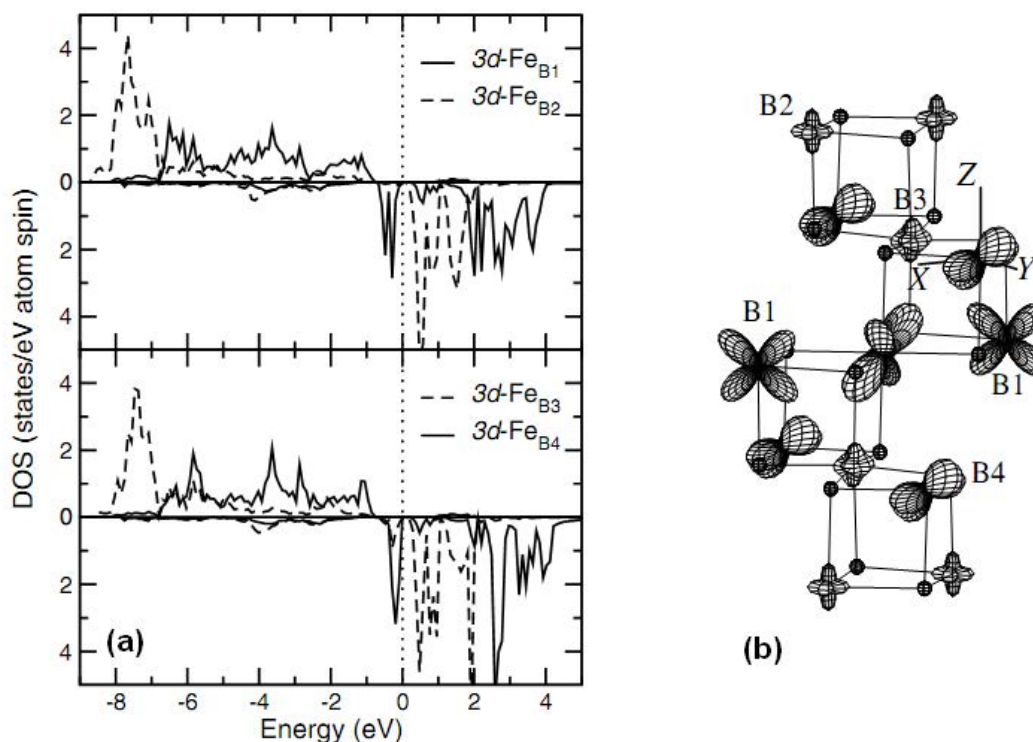


Fig.2.12 LSDA+U calculations for the low temperature P2/c phase of  $\text{Fe}_3\text{O}_4$ . (a) Partial DOS obtained from the with  $U=5$  eV and  $J=1$  eV (b) Angular distribution of the minority spin 3d electron density of  $\text{Fe}_B$  cations [57]

### 2.3.2 Experimental determination of the electronic structure by photoemission

The interpretation of early photoemission studies of iron oxides was based on the localized electron point of view. It was considered that the oxygen ligand field splits the localized 3d cation levels that will determine the main feature of PE spectra. Moreover, for iron oxides and other transition metal oxides, the 3d electrons are more localized than in the corresponding metals, and hence the 3p absorption spectra from the oxides exhibit more distinct multiplet features. It appears therefore that the resonant PE performed across the Fe  $3p \rightarrow 3d$  excitation threshold can be an appropriate technique. In reference [58] it was possible to partially separate the contributions to the resonant PE in  $\text{Fe}_3\text{O}_4$  from  $\text{Fe}^{2+}$  and  $\text{Fe}^{3+}$  ions by taking difference curves from EDC's measured with on- and off-resonant photon energies of the corresponding iron valences. In Fig.2.13, the 57-54 eV difference spectrum enhances the final states from the  $\text{Fe}^{2+}$  cations. Likewise, a 58-55 eV difference spectrum highlights the  $\text{Fe}^{3+}$  related features, although some intensity from  $\text{Fe}^{2+}$  cations is still included. The authors concluded that the occupied states near the Fermi level are mainly of  $3d^n \underline{L}$  (ligand hole) character and that all iron oxide phases should be classified as charge transfer insulators (charge transfer between the cation 3d and the ligand 2p orbitals).

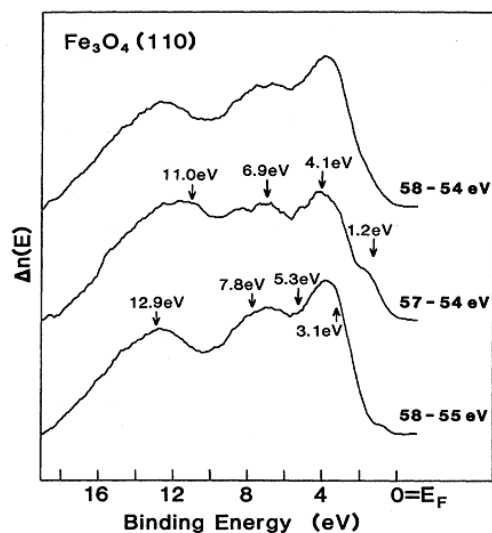


Fig. 2.13 Fe 3d derived final states in  $Fe_3O_4$  (110) determined in resonant photoemission by differences between EDC's measured at 58 eV and 54 eV, at 57 eV and 54 eV (emphasizing  $Fe^{2+}$  features), and at 58 eV and 55 eV (emphasizing  $Fe^{3+}$  features) [58]

In the itinerant electron model, the anisotropy and translation symmetry of the crystal is taken into account to explain the band dispersion of  $Fe_3O_4$ . A. Yanase and K. Siratori [52] et al observed finite intensity at the Fermi level, which indicated that  $Fe_3O_4$  is a metal rather than an insulator, in agreement with the band structure calculation. Although energy band dispersion, predicted by the calculation, was not clearly observed, it was concluded that the itinerant electron description is more appropriate than the ionic model for describing the electronic structure of  $Fe_3O_4$ .

To my knowledge, only 2 papers report on band dispersion, as seen by ARPES. In both papers the (111) surface was studied, there is no result concerning the dispersion on the (100) surface.

In the work of Cai et al [59], the valence band structure of a  $Fe_3O_4$  (111) surface along the  $\Gamma \rightarrow L$  symmetry line was studied. The dispersion of the minority spin bands near the Fermi level predicted by the calculation was clearly observed (Fig. 2.14). Together with the finite intensity at Fermi level confirm the metallic nature of  $Fe_3O_4$ . Although a defect can contribute to intensity at Fermi level through impurity scattering of photoelectrons, the valence bands show considerable variation both in intensity and spectral line shape as a function of photon energy. On an expanded scale (Fig 2.14 b), one identifies two bands, which correspond to the first two occupied minority spin bands in the calculation, both of which disperse upward towards the zone boundary. The feature of emission from the majority spin bands near the  $\Gamma$  point are not seen, maybe due to the low spectra weight.

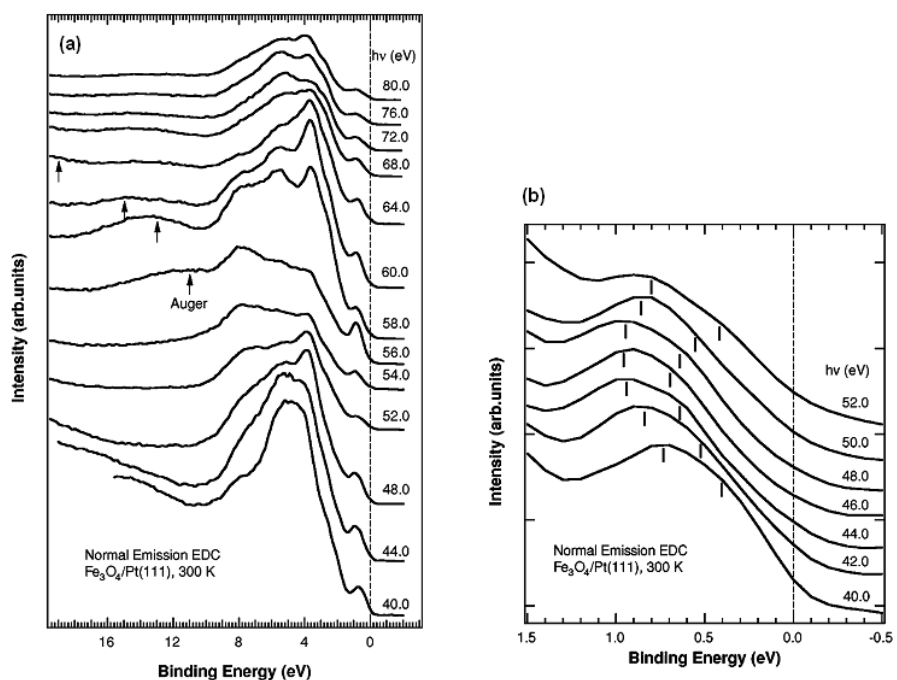


Fig.2.14 (a) Normal emission spectra from the valence bands of  $Fe_3O_4$  taken at room temperature; (b) A selection of normal emission spectra show the dispersion of the lowest binding energy feature (indicated by the vertical bars). The turning point in the dispersion corresponds to the  $\Gamma$  point [59]

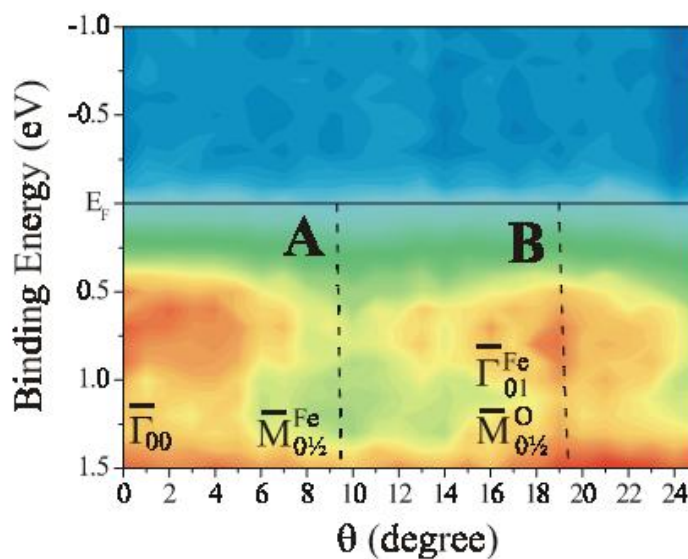


Fig.2.15 ARPES spectrum of  $Fe_3O_4(111)$  thin film obtained with photons of 58 eV (at 3p-3d resonance) at room temperature along  $\bar{\Gamma} \rightarrow \bar{M}$  direction. Line A represents the surface Brillouin zone (SBZ) limit of the iron sub-lattice, line B represents the SBZ border of the oxygen sub-lattice. [60]

Another ARPES study of the  $Fe_3O_4(111)$  thin film is presented by an intensity image plot giving a richer information than the profile plot [60] (see Fig.2.15). Photon energy of 58 eV, corresponding to Fe 3p $\rightarrow$ 3d resonance, was used in order to increase photoemission intensity from Fe 3d states near  $E_F$ . For interpretation of their data the authors considered the  $Fe_3O_4(111)$  surface band structure to be composed of two overlapping contributions corresponding

to symmetries of oxygen and iron sub-lattices. The oxygen sub-lattice is two times smaller than the iron sub-lattice. The limits of both surfaces Brillouin zones (SBZ) sub-lattices are shown in fig.2.15. Fe 3d-derived states show only a small periodic dispersion near  $E_F$ .

### 2.3.3 Half-metallic properties: spin resolved photoemission

The ultimate task of determination of the half metallicity is measuring the spin polarization at Fermi level. There are few techniques that measure the spin polarization. Andreev reflexion (AR) is one of them [61]. This technique is based on the idea that the Andreev process is inhibited due to inability to form electron pairs in the superconductor and impossibility of single-particle transmission, if only one spin band is occupied by the conduction electrons. As not all of the conductance channels are open for AR, the Andreev current is partially suppressed [62]. This kind of measurement must be performed at a temperature much lower than the  $T_V$  of  $Fe_3O_4$ . At this temperature,  $Fe_3O_4$  becomes an insulator and no spin polarization can be measured. Then spin-resolved photoemission measurement becomes the first option.

The first spin resolved photoelectron investigation of  $Fe_3O_4$  single crystals were performed by Alvarado et al. [63] (see Fig.2.16). Measurements of photoelectron spin polarization allowed the authors to see whether an electron was excited from a metal ion in the A or B sub-lattice, and to distinguish between excitation of p and d electrons. In other words, the measurement can distinguish the magnetic (Fe 3d) and nonmagnetic electrons (O 2p). They performed the measurement with photon energy up to 11 eV. The results were in good agreement with a calculation made on the basis of the single ion in a crystal field (SICF) model. According to the SICF model, the photoelectron excitations depend on the energy of the  $3d^{n-1}$  derived state of the metal ion left behind. This model predicts that in the binding energy region between 1.5 eV and the Fermi level, the electronic states correspond to the ionic configuration based transition of  $Fe^{2+}$ . As derived in this model, the maximum of the spin polarization at  $T=0$  K is -66.6 %.

From this experiment up to today, the experimental technique improved and the problem of preparation of transition metal oxide thin films with well-defined stoichiometry on the surface has been solved. Spin-resolved PES measurements of  $Fe_3O_4$  at high temperature ( $T > T_V$ ) were carried out, but there is still a controversy about the half-metal properties of  $Fe_3O_4$ . Kim et al, [49] carried out SRPES on epitaxial  $Fe_3O_4$  (111) thin films grown on the Fe (110) surface. They found a larger PE intensity a Fermi level as compared to bulk  $Fe_3O_4$ . This was attributed to a possible formation of oxygen deficient  $Fe_3O_4$  surface. A spin polarization of 16 % at Fermi level was obtained. Such a small value indicates that the thin films do not have the  $Fe_3O_4$  stoichiometry.

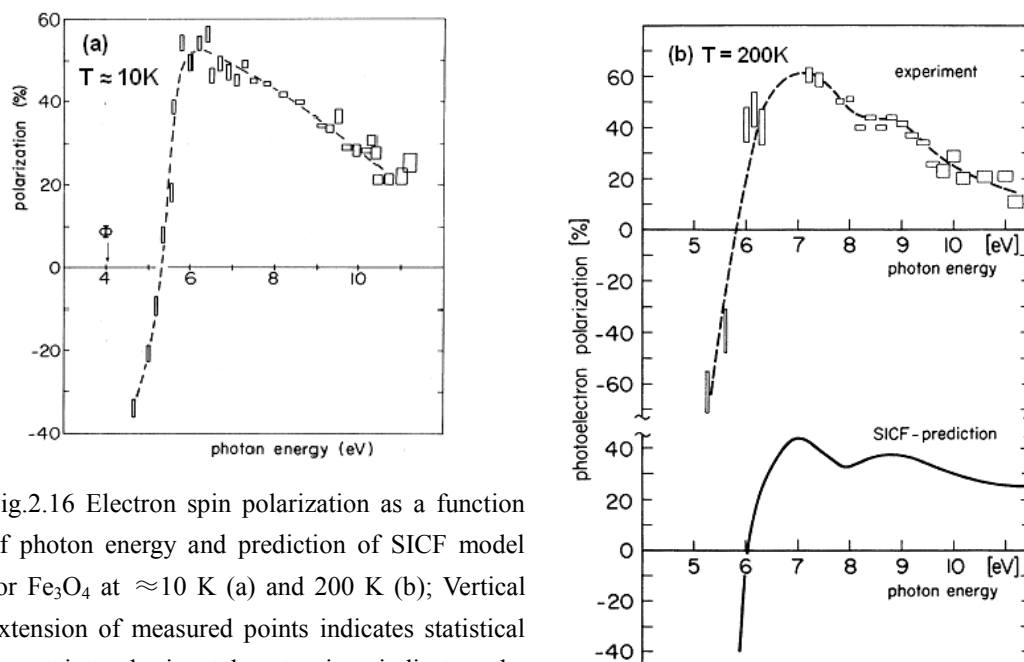


Fig.2.16 Electron spin polarization as a function of photon energy and prediction of SICF model for  $Fe_3O_4$  at  $\approx 10$  K (a) and 200 K (b); Vertical extension of measured points indicates statistical uncertainty, horizontal extension indicates the resolution of monochromator. [63]

D.J. Huang et al [50] presented evidence against half metallicity of  $Fe_3O_4$ . They did in situ spin-resolved photoemission on  $Fe_3O_4(100)/MgO(100)$  epitaxial films (see Fig.2.17). A spin polarization of -40 % was found near Fermi level. It was suggested that the magnetic moments at the (100) surface might be reduced due to the surface reconstruction. Taking into account this reduction in the spin moment, the spin polarization of the state was normalized to -55.5 %. However even this value is significantly lower than the LSDA and GGA calculations suggest. Consequently, the authors concluded that this discrepancy results from the strong electron correlation effects (the maximum polarization is up to -66.6% [63]) and  $Fe_3O_4$  should not be considered as half-metal.

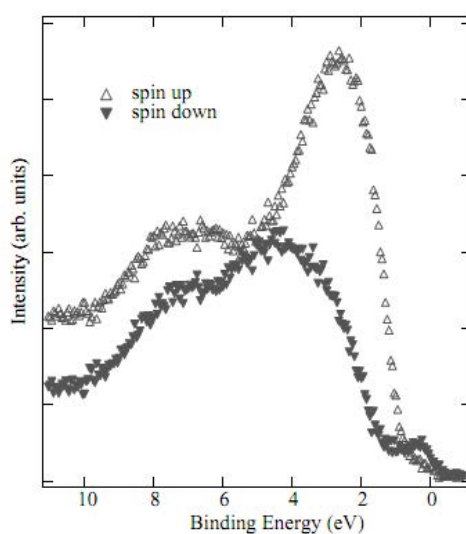


Fig.2.17 Spin-resolved photoemission spectra of  $Fe_3O_4(100)$  on  $MgO(100)$  measured with 450 eV photon energy [50].

Chapter 2: Overview of  $Fe_3O_4$

In the same year, M. Fonin et al obtained a spin polarization of 80 % at Fermi level on the (111) surface at room temperature [64] (Fig. 2.18). This ruled out the ionic configuration based approach giving the upper limit of -66.6 % at the temperature of 0 K [63] [65]. Moreover, the authors found an agreement of the photoemission spectra with DFT calculations, predicting an overall energy gap in the spin-up electron bands and provided in such a way the evidence for a half-metallic ferromagnetic state of  $Fe_3O_4$ .

For the  $Fe_3O_4$  (100) surface, the same group observed a spin polarization of -55 %, similarly to [65], see Fig. 2.19. The reduced polarisation was explained by a surface reconstruction [66][67][68], the ultimate layer being not half-metallic.

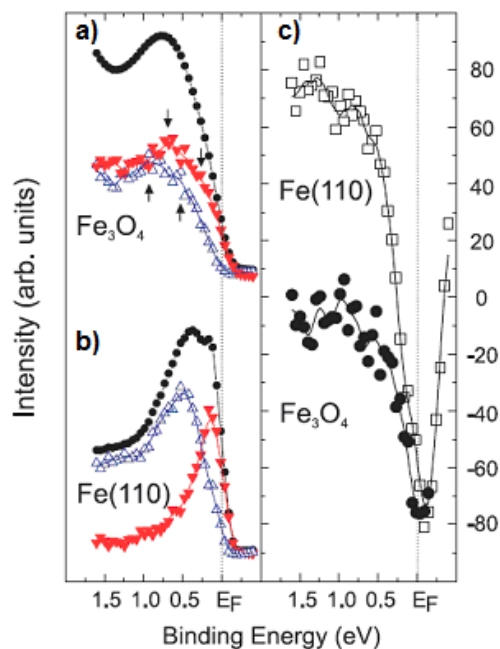


Fig.2.18 Spin-resolved, normal-emission spectra measured with  $h\nu = 21.2$  eV of (a)  $Fe_3O_4(111)/Fe(110)/W(110)$  (b)  $Fe_3O_4(111)/Fe(110)/Mo(110)/Al_2O_3(1120)$ . Red filled triangle represents spin down, blue open triangle represents spin up and filled circle represents the total electron. (c) Spin polarization: open and filled symbols squares correspond respectively to (a) and (b); [64].

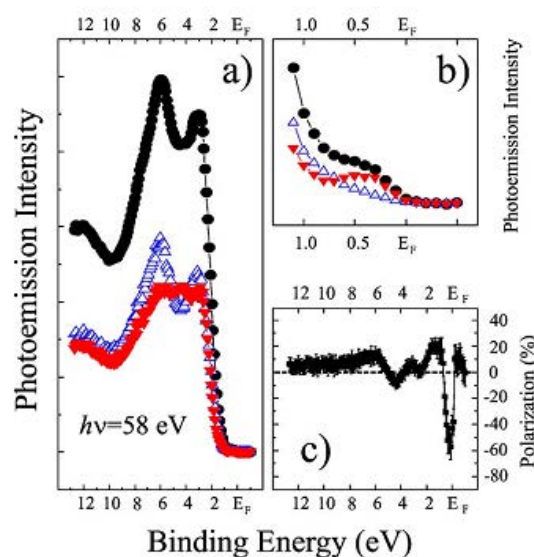


Fig.2.19 (a) Photoemission spectrum of  $Fe_3O_4(100)/MgO(100)$  (black) taken with 58 eV photon energy at normal emission. Spin up (blue) and spin down (red) photoemission intensities are also shown. (b) Detail of near  $E_F$  region. Red filled triangle represents spin down, blue open triangle represents spin up and filled circle represents the total electron. (c) Spin polarization. [67]

On the contrary, J. G. Tobin et al [69] suggest a strong electron correlation as a reason for measured low spin polarization. His research group obtained the spin polarization of -30 % to -40 % at the Fermi edge using different photoelectron take-off angles at various photon energies. This is consistent with the value of -65 % corresponding to the underlying bulk and agrees with the predicted electron correlation effects. Their main argument is that ARPES cannot bring a proof of half-metallicity because it is not averaging over the whole Brillouin zone. According to them, half-metallicity requires that the entire density of states has one spin

only. However, the samples of Tobin et al were prepared by ion sputtering or transferred ex situ to the UHV system that could lead to a surface contamination and/or to reconstructed magnetically dead surface layers. Ill-defined surface properties may obscure the intrinsic properties of  $Fe_3O_4$ .

Clearly, the polarization at Fermi level reported in the literature is much lower than -100 %. As we will discuss in chapter 5, there are several reason for this reduction. Except the quality of samples (surface contamination or defect etc.), intrinsic effects of the photoemission process as the life-time of the photohole and the interaction with the lattice (polarons) are major ingredients that reduce the spin polarization.

### 2.3.4 Verwey transition

A lot of experiments were carried out to understand the electronic structure of  $Fe_3O_4$  and the changes that occur following the Verwey transition. The original hypothesis of the Verwey transition is that we consider  $Fe_A^{3+}[Fe^{3+}Fe^{2+}]_B$  as  $Fe_A^{3+}[Fe^{3+}Fe^{3+} + e^-]_B$ . Conduction is then a matter of thermally activated electron hopping amongst adjacent  $Fe^{3+}$  sites. When the temperature is getting lower, the thermal fluctuation is decreased and the electron becomes unable to overcome the hopping barrier; there the Verwey transition occurs.

At this point it is worth to mention that there are several models describing the mechanism of electrical conduction in  $Fe_3O_4$ . Cullen and Callen proposed a simple model in which the “extra” electrons on the B sites move in a non-degenerate spin-less band [70]. Minimizing the coulomb repulsion between the hopping electrons is known as the Anderson model condition. Yamada and Chakraverty seem to favour the idea of molecular polarons or bipolarons [71][72]. All of these models and calculations focused almost entirely upon explaining the transport measurements. Local spin density approximation and dynamical mean field theory into the first-principle, Density Functional Theory, has been used to derive the electron interaction and hopping parameters. The exact mechanisms of electronic charge transport and the precise microscopic interactions within various temperature ranges are still under discussion.

In an early photoemission study, Chainani et al [73] observed that below  $T_V$  a clear gap in DOS exists at  $E_f$ . This gap was found closed above the transition temperature. The spectral weight at  $E_f$  was found to increase with temperature, suggesting that a degree of short-range order persists just above  $T_V$ . This gives way to fully metallic behaviour at room temperature. In Fig.2.20 (b), the 140 K spectrum is shifted (dotted line) to superimpose on the 100 K spectrum to show the changes across  $T_V$ . The feature d decreases in intensity and feature e increases. The most important change is observed at the Fermi level in the inset of Fig.2.20 (b). The 100 K spectrum shows a gap in the DOS of 68 meV.

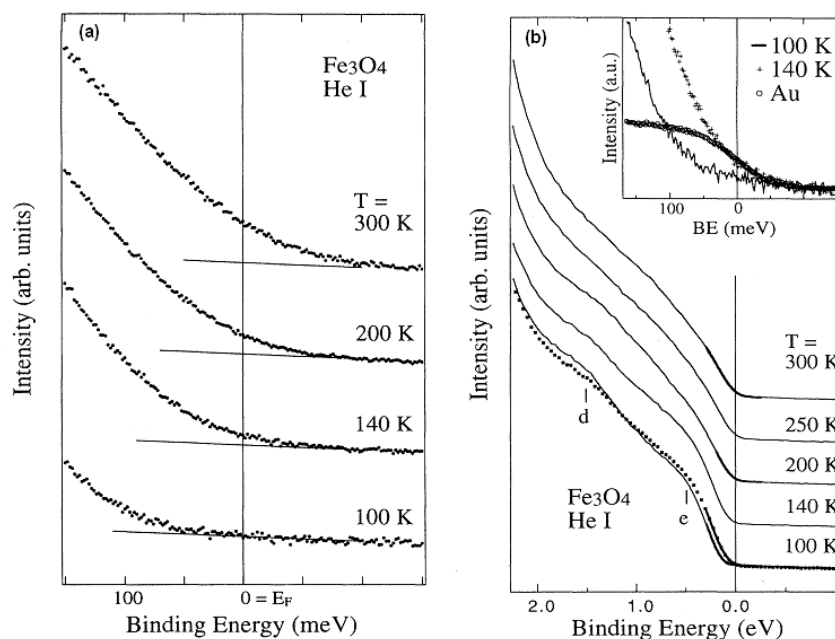


Fig.2.20 (a) Temperature dependence of  $Fe_3O_4$  spectra near  $E_F$  showing systematic increase in the DOS at  $E_F$  with temperature. (b) Fe 3d- $e_g$  and 3d- $t_{2g}$  states of the B sub-lattice, marked d and e respectively, as a function of temperature. Inset shows the detail of the semiconductor-metal transition unravelling a gap of  $\sim 70$  meV at 100 K and a finite DOS at  $E_F$  at 140 K [74].

Lad and Henrich [74] have measured similar spectra, which revealed the existence of Fe 3d derived features at binding energies of 0.5 eV and 1.5 eV. These features are resolved below  $T_V$ , and also above (at 140 K) it. The finite DOS at  $E_F$  for  $T > T_V$  and its absence for  $T < T_V$  is consistent with the first order metal-insulator transition and with the change of two orders of magnitude in electrical resistivity due to a variation in free carrier concentration. This is a direct observation of the changes as a function of temperature in the DOS at and near Fermi level and clarifies the role of short-range-ordering in  $Fe_3O_4$ .

J.H. Park et al [75] have found contradictory results. Their observation indicates that the gap didn't collapse and the spectrum intensity at the Fermi level remains zero just above  $T_V$ . (See Fig.2.21) The loss of long-range order reduces the gap by  $\sim 50$  meV on heating through  $T_V$  and this reduction of the gap is consistent with both the conductivity jump in a semiconductor picture. The spectra of both phases merge smoothly with the background well below Fermi level and do not show a Fermi step. They conclude that the gap is not eliminated in the Verwey transition but the threshold energy is shifted by  $\sim 50$  meV to lower binding energy. This finding is consistent with the conductivity jump at the transition and with other evidence for a small carrier density at room temperature. Although short-range-ordering continues to maintain a gap against free carrier generation above  $T_V$ , it appears that carriers so generated are much more mobile than in the incoherent hopping model.

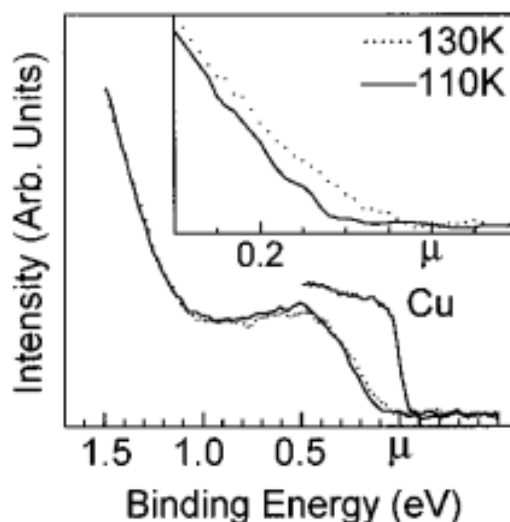


Fig.2.21 Spectrum in the region near the chemical potential. Inset: detail feature of valence band PES spectrum of  $\text{Fe}_3\text{O}_4$  at 110 K (dashed) and 130 K (dotted). Including a reference spectrum showing the sharp Fermi edge of Cu metal. [75]

The importance of surface order for Verwey transition of  $\text{Fe}_3\text{O}_4(111)$  surface was studied by Jordan et al [76]. They used scanning tunnelling spectroscopy (STS) to obtain information on occupied and unoccupied states of the surface. The comparison of the results above and below Verwey transition temperature showed the surface doesn't exhibit a metal-insulator transition that is completely different from bulk.

In order to investigate intrinsic properties of Verwey transition of  $\text{Fe}_3\text{O}_4$  by electrons (i.e. by photoemission) a long mean free path is needed. According to the "universal curve" (See Fig.3.13), either very low, or very high photon energies are required.

Schrupp et al [77] performed soft X ray PE (large mean free path of  $\sim 45 \text{ \AA}$ ) on the fractured surface for temperature within a small interval of temperatures around  $T_V$ . They found neither indication of a metallic Fermi edge nor a quasi-particle feature in the high temperature phase. (see Fig.2.22) The inset profile shows that the onset energy  $E_{\text{on}}$  (defined in Fig. 2.22) jumps exactly at  $T_V$  and is consistent with the hysteretic behaviour of the conductivity, confirming that these spectra reflect intrinsic bulk behaviour. The authors believe that previous PE studies, besides being strongly surface sensitive, used rather wide temperature steps, so that the reported effects resulted from the gradual temperature evolution and not from the Verwey transition. They describe the charge carriers in  $\text{Fe}_3\text{O}_4$  as small polarons and the physics of Verwey transition contains elements of a cooperative John-Teller effect, which requires additional stabilization by local d-d Coulomb interaction.

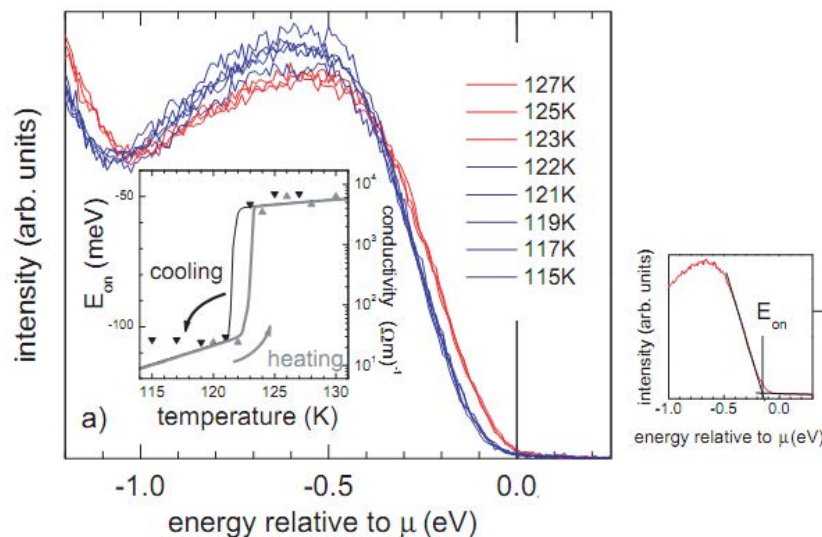


Fig.2.22 Spectra of the fractured sample taken around the Verwey transition. Inset: spectral onset energy during cooling (down-triangles) and heating (up-triangles) and the conductivity hysteresis (solid curves) measured on the same sample; the definition of onset energy  $E_{on}$  is shown on the right panel [77].

Masato Kimura et al [78] performed bulk sensitive photoemission using hard X-ray (8 keV) and extremely low (7.5 eV) photon energies. They didn't observe a clear Fermi edge above  $T_V$  either and the detailed spectra (Fig.2.23) measured at different temperatures indicate that the electronic states of  $Fe_3O_4$  vary gradually above  $T_V$  with negligible intensity at Fermi level. This temperature dependence can be well explained by considering the formation of the polaronic quasi-particle due to the electron-phonon coupling. Since this coupling strength becomes weaker at high temperature far from  $T_V$ , the intensity at Fermi level increases inducing the increased conductivity of  $Fe_3O_4$  at high temperatures.

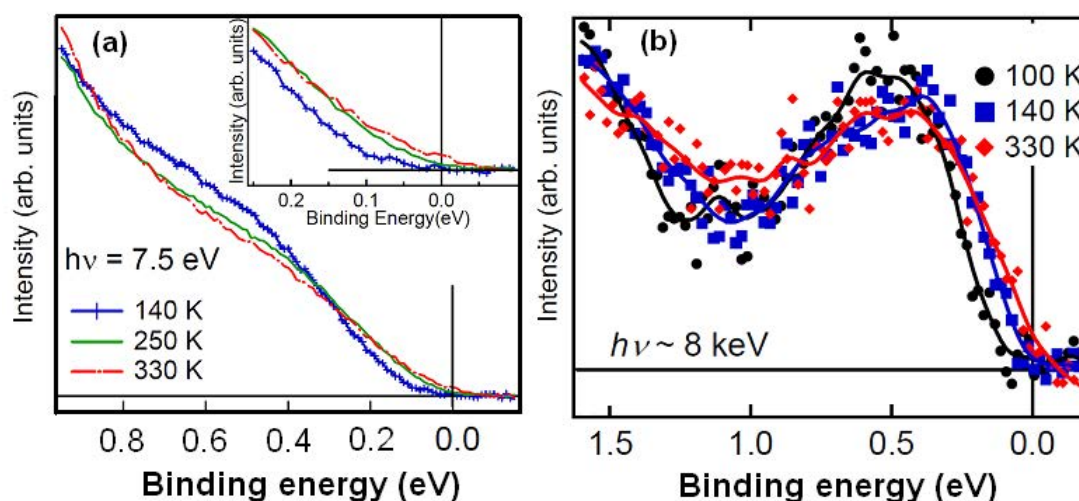


Fig.2.23 (a) Temperature dependence PES spectra of  $Fe_3O_4$  at a) low photon energy and (b) with hard X-ray [78].

# Chapter 3:

---

---

## Experimental aspects

---

---

### 3.1 Synchrotron Radiation Source

Determination of the bulk and surface electronic structure by photoemission requires variable photon energy that is available only in synchrotron radiation centres.

The main part of results presented in this thesis has been done at the CASSIOPEE beamline (Combined Angular- and Spin-resolved Spectroscopies Of PhotoEmitted Electron ) at SOLEIL, French national synchrotron facility. The CASSIOPEE is divided into two branches and is dedicated to high resolution ARPES, spin-resolved photoemission and resonant spectroscopies in the 8-1500 eV photon energy range with 20-70 meV energy resolution depending on the photon energy. This wide energy range allows both surface and bulk studies of condensed matter. The beamline uses two undulators as a source with high flux and adjustable polarization. The flux on the sample is  $10^{13}$  photon/s/0.1% BW. Both analyser chambers are connected to a Molecular Beam Epitaxy chamber for sample growth and characterization. This allowed us to prepare in-situ  $\text{Fe}_3\text{O}_4$  thin layers.

Several other experiments have been performed at three different beamlines of ELETTRA, the Italian synchrotron radiation facility.

ARPES experiments with low photon energies (6 – 25 eV) were done at the BaD ElPh (Band dispersion and electron-phonon coupling) beamline. Low photon energies provide enhanced bulk sensitivity, since the inelastic mean free path is expected to increase for the electrons with kinetic energies below 10 eV. The beamline is based on a 4m normal-incidence monochromator (NIM) that is fitted with three interchangeable spherical gratings to cover the photon energy range 4.6-40 eV at 2.0 GeV of electron ring energy. The same as at CASSIOPEE beamline, the samples were prepared in-situ and characterized by LEED and XPS (Mg and AL  $K\alpha$  radiations).

Some of the samples were further characterized by X-ray absorption spectroscopy (XAS) and X-ray Magnetic Circular Dichroism (XMCD) experiments. These techniques are available at the BACH (Beamline for Advanced DiCHroism) beamline. For these measurements it was necessary to transfer the samples through the atmosphere.

BACH beamline is conceived and optimized to perform spectroscopy experiments in the UV-soft x ray (35eV-1600eV) photon energy range with variable light polarization (linear horizontal, linear vertical, circular) delivered by two APPLE-II undulators. The high resolving power (20000-6000 in the entire energy range) is obtained by the use of three variable-angle spherical gratings. The photon flux in the experimental chambers, calculated at the best resolutions achievable, is expected to be above  $10^{11}$  photons/s with linearly or circularly polarized light.

Very recently we performed a Fermi surface mapping at the VUV photoemission

### Chapter 3: Experimental aspects

beamline that has been designed for surface and solid state experiments. The light source is an undulator with energy range of 17 to 1000 eV and the monochromator is equipped with five interchangeable spherical gratings.

Another series of Fermi surface mapping was done at the ADDRESS (ADvanced REsonant SpectroScopies) beamline of SLS (Swiss Light Source), Paul Scherrer Institut in Villigen. The beamline is an optimized soft X-ray spectroscopy user facility for soft X-ray RIXS and ARPES and delivers photons with variable polarization (circular and linear) between 0.4 and 1.8 keV with high resolving power up to the design value of 28000 near 1 keV. The theoretical flux of 1keV photons on the sample ranges from  $3 \times 10^{11}$  to  $1 \times 10^{13}$  photons/s/0.01%BW for a resolving power of 28000 and 7000, respectively.

## 3.2 Laser Source

Laser source allowed us to perform spin-resolved and time-resolved (pomp-probe) experiments using an electron Time of Flight Spin (ToF-Spin) analyzer. Photoelectron spectroscopy was carried out in the experimental chamber built by C. Cacho [79] and installed in the T-Rex laboratory at Elettra. The TOF analyser (see Fig. 3.1) incorporates electron optics to decelerate electrons into a drift tube of 25 cm length, followed by another electron optic assembly to refocus the electron beam.

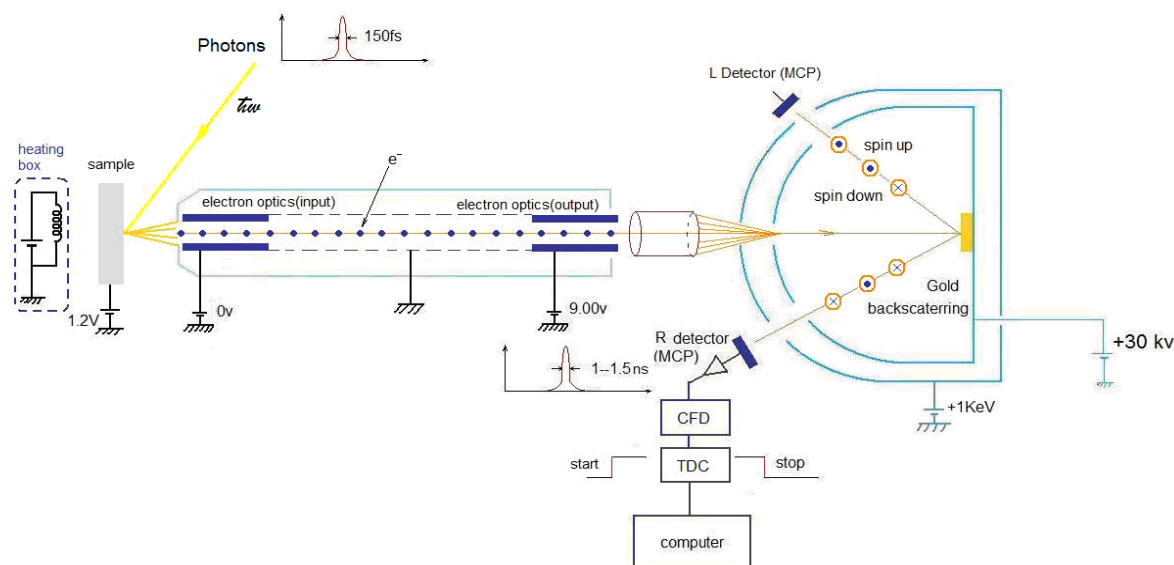


Fig.3.1 View of experimental configuration of TOF analyser and Mott detector. After amplification the laser operates at 250 kHz producing photons with wavelength of 800 nm and power of around 1 W. The 4th harmonic (200 nm) is generated in phase matching conditions, with a pulse length of 150 fs.

The horizontal and vertical transverse spin polarisations of the electron beam are detected by a four-channel retarding field Mott polarimeter. The spin selectivity of the Mott detector (Sherman function) is estimated to be 15%. The experimental asymmetry is removed by reversing the magnetic state of the sample and repeating the measurement. Following deceleration in the input electron optics, the electrons travel with 6 eV kinetic energy in the drift tube. The time taken for an electron to travel from the sample surface to any of the

Chapter 3: Experimental aspects

detectors is measured with a time digitisation of 120 ps, it is then converted to kinetic energy. In the long time of flight region, consecutive data points are merged together to ensure a minimum kinetic energy variation of 20 meV between each point after conversion. The time-to-energy calibration is determined through a fit of the vacuum cut off time position versus the sample voltages. (See §3.3.2.4)

The laser consists of a Ti:SA oscillator (Mira Seed) and a high repetition rate Ti:SA amplifier (RegA). The oscillator is synchronizable to an external RF signal. The oscillator output consists of pulses with the following specifications:

	Before the amplification	After the amplification
wavelength	800 nm (tunable in 780-840 nm)	800 nm
bandwidth	40 nm	26 nm
Average power	800 mW	1.1 W
Pulse duration	100 fs	150 fs
Repetition rate	80 MHz	250 kHz

An optical set up has been realized to generate the 4th harmonic of the laser,  $\lambda = 200$  nm, in phase matching conditions, to serve an experimental chamber for spin resolved ARPES and also pump-probe measurement. The pump-probe scheme uses 50mW of the RegA output ( $\lambda = 800$  nm) as pump beam, while the Optical Parametric Amplifier (OPA) output is used as probe beam. A general layout of the experimental configuration is shown in Fig. 3.2, we did our measurements in the chamber denoted “10”.

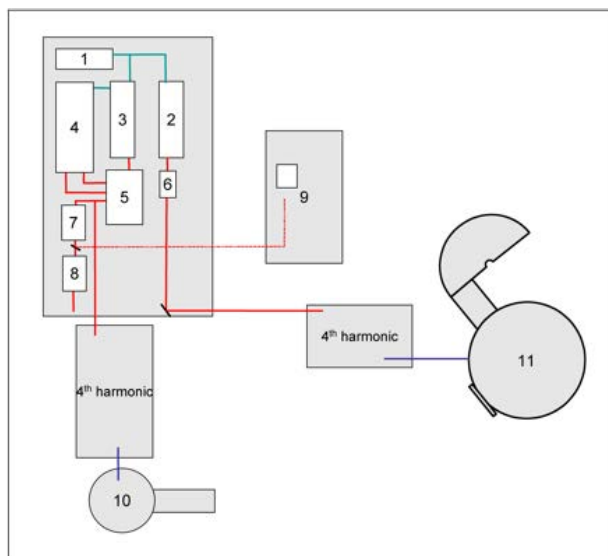


Fig.3.2 Laser laboratory setup: 1 -8 laser delivering 800nm beam with repetition rate of 250 kHz. 9: time-resolved optical spectroscopy; 10: SARPES and 11: ARPES

### 3.3 Experimental techniques

#### 3.3.1 Low Energy Electron Diffraction (LEED)

LEED experiments give direct information about the surface order. The energy of the electron beam used in diffraction experiments is in the range between 10 and 200 eV. According to the universal curve, the electron mean free path in solids for these energies is of the order of a nanometer or less, LEED is therefore a surface sensitive technique.

The relationship between scattered and incident electrons is described in reciprocal space defined by primitive reciprocal lattice vectors.

$$\vec{a}^* = \frac{2\pi \vec{b} \times \hat{n}}{|\vec{a} \times \vec{b}|}, \vec{b}^* = \frac{2\pi \hat{n} \times \vec{a}}{|\vec{a} \times \vec{b}|} \quad (3.1)$$

where  $\{a,b\}$  is the real 2D space lattice.  $\hat{n}$  is the normal vector for this 2D lattice. In Fig.3.3

(a),  $\vec{k} = \frac{2\pi}{\lambda}$ ,  $\vec{k}' = \frac{2\pi}{\lambda'}$ ,  $\vec{G} = h\vec{a}^* + k\vec{b}^*$  are incident electron wave vector, scattered wave vector and reciprocal vector, respectively. According to Laue condition,  $\vec{k}' - \vec{k} = \vec{G}$ , and  $|\vec{k}| = |\vec{k}'|$ .

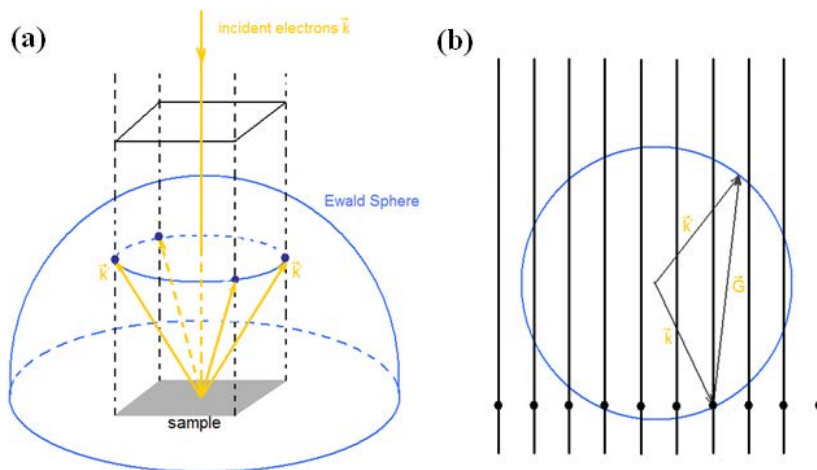


Fig.3.3 (a): The typical kinematic scattering model for LEED where the fluorescent screen is displayed as an Ewald's sphere. (b): Ewald's sphere construction for the case of diffraction from a 2D-lattice. The intersections between Ewald's sphere and reciprocal lattice rods define the allowed diffracted beams.

The Laue condition results in a construction of the Ewald's sphere, as shown in Fig.3.3 (b). A spot on the fluorescent screen will represent every wave vector that satisfies the Laue condition. The pattern observed on the fluorescent screen is therefore a representation of the reciprocal lattice. The size of the Ewald's sphere and hence the number of diffraction spots on the screen is controlled by the incident electron energy. From the knowledge of the reciprocal lattice, a model of the real space structure, at least qualitatively in terms of the surface periodicity and the point group, can be proposed.

The real configuration of LEED experiment is shown in Fig.3.4. The electrons from a

hot filament are focused on the sample surface. The hemispherical grids are acting as a high pass filter for energy of diffracted electrons. The electrons are then accelerated by a high potential onto a fluorescent screen on which the diffraction pattern can be directly observed.

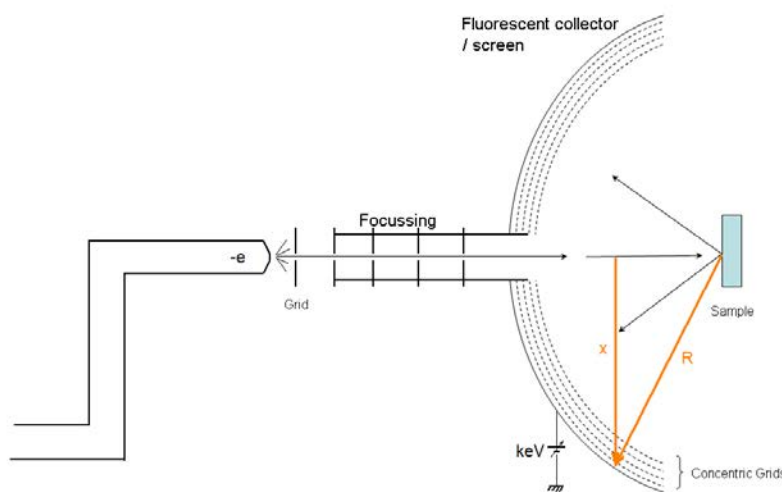


Fig.3.4 Simple scheme of typical LEED apparatus with two major components: an electron gun and a hemispherical detector system

The relationship between the constructive interference point which a distance measured from the centre of the screen is  $x$  and the electron energy  $E$  (eV scale) is:

$$\frac{x}{R} \cong 12.264 \frac{n}{d\sqrt{E}} \quad (3.2)$$

Where  $n$  is the diffraction order,  $R$  is the radius of the fluorescent screen and  $d$  is the lattice parameter ( $\text{\AA}$ ).

### 3.3.2 X-ray based absorption spectroscopy techniques

X-ray absorption spectroscopy (XAS) is a widely used technique for determining the local geometric and/or electronic structure of matter. The experiment is usually performed at synchrotron radiation sources, which provide intense and tuneable X-ray beams. XAS data are obtained by varying the photon energy using a crystalline monochromator to a range where core electrons can be excited (0.1-100 keV photon energy).

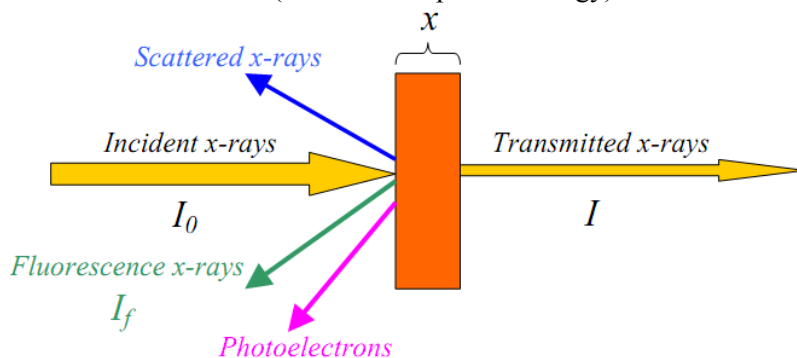


Fig.3.5 Schematic diagram of physical mechanism when a x-ray beam comes into a solid material

Chapter 3: Experimental aspects

When the x-rays hit the sample, the oscillating electric field of the electromagnetic radiation interacts with the electrons bound in an atom. Either the radiation will be scattered by these electrons, or absorbed and excite the electrons. As seen in Fig.3.5, a monochromatic x-ray beam of intensity  $I_0$  passing through a sample of thickness  $x$  will get a reduced intensity  $I$  according to the expression:  $\ln(I_0/I) = \mu x$ , where  $\mu$  is the linear absorption coefficient. In our case, the conventional XAS spectrum is very difficult to measure, because of the thickness of the sample and of the substrate. Therefore, the XAS spectra presented in this thesis were collected by measuring the total-electron-yield (TEY). TEY varies linearly with the x-ray absorption coefficient of the element.

Magnetic samples were characterized by X-ray magnetic circular dichroism (XMCD). XMCD is a change in photon absorption intensity either when the magnetization of the sample is reversed or when the light polarization is changed (from left to right circularly polarized light). A XMCD spectrum brings information on magnetic properties of atoms, such as its spin and orbital magnetic moments.

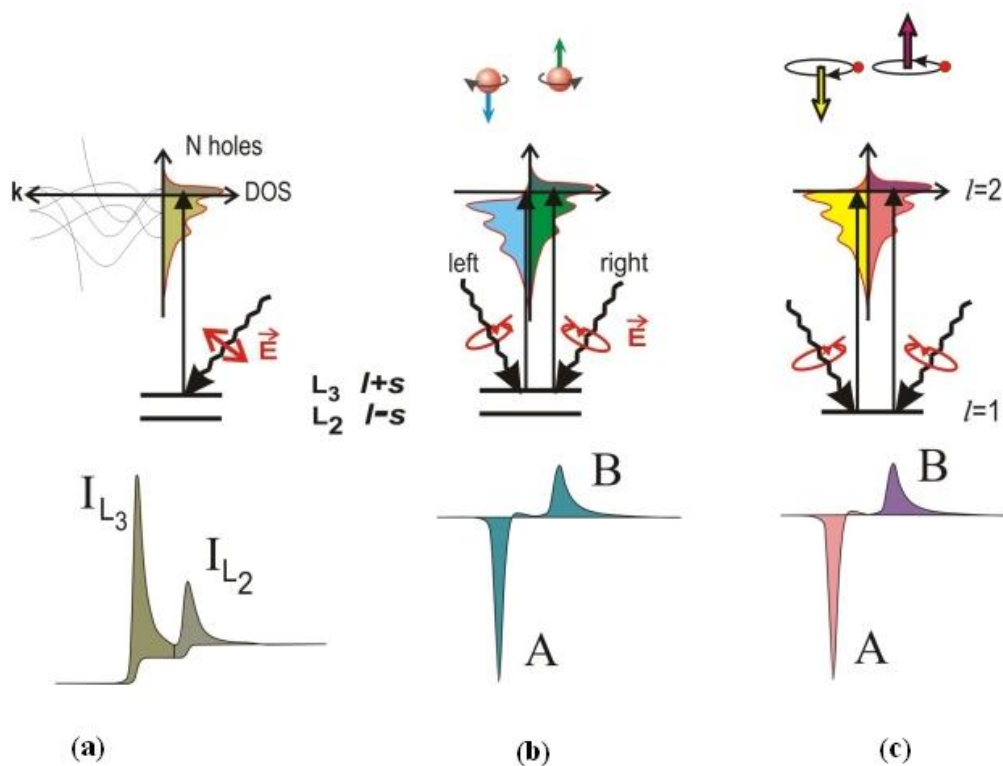


Fig.3.6 One electron configuration picture of an atom excited from spin orbit split p core shell to unfilled d states. (a) electronic transitions in conventional L-edge XAS; (b) and (c) XMCD, illustrated in a one-electron model. The transition occurs from the spin-orbit  $2p$  core shell to empty conduction band states. In conventional XAS, the total transition intensity of the two peaks is proportional to the number of d holes (first sum rule). By use of circularly polarized X-rays the spin moment (b) and orbital moment (c) can be determined from linear combinations of the dichroic difference intensities A and B, according to other sum rules [81]

Fig.3.6 shows the concept of XMCD spectroscopy. The total intensity of  $L_3$  and  $L_2$  resonances links to the number of empty d states (Fig.3.6 (a)). For a magnetic material the d shell has a spin moment which is given by the imbalance of spin-up and spin-down electrons.

### Chapter 3: Experimental aspects

In order to measure the difference in the number of d holes with up and down spin, the spin dependent x-ray absorption process is needed. This is done by use of right and left circularly polarized photons which transfer their angular momentum to the excited photoelectron. These photoelectrons carry the transferred angular momentum as a spin (Fig. 3.6 (b)) or an angular momentum (Fig.3.6 (c)) or both [80]. Since spin flips are forbidden in electric dipole transitions, spin-up (spin-down) photoelectrons from the p core shell can only be excited into spin-up (spin-down) d hole states. Hence the spin-split valence shell acts as a detector for the spin of the excited photoelectron and the transition intensity is proportional to the number of empty d states of a given spin. The quantization axis of the valence shell “detector” is given by the magnetization direction. The size of the dichroism effect scales like  $\cos(\theta)$ , where  $\theta$  is the angle between the photon spin and the magnetization direction. Hence the maximum dichroism effect (typically 20%) is observed if the photon spin direction and the magnetization directions are parallel and anti-parallel. By the use of circularly polarized x-ray, one can determine the spin moment and orbital moment from dichroic difference intensities A and B through powerful sum rules. [82] For spin moment, it is quantitatively linked to the measured intensity  $A - 2B$  and by summing over A and B ( $A + B$ ) intensities, one measures the orbital moment of the valence shell, as schematically shown in Fig. 3.6 (c).

In the case of transition metal Fe, the absorption spectra for XMCD are usually measured at the L-edge. This corresponds to the following process in our case: a 2p electron is excited to a 3d state by an x-ray of about 700eV. Because the 3d electron states are the origin of the magnetic properties of the elements, the spectra contain information on the magnetic properties.

#### 3.3.3 Photoemission Spectroscopy (PES)

##### 3.3.3.1 Energy conservation

In 1887, Heinrich Hertz announced the discovery of the photoelectric effect, in which the electrons are emitted from matter when the incoming photon energy is bigger than the work function. This phenomenon belongs to light-matter interaction with low photon energy (a few eV to a few keV) while with mid-energy ( $\sim$ MeV) the Compton scattering is dominant and with high-energy ( $>$  MeV) the Pair production ( $e^-$  and  $e^+$ ) is obtained.

In 1905, A. Einstein presented the formula of photoemission:

$$E_{kin} = \frac{R}{N} \beta \nu - P. \quad (3.3)$$

R is the gas constant; N is the number of “real molecules”; P is the potential produced by charging when electrons leave the bulk;  $\beta$  is  $1/k_B$ , where  $k_B$  is the Boltzmann constant. Later, the Plank constant  $h$  is introduced and  $E_B$ , the binding energy of a valence electron and  $\Phi$ , the work function was introduced into the formula.

$$E_{kin} = h\nu - E_B - \phi, \quad E_{kin,max} = h\nu - \phi. \quad (3.4)$$

This is “Energy conservation”, the first conservation law in the photoemission process. The photoelectron effect must conserve the energy by transferring the energy of photons to the electrons. Based on energy conservation law, Fig.3.7 shows schematically how the energy level diagram and the energy distribution curve (EDC) of photo-emitted electrons relate to each other. In this type of experiment, the momentum information is lost by the integration

over all outgoing wave vectors. Such measurements yield a joint density of states.

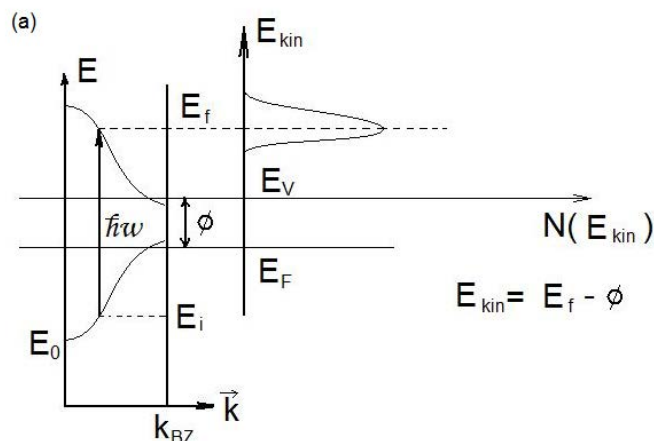


Fig.3.7 Relation between the energy levels (valence band) in a solid and the electron energy distribution produced by photons of energy  $\hbar\omega$

### 3.3.3.2 Momentum conservation

The second conservation law is related to momentum conservation. When electrons travel to the interface between the crystal and the vacuum, those with the kinetic energy sufficient to overcome the surface potential and, at the same time, having an appropriate orientation of the momentum vector  $\vec{k}$ , can escape while the other electrons are reflected totally to the bulk. (See Fig.3.8)

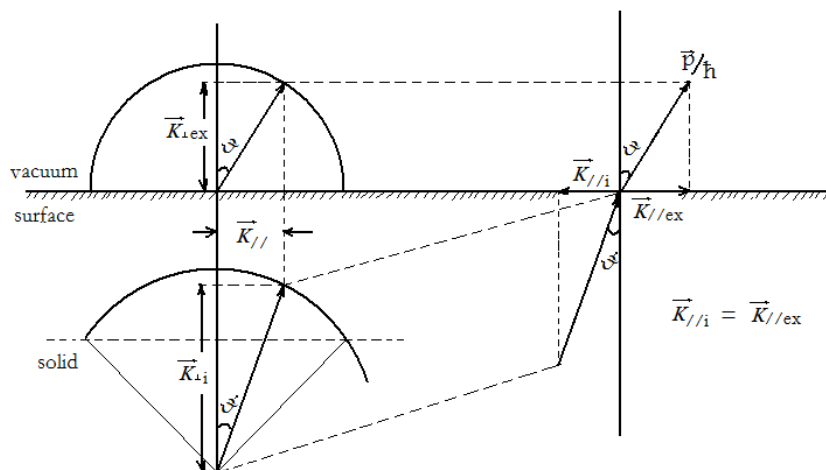


Fig.3.8 Momentum relations at the solid-vacuum interface in free electron model. It is assumed that the photoelectron has final state inside the solid, and the  $k_{||}$  is conserved.

For the electrons escaping into the vacuum must satisfy the condition:

$$\frac{\hbar^2}{2m} \underline{\hat{K}} \geq E_f - E_0 \quad (3.5)$$

where  $E_0 (< 0)$  is the energy of the bottom of free-electron-like final state band and  $K_{\perp}$  is the component of the wave vector of the excited electron normal to the surface. For the

### Chapter 3: Experimental aspects

determination of  $k_{\perp}$ , three methods have been used: either it is adjusted in such a way that the agreement between experimental and theoretical band structure of the occupied states is optimal (what we used in this thesis), one uses the value of the theoretical muffin-tin zero or one looks for symmetries in the experimental  $E(k_{\perp})$  curves.

The transmission of the electron through the surface leaves the parallel component of the wave vector conserved:

$$|\vec{K}_{//i}| = |\vec{K}_{//ex}| = |\vec{k}_{f//}| = \sqrt{\frac{2m}{\hbar^2} E_{kin}} \sin \vartheta \quad (3.6)$$

In the free electron model (then  $E_0$  is called also “inner potential”) and one electron approximation, the energy of the electron in the initial state and final state are:

$$E_i(\vec{K}) = \frac{\hbar^2 \vec{K}^2}{2m} \quad (3.7)$$

$$E_f(\vec{K}) = \frac{\hbar^2 \vec{K}^2}{2m} - |E_0| = \frac{\hbar^2 (\vec{K}_{//}^2 + \vec{K}_{\perp}^2)}{2m} - |E_0| \quad (3.8)$$

Angle-resolved photoemission spectroscopy (ARPES) is based on energy and angular momentum conservation law. It allows mapping the band structure in the momentum space. The geometry of an ARPES experiment is shown in Fig. 3.9. An electron analyser measures the number, angle and kinetic energy of electrons emitted from the solid. According to equations 3.6- 3.8, by measuring the emission angle of the electron relative to the crystal axis and the analyser, the momentum wave vector of the emitted photoelectron can be determined. Using momentum conservation, the momentum of the electron in the initial state can be known. Different emission angle corresponding different  $k_{//}$  will give the mapping of band structure. The simply relationship is based on already mentioned assumption of a free-electron final state. It is not only a convenient but also a rather accurate approximation (in certain case, the free-electron model is not appropriate for low photon energy) for determination of  $E(\mathbf{k})$  curves from measured angle-resolved EDCs.

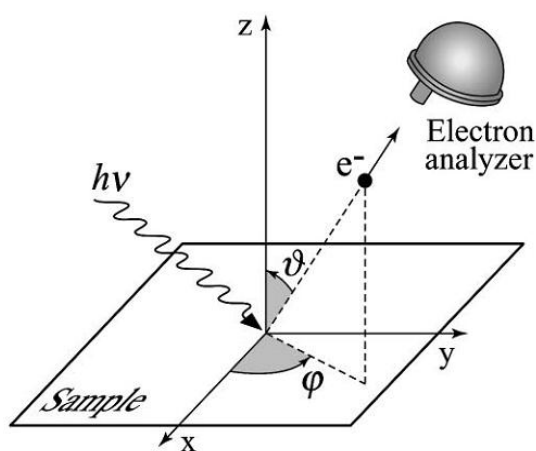


Fig.3.9 Geometry of an ARPES experiment in which the emission direction of the photoelectron is specified by the polar ( $\vartheta$ ) and azimuthal ( $\varphi$ ) angles

Chapter 3: Experimental aspects

ARPES has great potential to quantitatively compare experimental line shapes with theoretical predictions, providing insight into the nature of the single particle excitations. For example, good agreement between ARPES and theory has been demonstrated on model systems such as noble metal surface states, two-dimensional Fermi liquid, and also on systems with strong electron-phonon coupling.

In our measurements, the GammaData Scienta electron analyser (R4000) is used to collect ARPES spectra at CASSIOPEE and VUV beamlines and a SPECS analysers (Phoibos 150) are used at BaD EIPh and ADRESS beamlines. Those are hemispherical analysers fitted with a 2-dimensionnal detector having typical angular acceptance of  $\pm 15^\circ$ . (See Fig. 3.10)

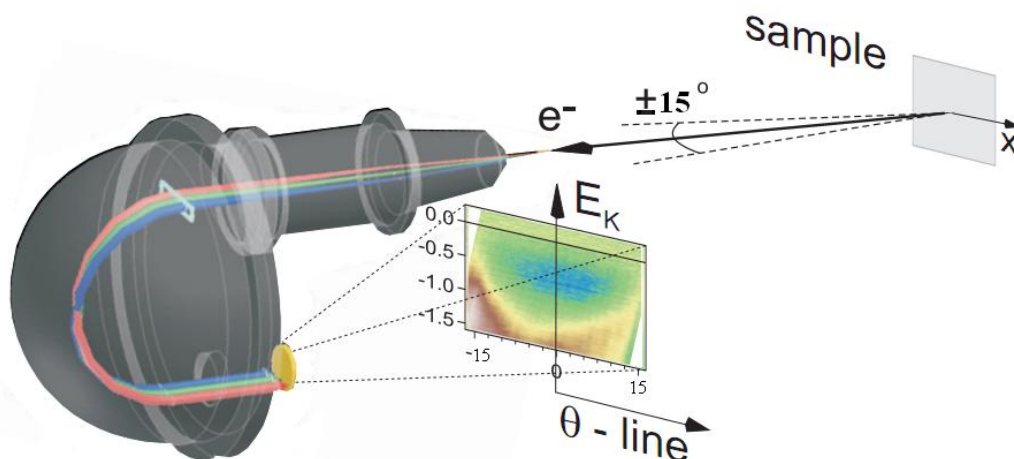


Fig.3.10 Schematic configuration of hemispherical electron analyser

The data collected with the SPECS analyser at BadElph beamline needed some preliminary treatment, which is shown in Fig.3.11. Here, the CCD camera takes the whole entrance window, while only the centre region of the window that is covered by a fluorescent powder is of interest and is resolved in angle, see Fig.3.11 (b). This region was extracted and normalized by the noise level of CCD above Fermi level.

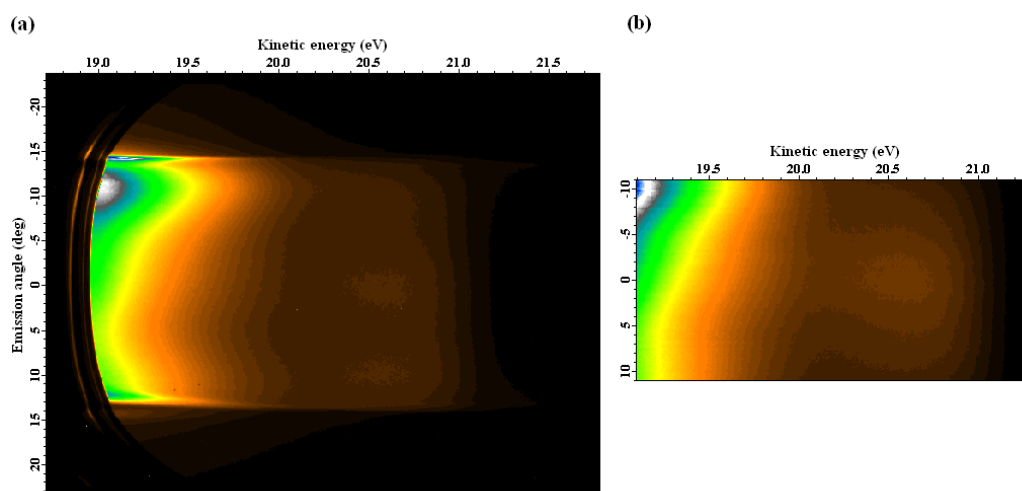


Fig.3.11 spectra obtained by Specs detector. (a) image taken directly by CCD; (b) normalized spectrum of the central region

### 3.3.3.3 Spin conservation

The third conservation law is related to spin conservation on which is based spin-resolved photoemission (SR PES). In the absence of spin-orbit coupling during the photoemission process, the spin transition from initial states to spin states is conserved. In practice, spin resolved photoemission requires that the way of the photoelectrons from the sample to the energy analyser is free of magnetic fields. Magnetic fields would lead to a precession of the electron spin around the field direction and cause a loss of the spin information. On the other hand, the sample has to be magnetized prior to photoemission in order to render it to a single magnetic domain state.

The most common method of measuring the spin polarization of electrons is Mott scattering. The original concept of Mott scattering relies on a high-energy (a few hundreds of keV) electron beam. The de Broglie wavelength is then small and one can assume classical electron trajectories. The scattering electron penetrates deep into the Coulomb field of the scattering target atom. In the rest system of the electron, the positive charge of the atomic nucleus moves towards it with a velocity  $v$ . This is equivalent to an electric current with circular magnetic field lines (see Fig. 3.12 a). The force on the magnetic moment of the electron is directed towards an increasing field when the moment is parallel to the field, but toward a decreasing field when it is antiparallel. As a consequence, the magnetic moment of the electron experiences a force to the left side when it is aligned upward no matter on which side of the atom is passes. In contrast, electrons with magnetic moment “down” are preferentially scattered to the right (Fig.3.12 (a)).

In other words, because of the interaction of the electron spin with its orbital moment during the scattering process,  $V_{so} = \frac{1}{2m^2c^2} \frac{1}{r} \frac{dV}{dr} \vec{s} \cdot \vec{l}$ , there is a difference between the effective cross sections for electrons with opposite spins.

So, if an electron beam has a polarization  $P$ , there will be a difference in counting of electrons between left (NL) and right (NR) side relative to the direction of the beam. This is valid in the plane containing the electron beam that is perpendicular to the electron spin. From the difference of counting rates, a normalized parameter, asymmetry  $A_x$ , can be defined yielding the spin polarization  $P$  of electrons:

$$A_x = \frac{(N_L^- - N_R^-)}{(N_L^+ + N_R^+)}, \quad P_x = \frac{A_x}{S_{eff}} \quad (3.10)$$

With the absolute statistical error:  $\Delta A = \frac{1}{\sqrt{N_L + N_R}}$  and  $\Delta P = \frac{1}{S_{eff} \times \sqrt{N_L + N_R}}$ . We note that for the calculation of polarization, it is necessary to count the electrons only in two channels, while four detectors are used in most cases to cover two polarization components.

$S_{eff}$  is the Sherman function.  $S_{eff} = 1$  is the case of a 100% polarized beam. Usually, the value of  $S_{eff}$  is around 0.1~0.2. It is very difficult to determine the absolute value of  $S_{eff}$  because an electron source of known polarization is needed to do calibration as a baseline.

From the measured spin polarization, spin-up ( $I^\uparrow(E_B)$ ) and spin-down ( $I^\downarrow(E_B)$ ) spectra can be obtained:

$$\begin{aligned}
 I^{\uparrow}(E_B) &= \frac{1}{2} I_0(E_B)(1 + P(E_B)) \\
 I^{\downarrow}(E_B) &= \frac{1}{2} I_0(E_B)(1 - P(E_B))
 \end{aligned}
 \tag{3.11}$$

where  $I_0(E_B)$  is the spin integrated spectrum.

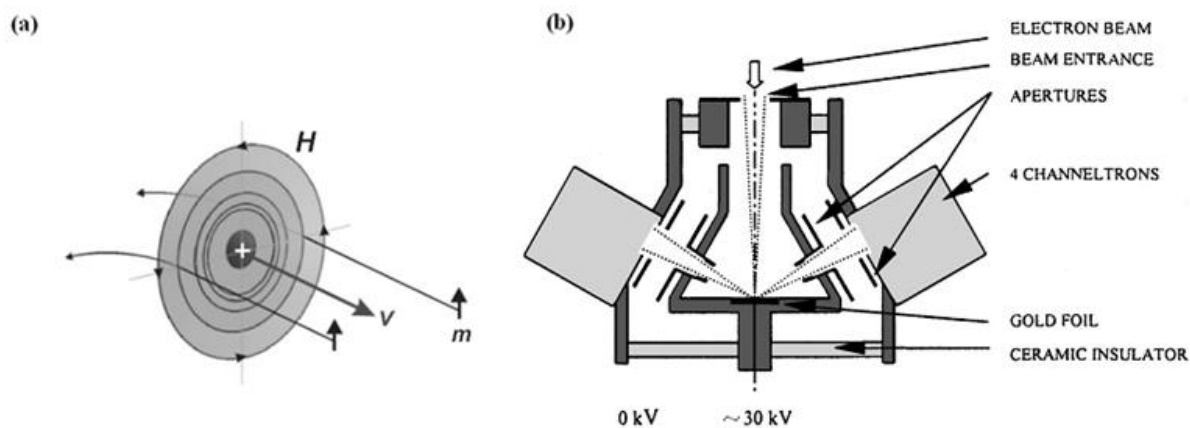


Fig.3.12 (a) Schematic configuration of retarding-potential Mott detector ; (b) Illustration how spin-orbit coupling in elastic Coulomb scattering can spatially separate the two spin states.  $m$  is a magnetic dipole and  $H$  is an inhomogeneous static magnetic field.

In practice, this kind of scattering is used in Mott detectors. We used a retarding-potential detector, so called “mini Mott detector” that needs only 20 – 30 keV of acceleration for the electron beam. It is schematically shown in Fig. 3.12 (b). The scattered electrons are recorded with two pairs of detectors arranged in two perpendicular scattering planes that allow measurement of two components of the polarization vector. In each plane the detectors are placed at an angle of  $120^\circ$  on left and right sides of the beam. At this angle, the Sherman function has a broad maximum for Au foil, which is a mostly used target for scattering because of its high atomic number and chemical stability.

Because during the photoemission process the photon of the exciting light does not directly couple to the electron spin, one might expect that the spin polarization measured in a spin-resolved photoemission experiment should directly reflect the spin polarization of the initial states under study. However, indirect coupling occurs in the process due to several mechanisms involving a spin-dependent reaction of the remaining  $(N-1)$  electron system (if it is strongly spin polarized), spin-orbit effects and spin-dependent elastic exchange scattering (spin-polarized photoelectron diffraction) in the photoelectron final state, or finally spin-dependent inelastic scattering processes during electron transport to the surface. Especially in strong correlation systems, the SRPES may not reflect the true spin polarization. One must consider the interaction of the excited electrons with other excitations, e.g. polarons. These will be discussed in chapter 5.

### 3.3.3.4 Time of flight spectrometer (TOF)

The laser stimulated photoelectron spectra were measured by a TOF analyser. The advantage of this analyser comparing with normal hemisphere analyser is that it's more efficient, because the electrons with different kinetic energy are collected at the same time while the hemisphere analyser must sweep the energy which losses huge amount of electrons.

In a TOF analyser, the kinetic energy of electrons is measured through the flying time of electrons from sample surface to detectors (distance  $L$ ). (See Fig.3.1)

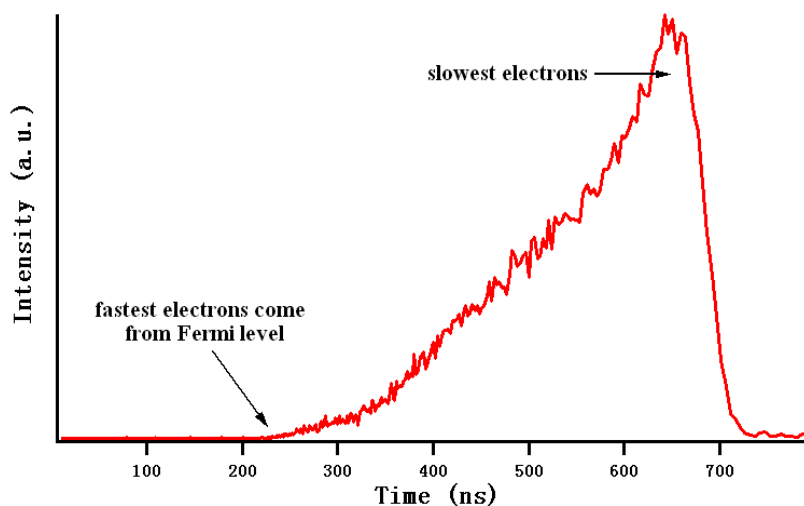


Fig.3.13 Raw Intensity curve obtained by TOF spectrometer in the function of measured time

Fig.3.13 shows the raw spectrum measured by TOF analyser. The calibration of TOF can be divided into two main parts. The calibration of flying time can be preceded by comparing the direct time ( $t_{\text{raw}}$ ) value recorded by electronics, with the event start time ( $t_0$ ). We can simply regard the measured time  $t_{\text{mea}} = t_{\text{raw}} - t_0$ . The time-to-energy calibration is done in the following way: The polarization voltage on the sample is changed by an interval of  $\Delta V$ , in our case, 200meV, then the measured  $I(t)$  curve will undergo a shift in time  $\Delta t$  due to the accelerating effect of the polarization voltage. (See Fig.3.14) Take the same position for each curve as a reference, they represent the electrons with the energy difference ( $n \cdot e\Delta V$ ,  $n$  is the number of interval). Ideally, the relationship between kinetic energy and flying time is:

$$E_{k i n} = \frac{1}{2} m_e \left( \frac{L}{t_{m e d}} \right)^2 \quad (3.12)$$

Although the calibration of time-to-energy can be much more complicated (See in reference [83]), in a very simply approximation, we use a hyperbola-like curve (from eq.3.12) to simulate the relationship between  $t_{\text{mea}}$  and kinetic energy. (See Fig.3.15)

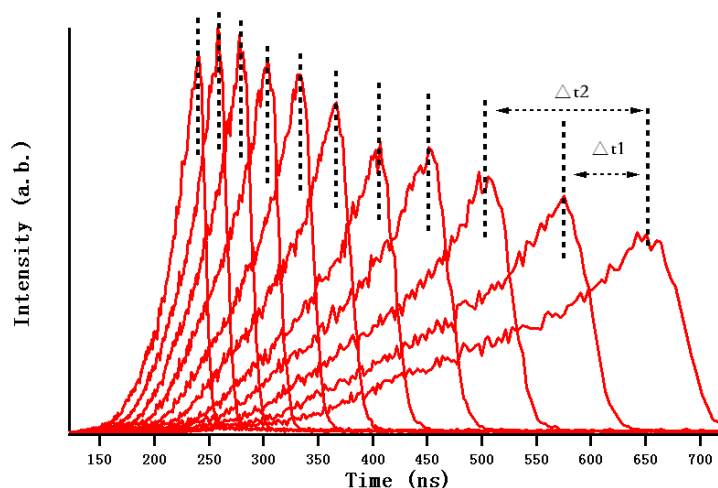


Fig.3.14 Calibration of time to energy for TOF spectrometer. The slowest electron comes from the same band in the solid, the difference of arriving time  $\Delta t$  is due the sample voltage

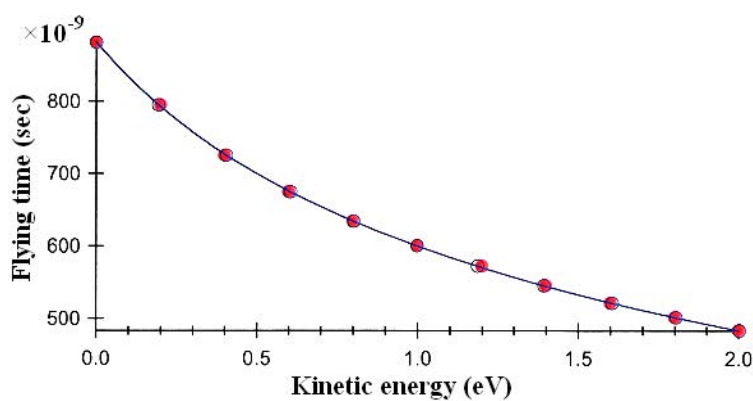


Fig.3.15 The relationship between flying time  $\Delta T$  and kinetic energy of the photoelectrons is simulated and shown

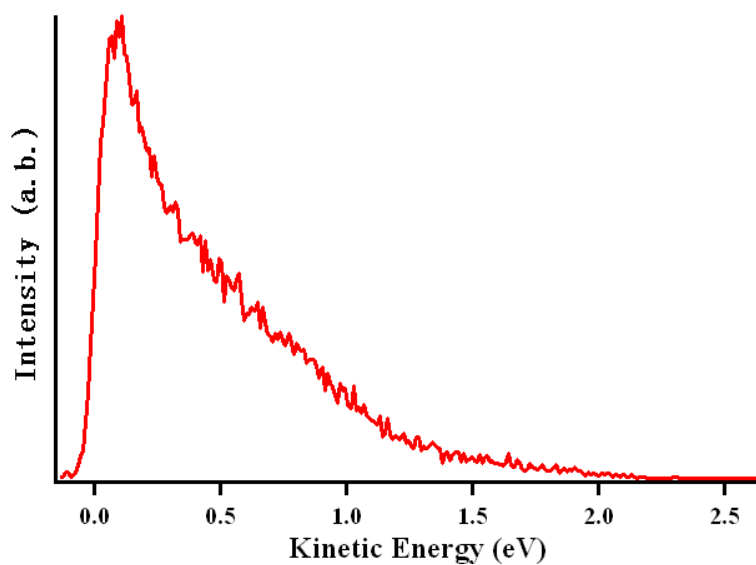


Fig.3.16 Energy dispersion curve of photoelectrons, obtained from Fig.3.13 by using the calibration curve in Fig.3.15 to transfer flying time to kinetic energy

### Chapter 3: Experimental aspects

Many effects can affect the energy and distribution of TOF spectra; among the most important are the space charge field and the residual electric and magnetic fields. The space charge field is due to the mutual interaction of electrons in the flying bunch from the sample to the detector. (See Fig.3.17) When a large number of electrons are generated from a short pulsed source and leave the sample surface, the electrons will first experience a rapid spatial distribution depending on their kinetic energy. Then, because of the Coulomb interaction, the fast electrons tend to be pushed by the electrons behind them while the slow electrons tend to be retarded by those fast electrons. This energy redistribution will distort the intrinsic information contained in the initial photoelectrons by giving rise to two kinds of effects. One is a general broadening of the energy distribution, due to both acceleration and retardation of electrons in their encounters. The other is a systematic shift in energy. Actually, there is until now no effective way to avoid space charge effects but only method to reduce the influence of it.

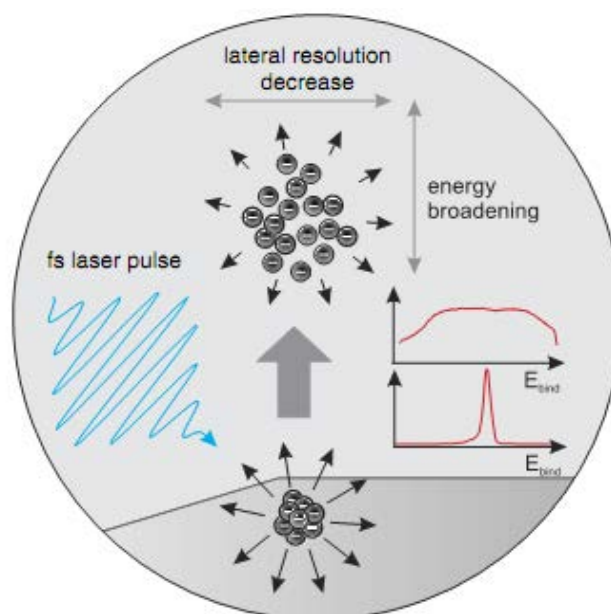


Fig.3.17 Illustration of space charge effects and their impact on PES measurements. The Coulomb repulsion of the photoelectron cloud leads to a broadening of the kinetic energy distribution of the photoelectrons and consequently results in image blur [84]

# Chapter 4:

---



---

## Simulation methods:

---



---

### 4.1 Electronic structure calculation

Taking into account spin-dependence of the DFT, one can study magnetic properties of complex materials. In particular, HMF was introduced based on this kind of calculation by de Groot et al [4]. This method is formally exact, but for practical calculations, the exchange-correlation energy as a functional of the density must be approximated.

$$E[n] = T_s[n] + \int d^3r v_{ext}(\vec{r})n(\vec{r}) + V_H[n] + E_{XC}[n] \quad (4.1)$$

$E[n]$  is the total energy of a system, expressed as a functional of the charge density  $n$ ;  $T_s$  is the Kohn-Sham kinetic energy;  $v_{ext}$  is the external potential acting on the interacting system;  $V_H$  is the Coulomb energy;  $E_{XC}$  is exchange-correlation energy which is most concerned.

The simple description of correlation is that the motion of each particle in the system depends on the motion of other particles. In practice, DFT uses two standard approximations: the local-(spin)-density approximation (LDA) and generalized gradient approximations (GGA). In this theory (DFT+GGA or DFT+LDA), only the exchange correlation energy as a functional of the electron spin densities  $n_\uparrow(\mathbf{r})$  and  $n_\downarrow(\mathbf{r})$  must be approximated:

$$E_{XC}^{LDA}[n_\uparrow, n_\downarrow] = \int d^3r n(\vec{r}) \epsilon_{XC}^{homo}(n_\uparrow, n_\downarrow) \quad (4.2)$$

$$E_{XC}^{GGA}[n_\uparrow, n_\downarrow] = \int d^3r f(n_\uparrow, n_\downarrow, \nabla n_\uparrow, \nabla n_\downarrow) \quad (4.3)$$

where  $n(\mathbf{r}) = n_\uparrow(\mathbf{r}) + n_\downarrow(\mathbf{r})$ .  $\epsilon_{XC}$  is the exchange correlation energy per particle of the homogeneous electron gas with a given density.  $f$  is a function of density and scale gradient which has enhancement factor over LDA exchange. GGA sometimes corrects, sometimes overcorrects LDA prediction by tending to improve the total energies, atomization energies, energy barriers and structural energy differences [85]. Typically, GGA favors density inhomogeneity more than LDA does [86]. We can note the difference of total energy between GGA and LDA depending on the exchange-correlation energy:

$$E_{tot}^{GGA}[n^{GGA}] = E_{tot}^{LDA}[n^{LDA}] + \underline{\underline{E_{xc}^{GGA}[n^{LDA}] - E_{xc}^{LDA}[n^{LDA}]}} + o(n^{GGA} - n^{LDA})^2 \quad (4.4)$$

A first principal numerical GGA can be constructed by starting from the second-order density gradient expansion for the exchange-correlation hole surrounding the electron in a system of slowly varying density, then cutting off its spurious long-range parts to satisfy sum rules on the exact hole [48].

Despite the many successes of LDA and GGA, they are claimed to be useless for strongly correlated materials (e.g. transition metal oxides, which contain atoms with open  $d$  or

Chapter 4: Simulation methods

$f$  shells) [31][36][87]. The magnitude of the self-interaction (electron interacts with its own mean field) in LDA and GGA depends very much on the nature of the hybridization of electron orbitals in the oxide. Then the GGA+U (LDA+U) method was introduced as a modification that adds an intra-atomic Hubbard  $U$  repulsion term in the energy functional. Consideration of Hubbard repulsion energy is particular important for materials such as transition metal oxides that have narrow  $d$ -bands where, when the electron concentration is not very high and hence screening is ineffective, the correlation between electron motion is much more pronounced than is predicted within the conventional band picture. [96]

Treated in a self-consistent mean-field manner (Hartree-Fock), the GGA+U (LDA+U) provide a greatly improved description of strongly correlated materials.

$$E^{GGA+U} = E^{GGA} + E^U \quad (4.5)$$

It is very important to understand the correcting energy part  $E^U$  (Hubbard  $U$  interaction term). The addition of a Hubbard  $U$  interaction also introduces the need for “double counting” correction terms in the energy functional to account for the fact that the Coulomb energy is already included in the GGA (LDA) functional.

$$E^U = E^{ee} - E^{dc} \quad (4.6)$$

$E^{dc}$  is the double counting energy correction, which is the electron-electron interaction for the localized states, which depends only on the total number of localized electrons in the orbital states. More important is the  $E^{ee}$  part:

$$\begin{aligned} E^{ee} &= E^H(n) + E^X(n) \\ E^H(n) &= \frac{1}{2}U(\sum n)^2 + E_{aniso}^H \end{aligned} \quad (4.7)$$

Where  $E^H(n)$  is the Hartree energy part (atomic unit energy) and  $E^X(n)$  is the exchange energy part. The first term in the Hartree energy is the isotropic interaction. This is the relatively simply Coulomb repulsion. And the second term is the anisotropic interaction which is only  $J$  dependent. It's worth noting that the anisotropic interaction is zero for electrons of spherical shell [92].

The exchange interaction part can be written as:

$$E^X = -\frac{1}{2}J\sum_s N_s^2 - \frac{U-J}{2}\sum_s Tr(n^s)^2 - E_{aniso}^X \quad (4.8)$$

Similar as said above, the first term in the equation is the isotropic exchange interaction, the second term is the self-interaction correction and the third term is the anisotropic exchange interaction [92].

The realization of the GGA+U (LDA+U) method depends strongly on the accurate determination of matrix elements  $U$  and  $J$  of the Coulomb and exchange interactions.  $U$  and  $J$  can be obtained by differentiating the LSDA energy with respect to the variation in the electron-density matrix and to the variation in the magnetization, respectively [93]. Such estimation of  $U$  and  $J$  are based on the assumption that the GGA (LDA) energy is a continuous function of both the electron density and the magnetization. [94]

## 4.2 Effect of U-parameter

The band structure calculation results of  $\text{Fe}_3\text{O}_4$  used in this thesis are based on WIEN2k package, orbital dependent potentials included GGA+U method, which is very useful for strongly correlated systems. (Detailed information can be found on the website: <http://www.wien2k.at/>) The calculation was done by Peter BLAHA from TU Wien, Austria. Before presenting the simulation methods, the effect of parameter U is briefly mentioned.

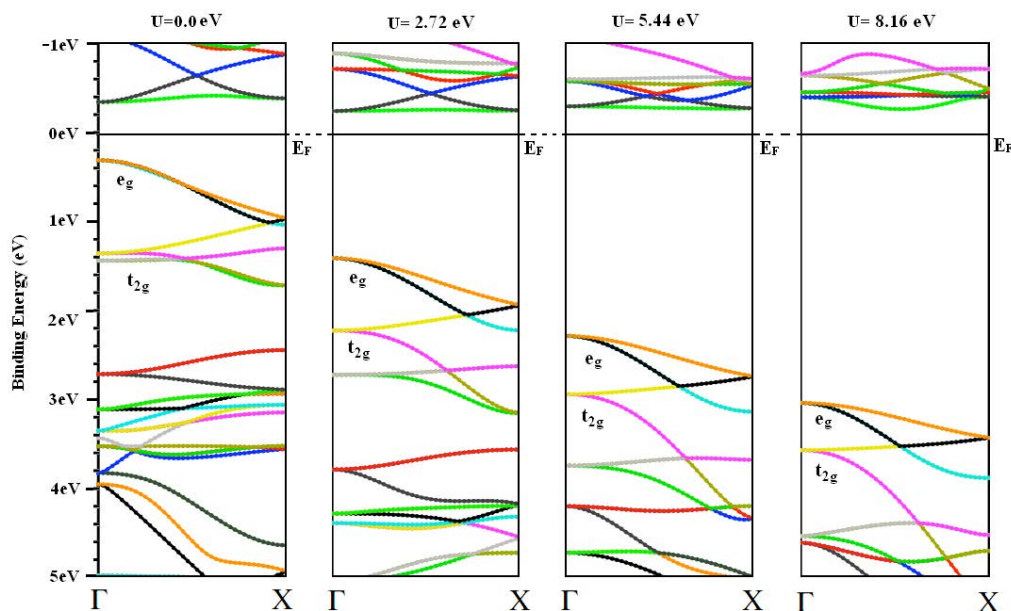


Fig.4.1 Effect of the parameter U in the GGA+U band-structure calculations for majority band along the  $\Gamma \rightarrow X$  direction.

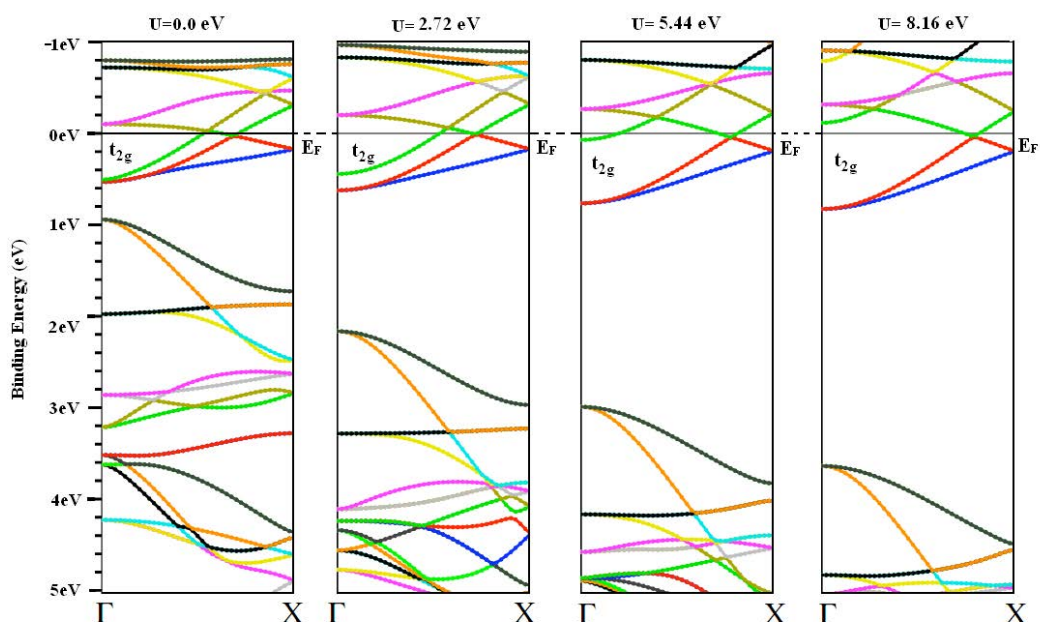


Fig.4.2 Effect of the parameter U in the GGA+U band-structure calculations for minority band along the  $\Gamma \rightarrow X$  direction.

Chapter 4: Simulation methods

As the parameter  $U$  increases, majority bands are shifted towards higher binding energies, while the minority  $t_{2g}$  bands are separated (green and red) during the increase of  $U$ .  $U$  is an empirical parameter and is to be adjusted to experimental data. It cannot be directly related to electron correlations like the Hubbard's  $U$ . For our experimental data we estimated the  $U$  value to be 2.72 eV. The complete set of calculated results is shown in Fig 4.3.

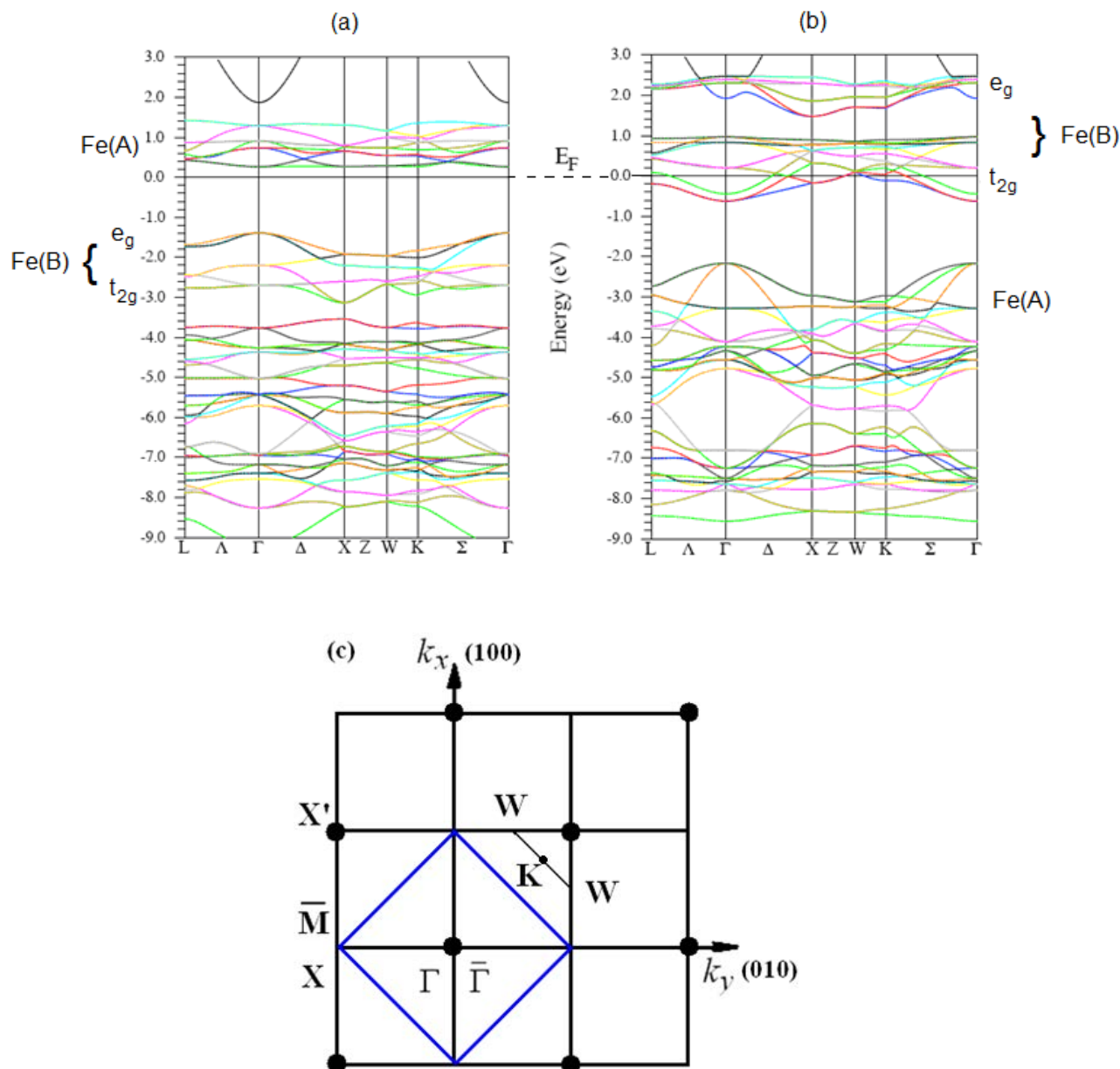


Fig.4.3 Electron band structure calculation with Hubbard  $U=0.2$  Ry. (a) majority and (b) minority spin band structure; (c) Schematic diagram of BZ for the  $\Gamma XWK$  mirror emission plane, the blue square represents the  $(1 \times 1)$  unit cell on (001) surface

### 4.3 Parameters used in simulation

The simulation of our spectra is based on GGA+ $U$  calculations in which we included three different major interactions appearing in the photoemission process: photoelectron

lifetime broadening; electron-polaron interaction and  $k_{\perp}$  broadening.

The influence of the photohole lifetime on the measured line shape has been judged based on a direct-transitions treatment of the photoemission, which describes the inelastic scattering by an energy uncertainty of the final Bloch state. The finite lifetime without inelastic scattering gives  $E_f(\mathbf{k})$  an energy width  $\delta E$  which is not constant due to the same scatter process of photohole. (See Fig.4.4 (a) and (b)) The direct method of investigating photohole lifetimes in valence-band photoemission consists in determining the full width at half maximum (FWHM) in ARPES spectra. The relation between lifetimes and peak intensities in experimental spectra is somewhat complex, because optical absorption and electron scattering will also contribute to the intensities. In the simplest way of a one-step formulation of photoemission, scattering only appears in the self-energies of the photohole and photoelectron. Inelastic scattering is assumed to depend weakly on energy. From simple phase space arguments, the lifetime of photohole becomes infinite as the hole approaches Fermi level because close to Fermi energy, quasi-particles have less and less phase space to scatter so that the lifetime diverges. The theoretical treatments of intrinsic lifetime broadening were available in 1981 in a model developed by P. Thiry in his thesis [91]. The expression for the measured line-width is considered to be a linear combination of the photoelectron and photohole lifetimes simulated with Lorentzian line shapes and a first order approximation within one-electron band structure.

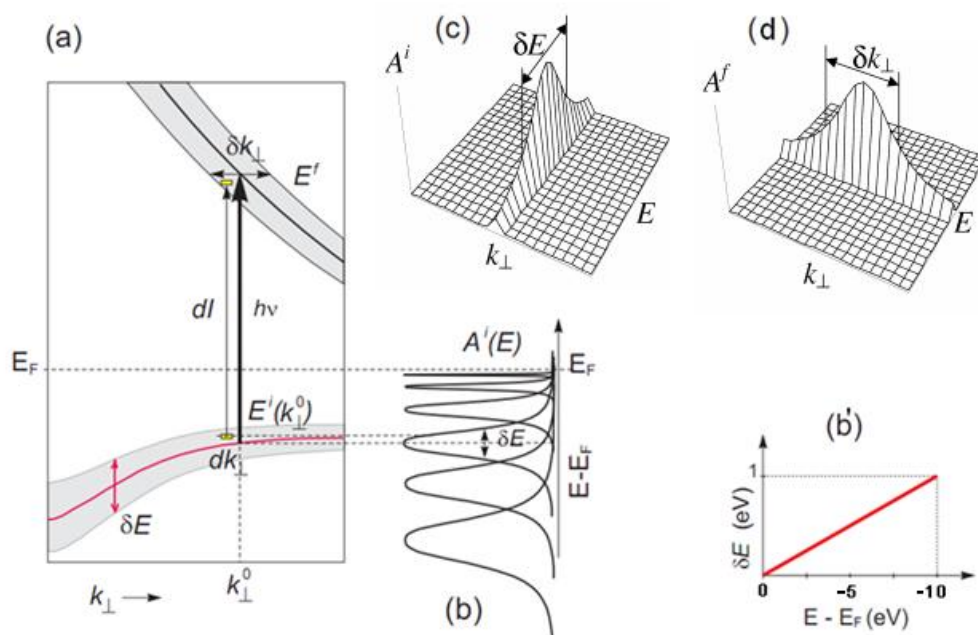


Fig 4.4 (a) Schematic diagram of how the photocurrents for a given direct transition  $k_{\perp}^0$  (thick vertical arrow) the initial state spectral function  $A^i(E)$  are weighted over the final state  $A^f(k_{\perp})$  broadening interval  $\delta k_{\perp}$ . (b) the energy broadening  $\delta E$  due to photohole lifetime effect is simulated as a Lorentzian distribution. The broadening effect is not constant but depends on binding energy (b'); (c) initial state  $A^i(E)$  broadening due to electron-phonon interaction is simulated as a Gaussian distribution; (d) the final state  $k_{\perp}$  broadening due to uncertainty of momentum is simulated as a Lorentzian distribution.

[88][89][90]

Mathematically, this is expressed via the Lorentzian convolution with FWHM of  $\delta E$ , centered

Chapter 4: Simulation methods

around the direct transition. See Fig.4.4 (b)

In the picture of strong electron-phonon coupling, electron excitation is heavily dressed by virtual phonons which leads to the formation of polaronic quasi-particles (polarons). Removal of an electron from the coupled system results in a spectrum consisting of a coherent quasi-particle peak, greatly reduced in spectral weight and renormalized in energy. (See Fig. 4.5)[10]. In Alexandrov and Ranninger model [95], the electron removal spectrum of a system with strong electron phonon coupling can be written as:

$$I(E_B) \propto e^{-g^2} \bar{N}_P(E_B) + \sum_{n=1}^{\infty} e^{-g^2} \frac{g^{2n}}{n!} \bar{N}_P(E_B - n\omega_0) \quad (4.9)$$

Where  $E_B$  is binding energy,  $g^2 = \varepsilon_p/\omega_0$ ,  $\varepsilon_p$  is polaronic binding energy and  $\omega_0$  is characteristic phonon energy,  $\bar{N}_P(E_B)$  is polaronic density of states.

The first term describes the polaronic quasi-particle band renormalized by a factor  $e^{-g^2}$ , where  $g^2$  is a dimensionless electron-phonon coupling strength given by polaronic binding energy divided by characteristic phonon energy. The second term describes the angle-independent line shape due to the phonon-assisted photoemission. The spectral weight of this zero-phonon line is reduced exponentially quickly as a function of  $g^2$ . Since the functional form of eq.4.9 is a Poisson distribution, this reduces to a simple Gaussian in the limit of large  $g^2$ . In our simulation, we will use the Gaussian form to substitute for the Poisson distribution.

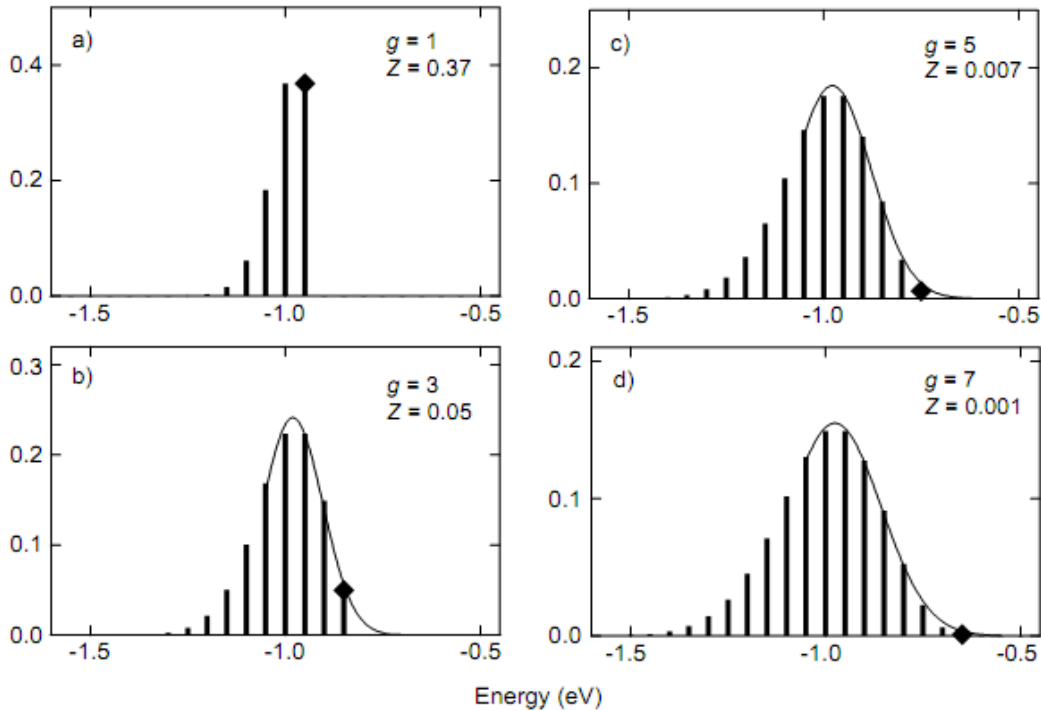


Fig.4.5 Calculation from the interacting electron-phonon Hamiltonian; (a)-(d) show the evolution of  $A(E_B)$  as a function of electron-phonon coupling strength: the quasi-particle peak is shifted to lower binding energies and the spectral weight is reduced exponentially quickly as a function of  $g$ . [10]

As known, a fundamental difficulty in the interpretation of ARPES data on

## Chapter 4: Simulation methods

three-dimensional systems is the intrinsic broadening of the electron momentum component perpendicular to the crystal surface  $k_{\perp}$ . Wadati et al [97] explain that the PE signal from the  $e_g$  and  $t_{2g}$  bands of transition metal oxides are smeared due to intrinsic uncertainty in momentum of the electrons in the solid perpendicular to the crystal surface caused by small escape depth of photoelectrons. This uncertainty has its origin in the inelastic absorption of the PE final states damped towards the interior of the solid. From the viewpoint of the PE final states, the initial states are localized close to the surface, hence their momentum, according to Heisenberg's uncertainty principle must have some momentum broadening. (See Fig.4.4 (d) ) Fig.4.6 shows the evolution of PE spectra with  $k_{\perp}^0$  scanning along  $\Gamma X$  (upper panels) and positions of the spectral peaks mapped on top of the true valence band (lower panels).

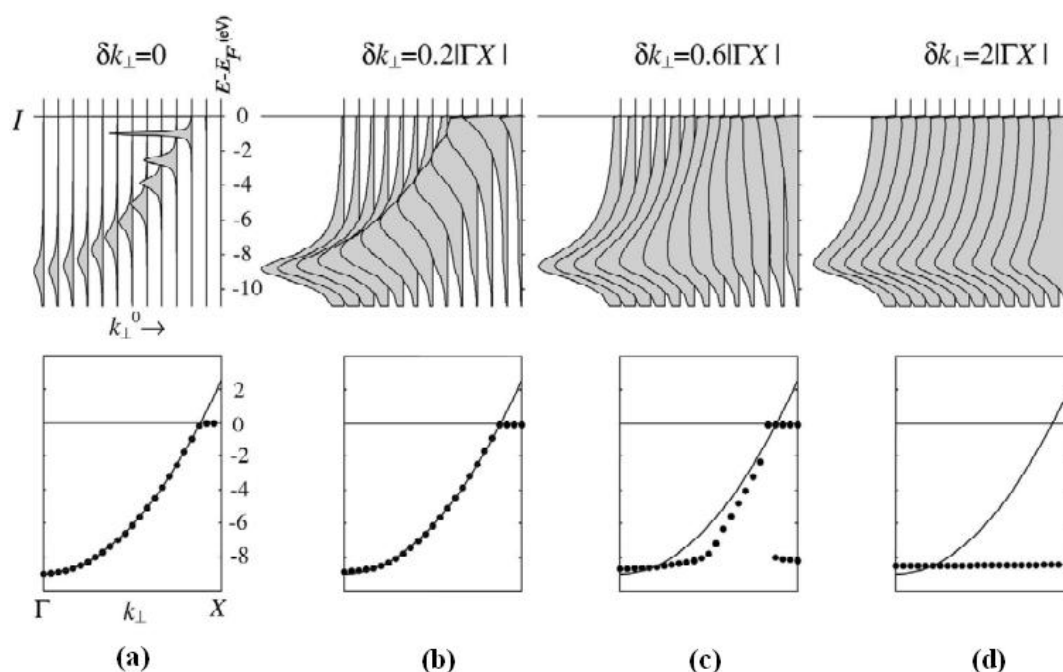


Fig.4.6 Simulated PE experiments on a model 3D band, performed with different strength of damping in  $k_{\perp}$  broadening. The corresponding  $\delta k_{\perp}$  values correspond to ideal  $k_{\perp}$  resolution (a), representative for the band-structure regime in a real PE experiment (b), degraded  $k_{\perp}$  resolution (c) and DOS regime (d); the lower panels show the positions of the spectral peaks mapped on top of the true valence band [88].

Because at present the calculation of the photoemission process is hardly feasible for  $\text{Fe}_3\text{O}_4$ , we did our simulation of the spectra using a simple model. We used the free-electron approximation for the final states, completely ignoring the matrix elements. In the simulation the ground state data were convoluted by Lorentzian and Gaussian functions to account for the lifetime and electron-phonon coupling effects, respectively. A reasonable description of the initial- state lifetime broadening was found using a Lorentzian with a full width at half maximum ( $\text{FWHM}_L$ ) varying linearly from 0 at EF to 1 eV at a BE of 10 eV, which covers the whole width of the VB (Fig 4.4 (b')). The contribution of small polarons was incorporated by convoluting the simulated spectra with a Gaussian having a  $\text{FWHM}_G$  of 600 meV. The 50meV  $\text{FWHM}_G$  experimental broadening, due to the electron analyzer and the photon bandwidth, is negligible compared to that due to polarons.

Chapter 4: Simulation methods

We did also several tests including  $k_{\perp}$  broadening. However, in our photon energy range, the inelastic mean-free path predicted from the “universal curve” is in the order of  $\sim 1\text{nm}$ , which imposes  $\Delta k_{\perp}$  to be  $\sim 10\%$  of the BZ. This will not have a strong influence on the dispersion of bands, see Fig.4.6 (d). So, this part of broadening was neglected in the majority of our simulations.

Fig. 4.7 summarizes different steps of our simulation using the parameters introduced above. Fig. 4.8 is the simulated spin polarization spectrum in  $\Gamma X$  direction. It is done by eq.4.10:

$$P_S(E_B) = \frac{(I_S^{\uparrow} - I_S^{\downarrow})}{(I_S^{\uparrow} + I_S^{\downarrow})} \quad (4.10)$$

$P_S(E_B)$  is the simulated polarization spectrum,  $I_S^{\uparrow}$  and  $I_S^{\downarrow}$  are simulated spin up and spin down spectrum respectively. The result shows that the lifetime broadening effect will generate some spin up states near the Fermi level which reduces slightly the spin polarization (Fig. 4.8(a)). When the electron-phonon interaction was considered in the simulation, we can see a clear decrease of spin polarization close to Fermi level (Fig. 4.8(b)). More detail analysis will be discussed in chapter 5.

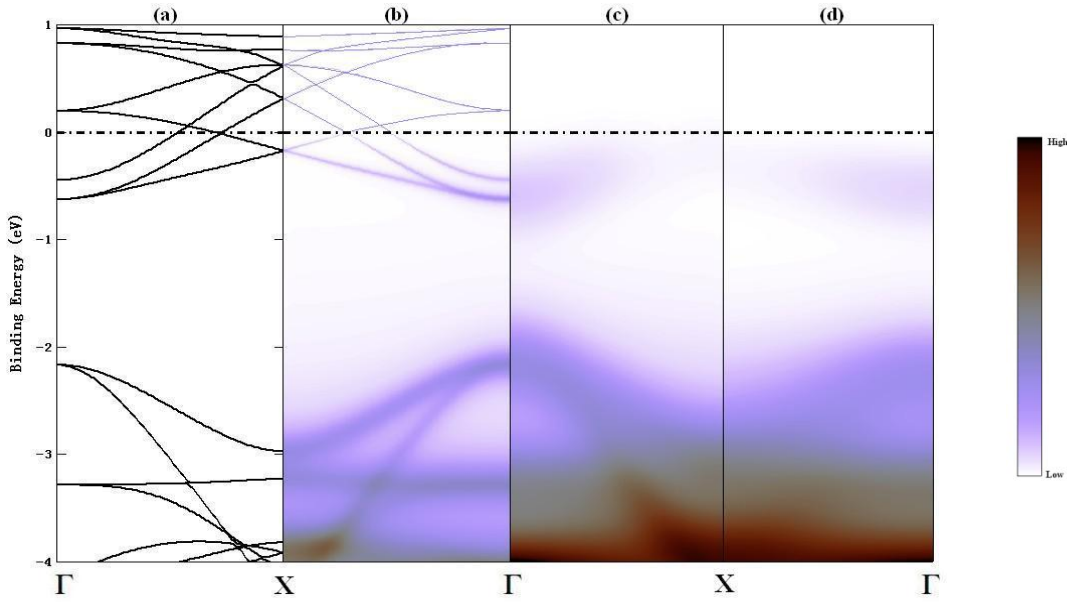


Fig.4.7 (a) GGA+U band structure (minority spin) in  $\Gamma X$  plane.

Simulation including (b) the initial state lifetime broadening plus (c) polaron contribution ( $\text{FWHM}_{\text{G}} = 600 \text{ meV}$ ) and (d)  $k_{\perp}$  broadening ( $\delta k = 10\%$  of BZ)

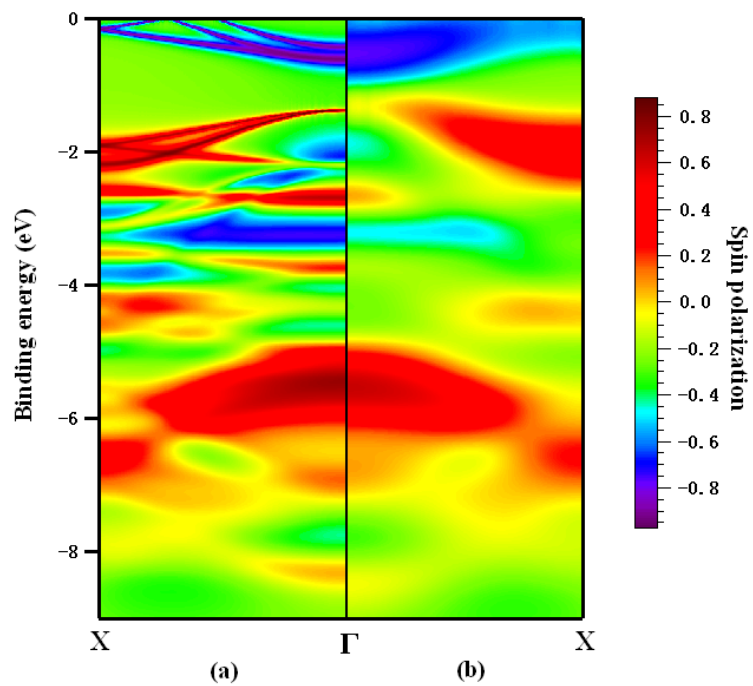


Fig.4.8 Simulation of spin-polarization in  $\Gamma X$  plane, (no  $k_{\perp}$  broadening is included); (a) only lifetime broadening is included; (b) lifetime broadening and polaron contribution are both included.

## Chapter 5:

---



---

# Results and Discussion

---



---

## 5.1 Sample preparation and characterization

### 5.1.1 Sample preparation

In this thesis, we present results obtained on four samples prepared at different synchrotron radiation centres.

We deposited epitaxial  $\text{Fe}_3\text{O}_4(100)$  thin film on  $\text{MgO}(100)$ . Prior to the deposition the  $\text{MgO}(100)$  substrate was annealed at 600 °C during 3 hours in the partial pressure of oxygen of  $5.10^{-6}$  mbar. Then, high purity Fe was evaporated from a Knudsen cell with a deposition rate of around 1.3 Å /min; the oxygen pressure was the same as for the substrate annealing. During the evaporation the substrate was maintained at a moderate temperature, of about 300°C, in order to prevent magnesium diffusion. Table 5.1 shows the list of samples and the photon energy range used for measurements.

N° of samples	Beamline	Thickness	Photon energy
#1	BaD EIPh	~40nm	21 eV
#2	CASSIOPEE	~40nm	100-200 eV
#3	ADRESS	<20nm	400 eV
#4	VUV	<20nm	133 eV

Table 5.1

### 5.1.2 Characterization of samples

After preparation, the samples were characterized *in-situ* by LEED, core-level photoemission spectroscopy, XAS and by XMCD. For sample #1, XAS and XMCD measurement were made ex-situ, at the Bach beamline, Elettra.

The  $\text{Fe}_3\text{O}_4(100)$  ( $1 \times 1$ ) surface is unstable because of a high surface energy and, as mentioned in the second chapter, its atomic arrangement is re-organized to form the  $(\sqrt{2} \times \sqrt{2})R45^\circ$  reconstruction. In Fig. 5.1 a typical LEED pattern, measured on sample #1, is shown. It was possible to do the diffraction at a very low electron energy (down to 17 eV) proving of a very high crystal quality. The observed patterns correspond well to those published in literature.

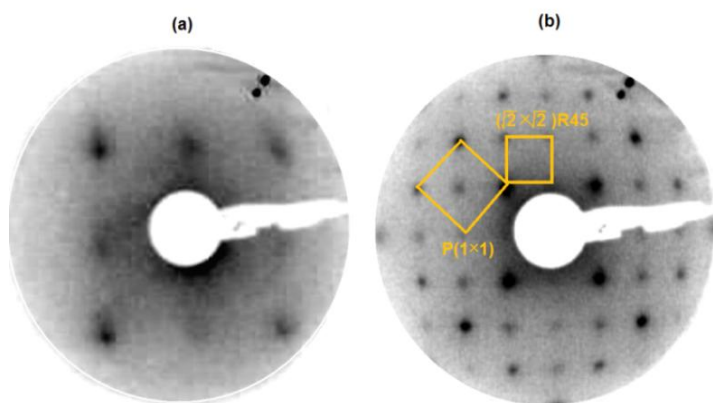


Fig.5.1 LEED patterns of  $\text{Fe}_3\text{O}_4$  sample #1 with electron energy of (a) 17 eV and (b) 69 eV.

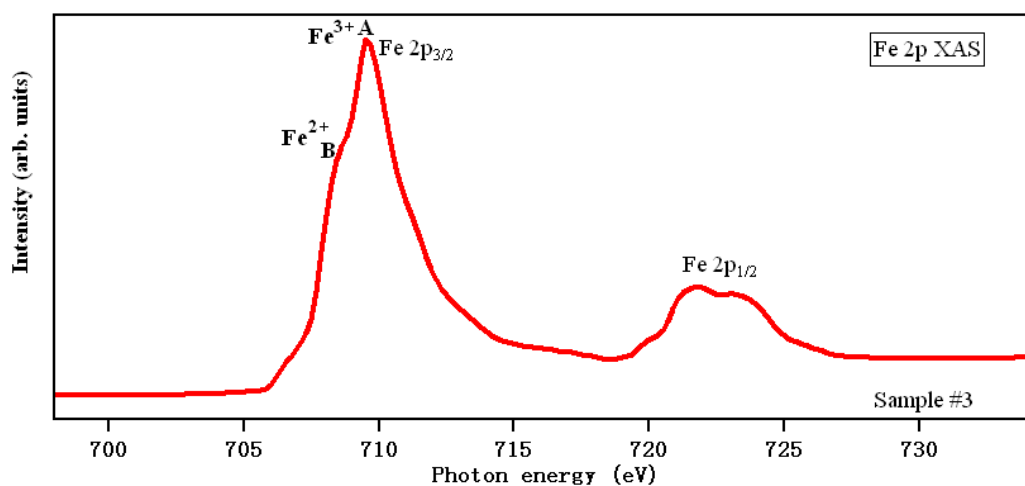


Fig.5.2 Fe 2p XAS spectrum of sample #3

Fig.5.2 shows a typical XAS spectrum, here taken on sample #3.  $L_3$  absorption peak consists of two sub-peaks, A and B corresponding to  $\text{Fe}^{2+}$  and  $\text{Fe}^{3+}$  ions, respectively. The energy difference between A and B is 1.2 eV and the peak intensity ratio of A/B is 1.4. Those results indicate a good stoichiometry of  $\text{Fe}_3\text{O}_4$ . [107] [108]

The XMCD spectrum (sample #1, Fig. 5.3) exhibits a peak at the leading edge of Fe  $L_3$  absorption, marked as 1, with a sign opposite to that of the main  $L_3$  absorption peak, marked as 2. From literature it is known that the peak 1 and peak 3 at higher photon energy originate mainly from the B-site Fe ions while peak 2 from the A-site  $\text{Fe}^{3+}$  ions. The absorption peak of the  $\text{Fe}^{2+}$  ions occurs at photon energy lower than that of the  $\text{Fe}^{3+}$  ions by 1–2 eV toward the low-energy side. Therefore the leading edge of the  $L_3$  XMCD with a negative peak results mainly from the  $2p \rightarrow 3d$  transition in B-site  $\text{Fe}^{2+}$  ions. In addition, peak 3 is derived predominately from B-site  $\text{Fe}^{3+}$  ions, consistent with the fact that the magnetic moments of the A-site and B-site Fe atoms are in antiparallel alignment.

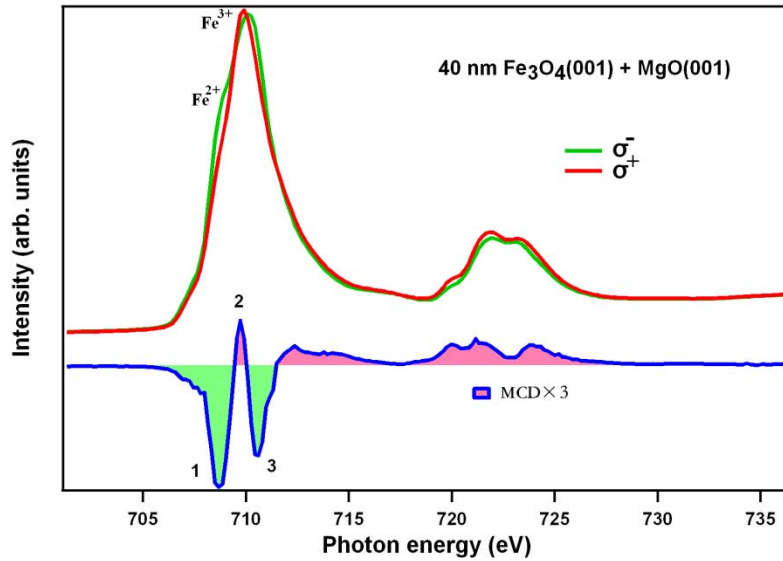


Fig.5.3 XMCD spectrum of sample #1

Another characteristic of a good quality of our Fe<sub>3</sub>O<sub>4</sub> samples is the observation of the Verwey transition. Photoemission measurements at low temperature were performed to observe this first order transition on sample#1 and #3 having different thicknesses.

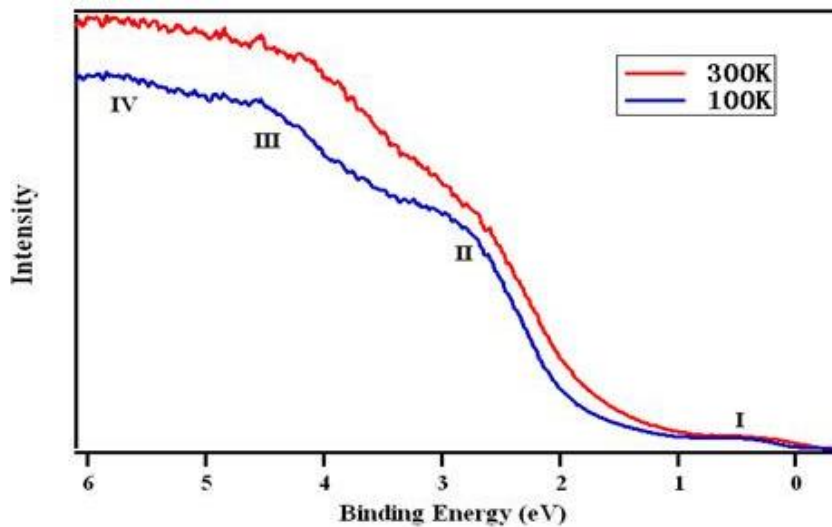


Fig.5.4 Normal emission EDC measured with a photon energy of  $h\nu = 21\text{eV}$  on sample #1 at room temperature (red) and at 100 K (blue). I~IV indicate different structures that will be discussed later on.

In Fig.5.4, we can tell that the major features of the electronic structure are unchanged. II, III and IV features are more clearly resolved at low temperature. Detail information of a gap-opening process happened on feature I is shown in Fig. 5.5. The value of the gap at 100 K is approximately 80 meV. This gap is defined by the crossing point between the tangent and zero intensity. This value is consistent with results in literature. We can see clearly the gap closing when the temperature (150 K) is raised above the Verwey transition.

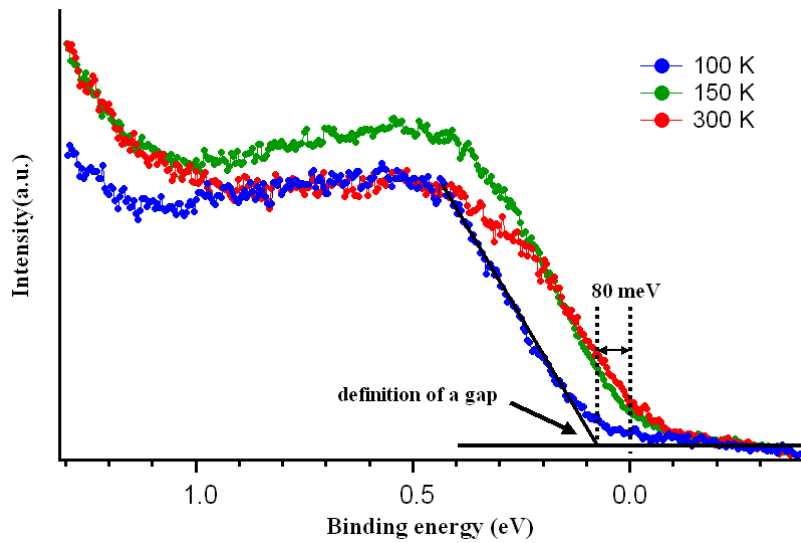


Fig.5.5 EDC measured with photon energy of  $h\nu = 21\text{eV}$  on sample #1 near the Fermi level ( $t_{2g}$  minority band): room temperature spectrum (red); spectra above (green) and below (blue) Verwey transition. The way we used to define a gap is explained in the text.

Sample #3 ( $< 20\text{ nm}$ ) was measured at 165 K and 20 K respectively, and the EDCs are shown in Fig.5.6. The spectrum at 165 K ( $T > T_V$ ) exhibits still an insulator-like gap that obviously disagrees with the metallic nature of  $\text{Fe}_3\text{O}_4$ . Furthermore, the  $t_{2g}$  band observed at 20 K is clearly shifted towards higher binding energy, but the Verwey transition should not be accompanied with such a big shift (see Fig.5.5). Since magnetite is not a good conductor ( $10^6\text{ S/m}$ ), the substrate is insulator and the sample is contacted only by a thin metal wire to the ground, we believe that there is a charging problem on the surface. This very thin sample is not suitable for photoemission determination of the Verwey transition gap.

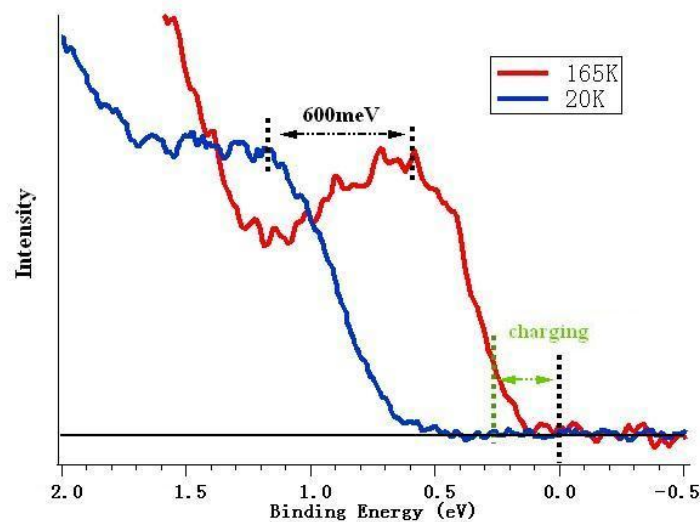


Fig.5.6  $h\nu = 400\text{ eV}$  EDC of sample #3 near Fermi level.

Although Verwey transition characterization failed for thin samples (#3 and #4), LEED, XAS and XMCD measurements are in agreement with literature that indicates a good quality

of the Fe<sub>3</sub>O<sub>4</sub> crystals.

## 5.2 Angle-resolved photoemission

### 5.2.1 Introduction

In an ARPES experiment, the kinetic energy  $E_{kin}$  of the photoelectrons for a given emission angle can be used to determine the crystal momentum. Using the eq. 3.6, we obtain the following expression for the parallel component of the photoelectron momentum:

$$k_{f\parallel} = \sqrt{\frac{2m}{\hbar^2} E_{kin}} \sin \vartheta .$$

So, one can map the band dispersion  $E(k_{\parallel})$  simply by tracking the energy position of the peaks detected in the ARPES spectra for different emission angles ( $\theta$ ). The momentum resolution,  $\Delta k_{\parallel}$ , and neglecting the energy resolution is:

$$\Delta k_{\parallel} \approx \frac{1}{\hbar} \sqrt{2mE_{kin}} \cos\theta \cdot \Delta\theta \quad (5.1)$$

$\Delta\theta$  corresponds to the acceptance angle of electron analyzer. It is clear that the momentum resolution will be better at lower photon energy (i.e. lower  $E_{kin}$ ), and larger polar angle  $\theta$ .

However, due to the abrupt potential change perpendicular to surface, in 3D systems, the perpendicular part of momentum,  $k_z$  ( $k_{\perp}$ ) in Fig. 5.7, is no more conserved across the surface. This  $k_z$  might produce indirect transitions which change the PE final states such that a comparison with band structure calculations becomes difficult.

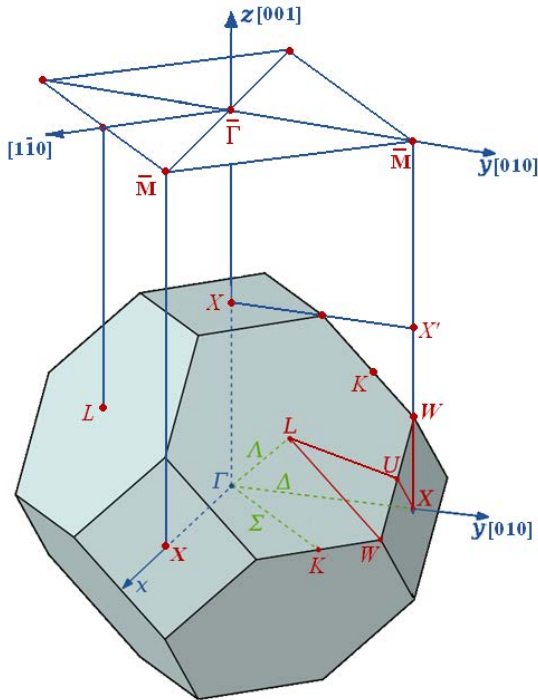


Fig.5.7 3D bulk Brillouin zone (BBZ) of FCC crystal structure and (001) Surface Brillouin zone (SBZ). Two emission (mirror) planes,  $\Gamma XWK$  and  $\Gamma XUL$  are shown. In this thesis, angular dispersion was mapped in the  $\Gamma XWK$  plane.

In the free electron approximation for the final states, it is necessary to determine an adjustable parameter, the so-called inner potential  $V_0$  :

$$k_{\perp} = \frac{1}{\hbar} \sqrt{2m(E_{kin} \cos^2 \theta + V_0)} \quad (5.2)$$

In the experiment we detect photoelectrons emitted along the surface normal (i.e.  $k_{\parallel}=0$ ,  $\theta=0$ ) while varying the photon energy. The photon energy range needs to be large enough to cover at least one Brillouin zone. From the periodicity of structures observed in EDCs and at the same time from the comparison with theoretical band structure, the inner potential  $V_0$  can be deduced. For our samples, this will be done in §5.2.2.

### 5.2.2 Determination of $V_0$

From the ARPES spectra obtained by the 2D detector of the electron analyser (SCIENTA, SPECS), one can extract individual 1D EDCs by fixing  $k$  (i.e. angle  $\theta$ ). It is possible also to plot the photoelectron intensity at a constant kinetic energy as a function of  $k$ . This is called the Momentum Distribution Curve (MDC).

In a normal emission experiment, equation 5.2 can be simplified:

$$k_{\perp} = 0.5123 \sqrt{E_{ph} - \Phi + V_0} = 0.5123 \sqrt{E_{ph} + V'} \quad (5.3)$$

In our experimental geometry we did navigation in the  $\Gamma \rightarrow X$  direction of the bulk Brillouin zone ( $k_z$  in Fig.5.7). In the CASSIOPEE (SOLEIL) experimental setup we used photon energies in the interval from 100 to 200 eV with the step of 3 eV. The Fermi level was measured on a gold foil that was in electric contact with the sample. In the following, the kinetic energy scale was replaced by binding energies (Fig. 5.8).

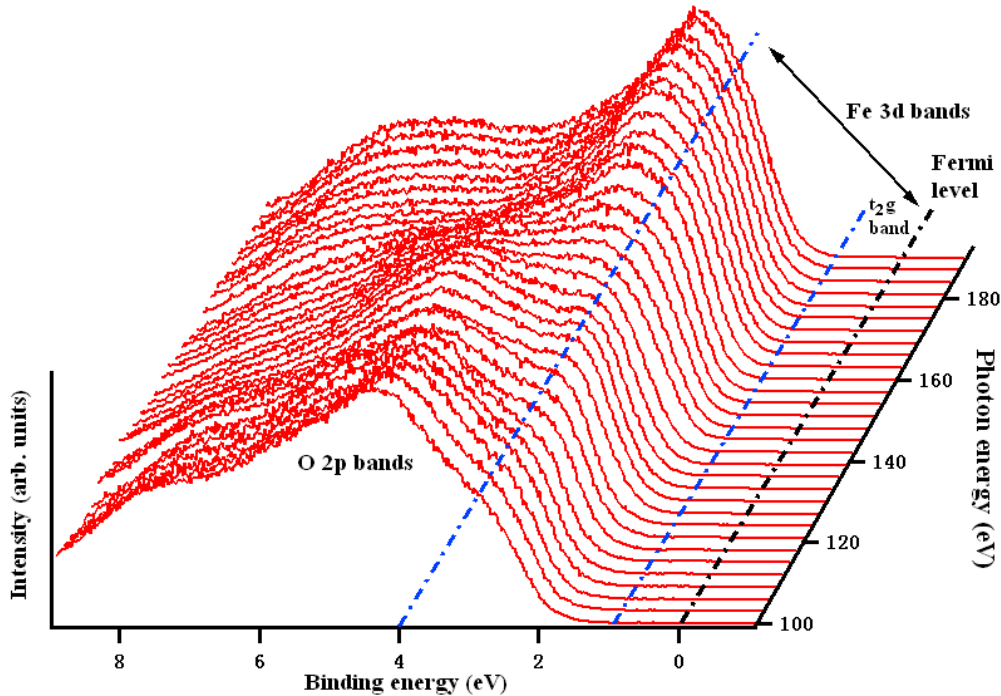


Fig.5.8 Normal emission ARPES spectra of sample #2 recorded with photon energies 100 ~ 200eV.

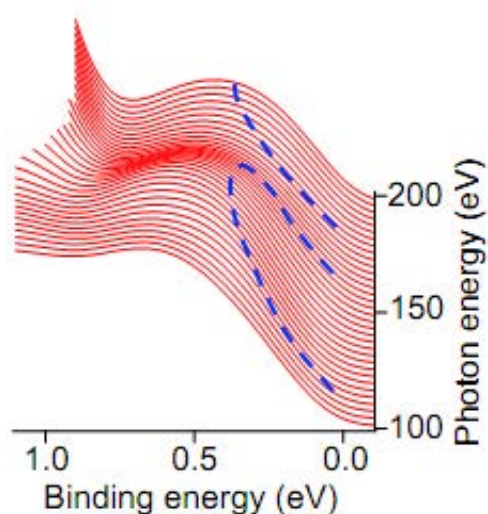


Fig. 5.9. Detailed view of the smoothed  $t_{2g}$  band of the VB spectra. Blue dash line is guide to the eye indicating the  $t_{2g}$  band dispersion as expected in band structure calculations.

defined quasi-particle peak is not observed. This can be explained by a strong electron-lattice coupling that reduces the spectra weight at  $E_F$ , as it is the case in many other transition metal oxides. In the photoemission process, when an electron is removed from such a coupled system, the measured spectrum consists of a coherent quasi-particle peak whose spectral weight is greatly reduced and renormalized in energy, and of an incoherent background of sidebands shifted away from  $E_F$ . In the case of  $Fe_3O_4$ , the electron-lattice interaction, described in the model of small polarons, is so strong that the intensity of the quasi-particle is completely smeared out. It should be noted that a small-polaron contribution to the DC conductivity of  $Fe_3O_4$  has been recognized for decades whereas in the photoemission process it has been addressed only recently.

As  $Fe_3O_4$  is a ferrimagnet, the photo-hole can also be dressed by a cloud of spin wave excitations and therefore can also decay into a spin polaron. [98]

An important aspect of the fermion-boson interaction model is that the first moment of the spectral weight does not change but remains peaked at the frozen lattice electronic energy. Thus we can attribute the hump at around 0.6 eV in Fig. 5.9 to sidebands of quasi-particles strongly dressed by polarons. The blue dotted line is a guide to the eye indicating the  $t_{2g}$  band dispersion expected from calculations.

In order to reveal slight variations in these spectra, the normal emission EDCs raw data are processed by taking the second derivate of  $k_{\perp}$ , shown in Fig. 5.10. Mathematically, the first derivative is the slope of the PES at a certain point; the second derivative is the curvature of the PES at a certain point. As we shall see, the second derivative contains useful information [99][100][101]. In these literatures, the second derivative treatments were done with respect to kinetic energy, we find that in a small kinetic energy range, the second derivative treatment brings more detailed information when it is done with respect to angle (i.e.  $k_{\perp}$ ).

When referring to the band structure calculations, one can qualitatively describe the main structures appearing in the spectra as follows. The features located between -3 eV and Fermi level are due to Fe 3d-derived states. The  $t_{2g}$  band and  $e_g$  band regions are indicated by dashed lines in the Fig. 5.8. The features from 8 eV to 4 eV are mainly due to the O 2p-derived states. [26]

The  $t_{2g}$  band is of particular interest because it plays an important role namely in the half-metallic properties of  $Fe_3O_4$ . From the calculations we know that the electrons at  $t_{2g}$  band correspond to  $Fe_B^{2+}$ .

The intensity of  $t_{2g}$  band is very low, neither a clear cut-off at the Fermi level nor a band dispersion can be observed. Only a slight variation in the spectral intensity is detected (see Fig. 5.9). Clearly, a well-

## Chapter 5: Results and Discussion

Now, a clear dispersion appears as an arc crossing  $E_F$ . Another dispersive arc starts at around 195 eV whose evolution is beyond the photon energy range we used. Comparing the observed dispersion with band structure calculation, we can reasonably suppose that the highest binding energy of this arc can be attributed to the  $\Gamma$  point, which corresponds to a spectrum measured with a photon energy of 133 eV. The energy bands obtained from our GGA+U ( $U = 2.72$  eV) calculation are shown as red solid lines superimposed on the plots. Using the free electron approximation for the final state of the photoelectrons, and taking into account our GGA+U calculations, we find a value of 4 eV for  $V'$  in eq. 5.3. Consequently, the dispersion in the  $k_{\perp}$  direction is located in 3<sup>rd</sup> and 4<sup>th</sup> bulk Brillouin zone along the  $\Gamma \rightarrow X$  high symmetry line. (the momentum unit in the following figures,  $k_{BZ} = 2\pi/a = 1.496\text{\AA}^{-1}$ )

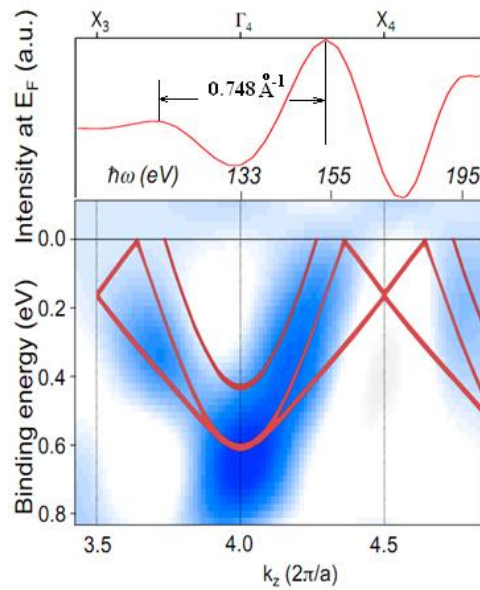


Fig.5.10 Plots of the second derivative picture of the ARPES data showing band dispersion. The superimposed red lines are the ground state  $t_{2g}$  bands given by GGA+U (2.72 eV) calculation. Calculated ground state data (solid red lines in the lower panel) are superimposed for comparison. The upper panel shows the spectral weight intensity variation at  $E_F$ .

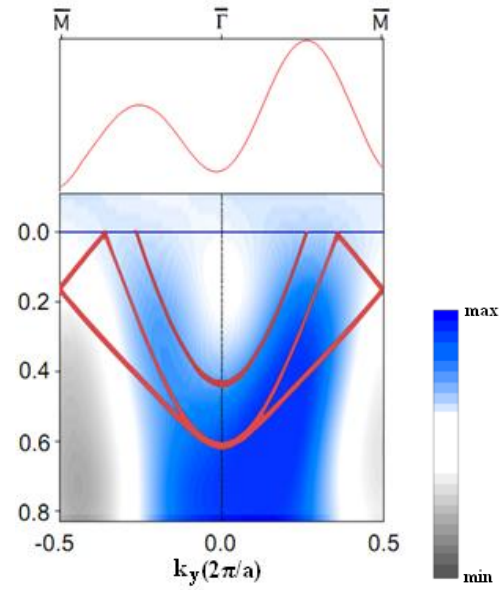


Fig.5.11 Plots of the second derivative picture of the ARPES at 133 eV. The  $k_y$  direction corresponds to the  $\bar{\Gamma}\bar{M}$  high symmetry line in the surface BZ. Calculated ground state data (solid red lines in the lower panel) are superimposed for comparison. The upper part shows the spectral weight intensity variation at  $E_F$ .

### 5.2.3 ARPES analysis in critical points of the bulk Brillouin zone

Photoemission being a surface sensitive technique, a contribution of the surface electronic structure to the spectra is expected. In this context it is remarkable that we observe bulk bands in spite of the  $(\sqrt{2} \times \sqrt{2})R45^\circ$  reconstruction. When looking for a signature of surface states one needs to keep in mind that in our experimental geometry the (001) surface reconstruction is arranged in such a way that in the reciprocal space its BZ is exactly half of

Chapter 5: Results and Discussion

that corresponding to the ideally truncated bulk Crystal (fig. 5.12). As a matter of fact, we observe both periodicities, i.e. one corresponding to 8.4 Å (reconstructed surface) and another to 4.2 Å (primitive lattice), as shown in the intensity profile at  $E_F$ , fig. 5.10, upper panel. The  $t_{2g}$  band is therefore folded in such a way that it crosses  $E_F$  at the edges of the reconstructed surface BZ.

At this stage, it deserves cross-checking whether these spectral features are still present when measuring the angle-resolved spectra which is sensitive to surface structure. The most appropriate is to choose  $h\nu = 133$  eV for which we have identified the  $\Gamma_4$  (in the 4<sup>th</sup> BZ as deduced by eq. 5.3) point of the bulk BZ. The results are displayed in Fig. 5.11. For this photon energy the  $\Gamma_4$  and  $\bar{\Gamma}$  points as well as the  $X_{3,4}$  and  $\bar{M}$  points are superimposed and the spectra are measured along the [010] ( $k_y$ ) direction, see fig. 5.7 and 5.12 (b). In this thesis, the polar angle measured by analyzer corresponds to  $k_{||}$  ( $k_y$ ) dispersion as seen in Fig.5.13 (c).

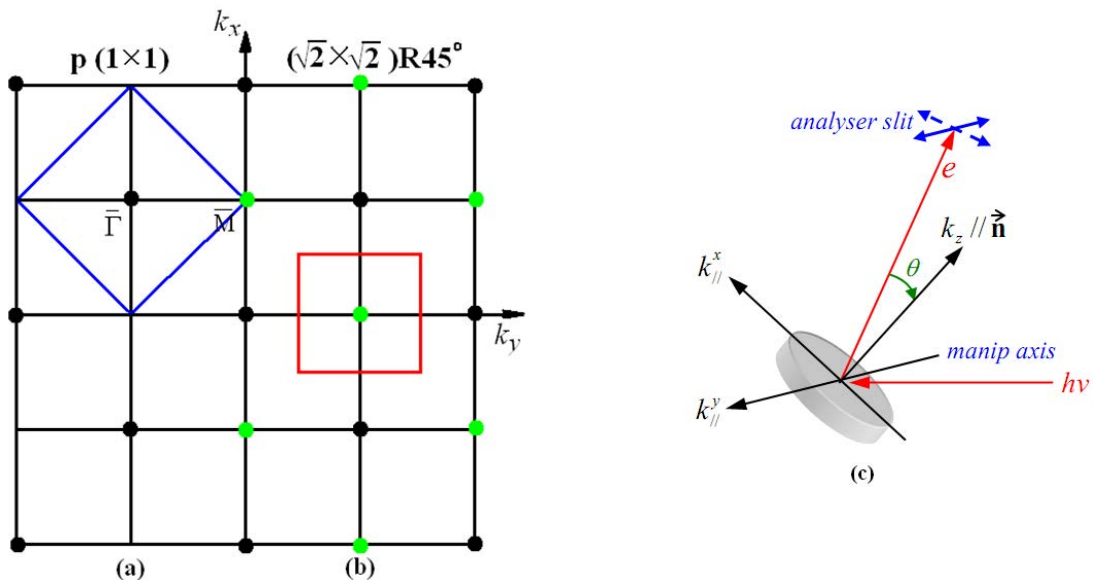


Fig.5.12 (a) blue square: SBZ of non-reconstructed FCC crystal; (b) red square: SBZ of  $(\sqrt{2} \times \sqrt{2})R45^\circ$  reconstructed FCC crystal; black spots: conventional lattice point of SBZ in  $k_x k_y$  plane; green spots: additional lattice point due to reconstruction on  $Fe_3O_4$  (001) surface; (c) experimental geometry of ARPES apparatus. The polar angle corresponds to the  $k_{||}^y$  component

The simulation shown in Fig. 5.13, using the parameters defined in § 4.2, exhibits similar features as those in Fig. 5.10. At binding energy of about 0.6 eV is the intensity maximum of the dispersion arc centre and the band crosses  $E_F$  nearly in the middle between  $\Gamma$  and X.

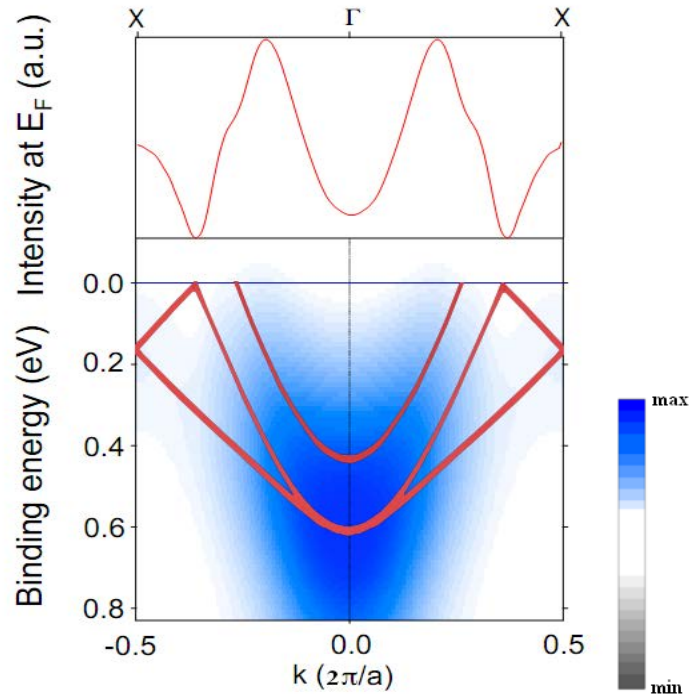


Fig.5.13 Simulation of the experimental data. Calculated ground state data (solid red lines in the lower panel) were convoluted by Lorentzian and Gaussian functions to account for the lifetime and electron-phonon coupling effects, respectively. The upper panel shows the spectral weight intensity variation at  $E_F$ .

If we choose  $h\nu = 154$  eV, corresponding to  $k_z$  where the band is crossing  $E_F$  (Fig. 5.10), the intensity profile determined at  $E_F$  for the dispersion in the  $[010]$  ( $k_y$ ) direction is inverted: the maximum intensity is now observed in normal emission. (See Fig. 5.14)

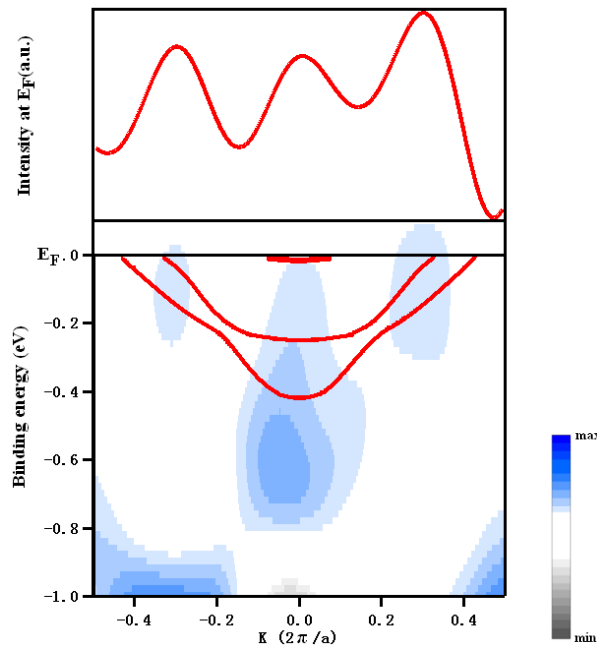


Fig. 5.14 Plots of the second derivative picture of the ARPES at 154 eV with ground state GGA+U calculation of  $k_z = 0.75 (2\pi/a)$ . The upper part shows the spectral weight intensity variation at  $E_F$ .

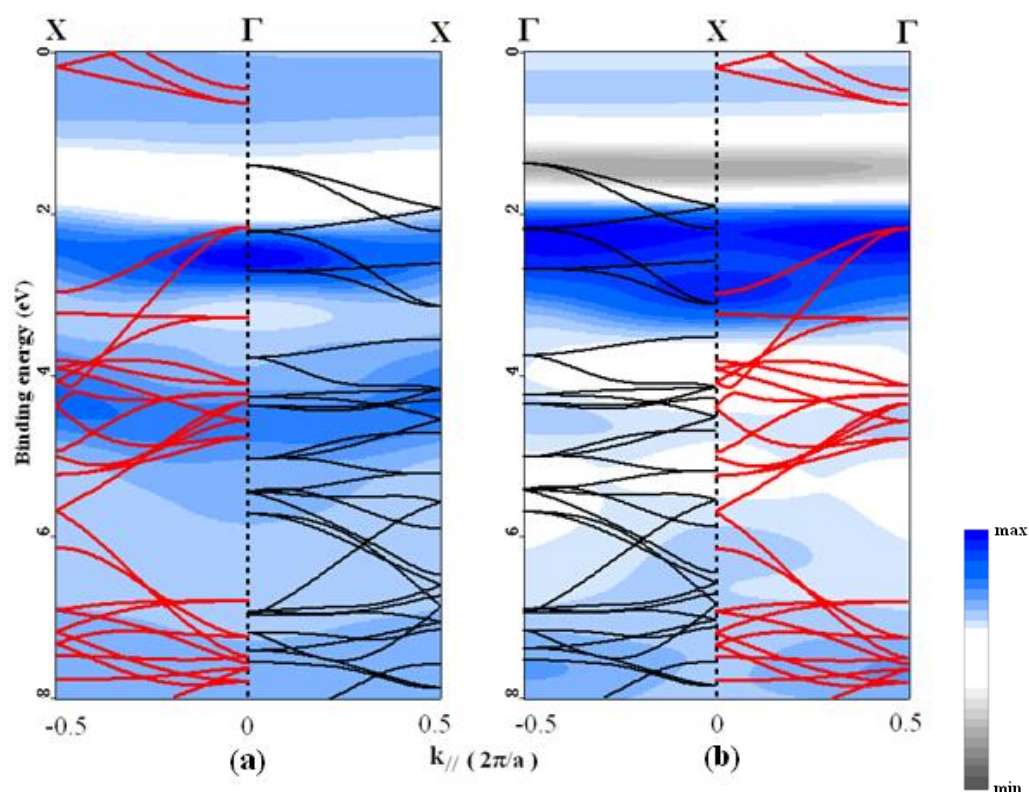


Fig.5.15 Second derivative plots of ARPES spectra measured with photon energy of (a) 133 eV ( $\Gamma$  point) and (b) 175 eV (X point). The GGA+U calculated ground state bands are superimposed. Red curves are minority spin bands and black curves are majority spin bands.

Until now, only the  $t_{2g}$  minority band was analyzed, in the Fig.5.15, we present the results of a big valence band range in order to see the accuracy of GGA+U calculation. We take  $h\nu=133\text{eV}$  ( $\Gamma$  point) and  $h\nu=175\text{eV}$  (X point) as examples in the second derivative plot with respect to kinetic energy (i.e. binding energy in Fig.5.15). In this figure, the positions and dispersion of the intensity plot has a quantitatively agreement with the ground state calculated by GGA+U. In spite of the fact that we cannot distinguish the spin polarization in the spectra, superimposed spin-resolved calculated bands, red and black lines in Fig.5.15 (a) and (b) can give us intuitive information about the spectral weight of different spins.

A more detailed simulation is shown in Fig. 5.16 ( $\Gamma$  point) and in Fig.5.17 (X point) where we compare a single EDC spectrum with GGA+U calculations. Blue lines are measured spectra and in the upper part of the figures the green colour represents the second derivative of the measured curves. For a better understanding of both spin contributions, the simulation is shown separately for spin up (black solid lines) and spin down (red solid lines) electrons. The spin integrated spectrum is plotted in red dotted lines.

From the figures we can draw several conclusions.

i) the positions of different structures in the experimental spectra are well reproduced by calculation. So, GGA+U has acceptable accuracy to calculate  $\text{Fe}_3\text{O}_4$ .

ii) the simulated spin-resolved curves give a qualitative estimation of the spin polarisation in the spectral structures. This can be useful for future experiments.

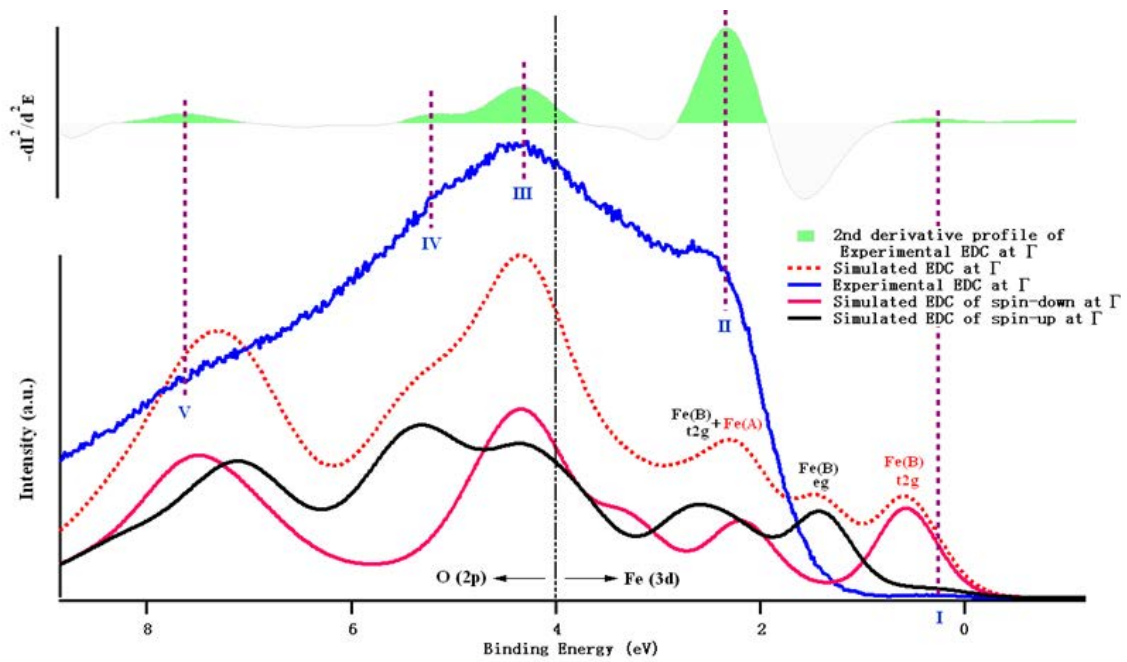


Fig.5.16 EDC in  $\Gamma$  point (blue) and its second derivative (green colour in the upper part). The spin-integrated simulated spectrum is shown by the red dotted line. Spin down (red) and up (black) contributions are also shown. Different spectral structures, numbered from I to V, are well reproduced by the simulation.

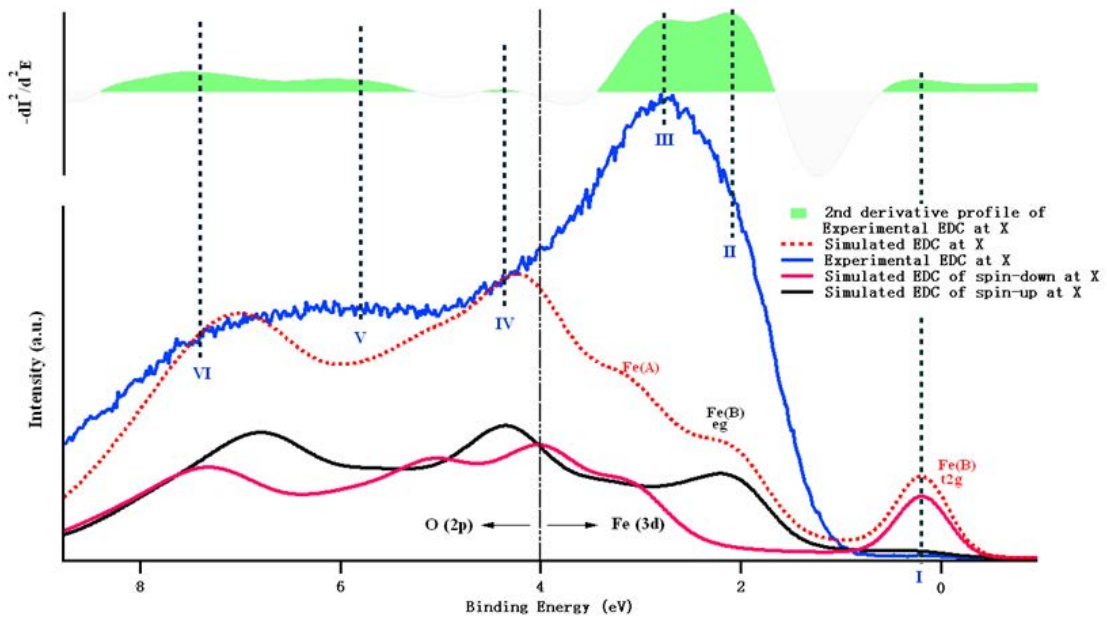


Fig.5.17 EDC in X point (blue) and its second derivative (green colour in the upper part). The spin-integrated simulated spectrum is shown by the red dotted line. Spin down (red) and up (black) contributions are also shown. Different spectral structures, numbered from I to VI, are well reproduced by the simulation.

## Chapter 5: Results and Discussion

iii) the spectral weight of the  $t_{2g}$  minority band is much smaller in the experimental curves. This is most probably due to matrix elements effects in the photoemission process that are completely neglected in the simulation. Another possibility is that our sample is partially oxidized in the surface region of the sample, resulting in a reduced concentration of B-site  $\text{Fe}^{2+}$  ions. Hence the spectra weight for Fe (B) bands in both figures is very small.

iv) the spectra weight is changed for different photon energy because the matrix element is a function of photon energy and it can be explained by the Fermi-Golden rule (Appendix A)

In order to crosscheck our results, we compared sample #2 and #4. Sample #4 was thinner (<20nm) and consequently a charging effect of about 300meV was induced (Fig.5.18 inset).

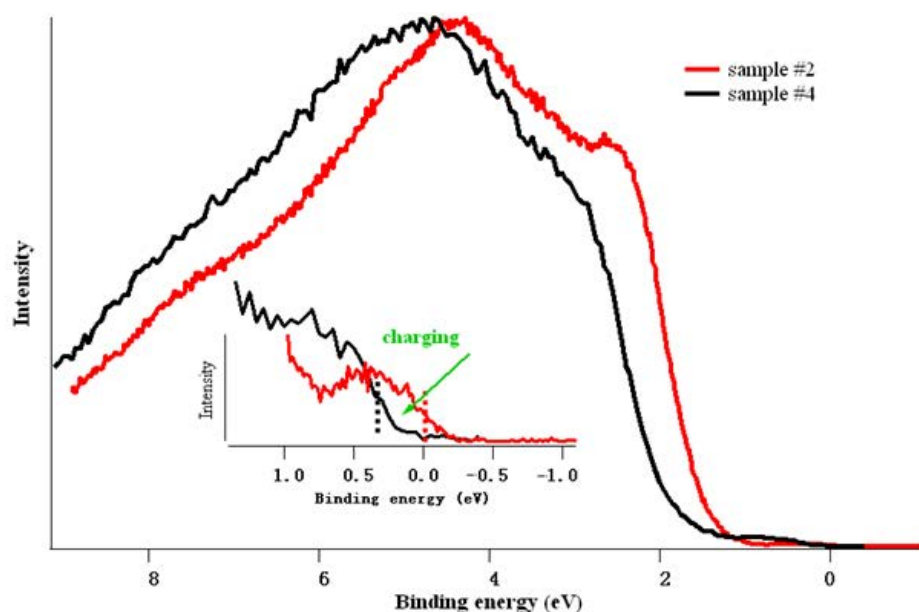


Fig.5.18 Normal emission EDC at a photon energy of  $h\nu = 133\text{eV}$  measured on sample #2 (red) and #4 (black). In the inset the zoom on the  $t_{2g}$  band clearly shows the space charging effect.

This effect is also seen in another thin sample (#3) during the measurements of the Verwey transition (§5.1.2). To do a comparison, the spectra of sample #4 are shifted towards the Fermi level. As seen in fig. 5.19 the results obtained on sample #2 are very well reproduced. The azimuth angle ( $\phi$ ) of sample #4 was well adjusted to the [001] direction. In spite of the fact that the sample was very thin, after choosing a good Fermi level position the major band dispersions fit the calculation well (see Fig.5.19). An off normal geometry ( $-10^\circ$  for  $\theta$ ) was used to enlarge the negative polar angle range so as to increase the measured part of the BZ.

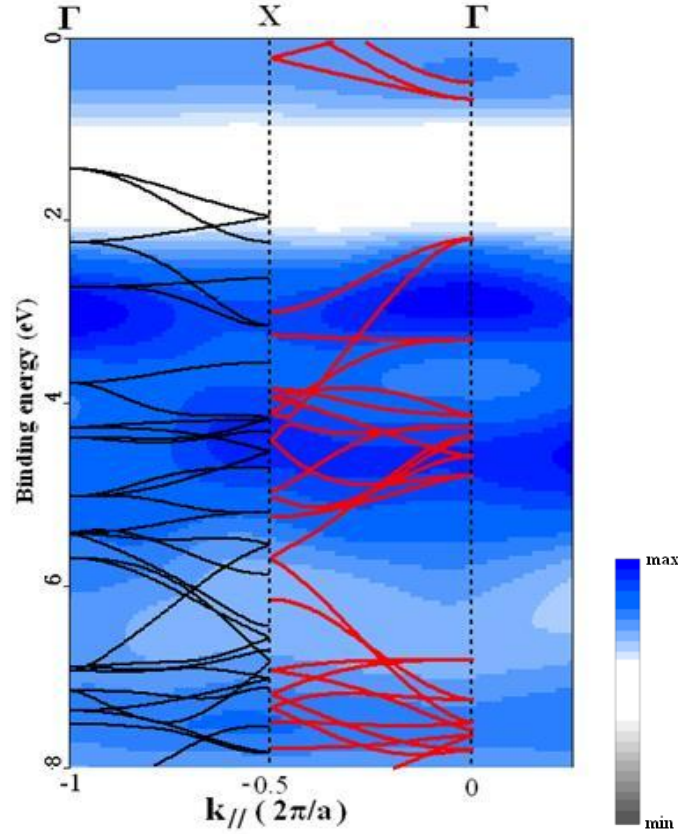


Fig. 5.19 Off normal ARPES measurement at photon energy of  $h\nu = 133\text{eV}$  on sample #4.

(a) emission angle is transferred into  $k_{//}$  and only one BZ of second derivative spectrum is plotted. GGA+U ground state minority and majority bands are shown by red and black curves, respectively.

#### 5.2.4 ARPES analysis at photon energy of 21eV

A set of measurements was also done at low photon energy (21eV) on sample #1. Rotating the sample in polar angle (Fig.5.20) allowed measurements in a wider emission angle range. Individual spectra were attached together and the resulting spectrum is shown in Fig. 5.21. For low photon energies this operation is necessary if one intends to map all bulk Brillouin zone, at a photon energy of 21 eV,  $\theta = 40^\circ$  is necessary.

According to the relationship between the emission angle and the free electron final state momentum vector from Fermi level:

$$\frac{2\pi}{a} = \frac{\sqrt{2mE_{\text{kin},F}}}{\hbar} \sin \theta_T \quad (5.4)$$

where  $E_{\text{kin},F}$  is the kinetic energy of an electron from the Fermi level,  $\theta_T$  is the angle corresponding to one Brillouin zone.

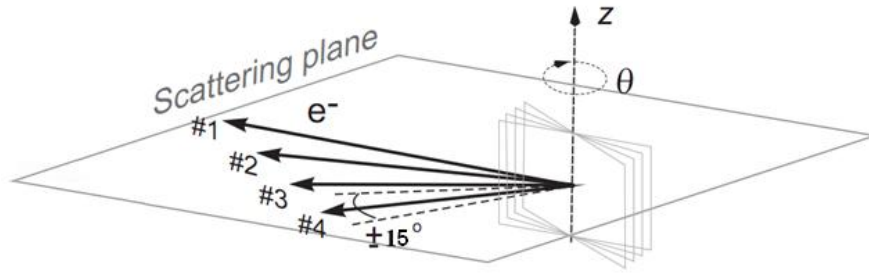


Fig.5.20 schematic view of sample rotation in polar angle

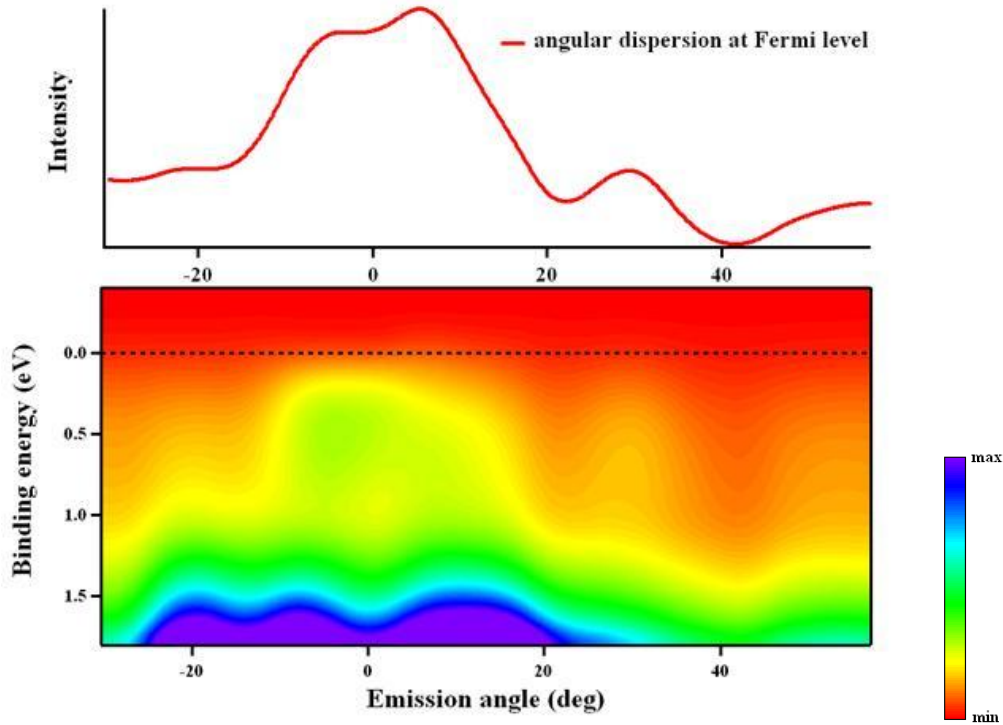


Fig.5.21 Wide-angle ARPES. Individual spectra measured at different polar angles are attached together and smoothed. (blue is high intensity and red is low intensity) Upper panel shows the spectral intensity at  $E_F$  ( $E_F$  reference was measured on Ag film)

As already stressed, in the photoemission signal we expect contribution from both surface and bulk electronic structure. Taking into account the inner potential we have determined in § 5.2.2, at the photon energy of 21 eV,  $k_{\perp}$  is located at  $1.7(2\pi/a)$  from the  $\Gamma$  point on the  $\Gamma X$  high symmetry line of bulk Brillouin zone (Fig. 5.7).

Comparison between experimental and simulated spectra is shown (Fig.5.22, 5.23). The normal emission EDC shows a good qualitative agreement between experiment and simulation. Especially the position of the  $t_{2g}$  band corresponds well (Fig.5.23). However, there is a clear disagreement at in the white dashed line region. This is probably a contribution from the surface reconstruction. In fact, a periodicity of  $21^\circ$  is observed in Fig.5.21, upper panel, which corresponds to one reconstructed surface BZ.

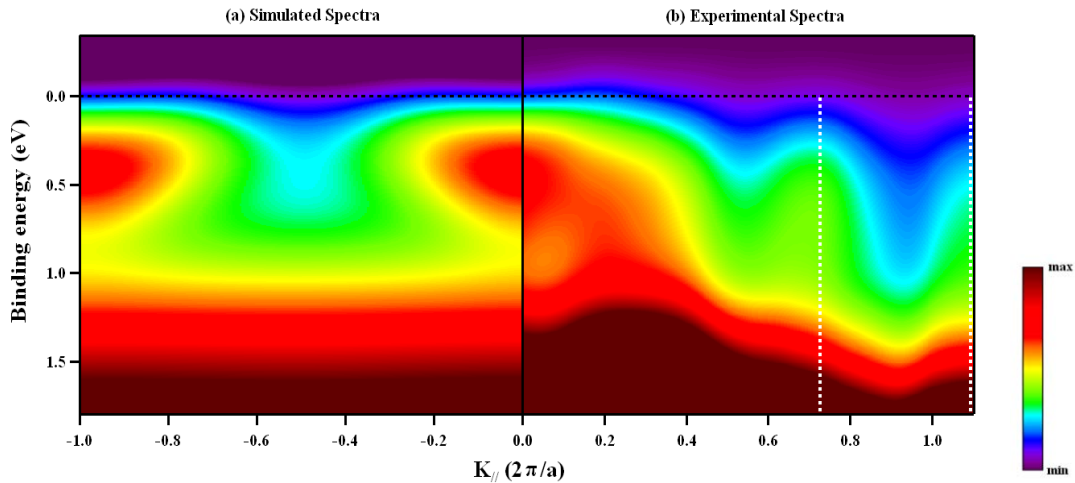


Fig.5.22 Comparison between experimental spectra and bulk simulated spectra at  $k_{\perp}=1.7 (2\pi/a)$ ; angle was transferred to momentum unit in (b); the distance between white dashed lines corresponds to  $21^{\circ}$ .  
Red: high intensity, blue: low intensity<sup>o</sup>

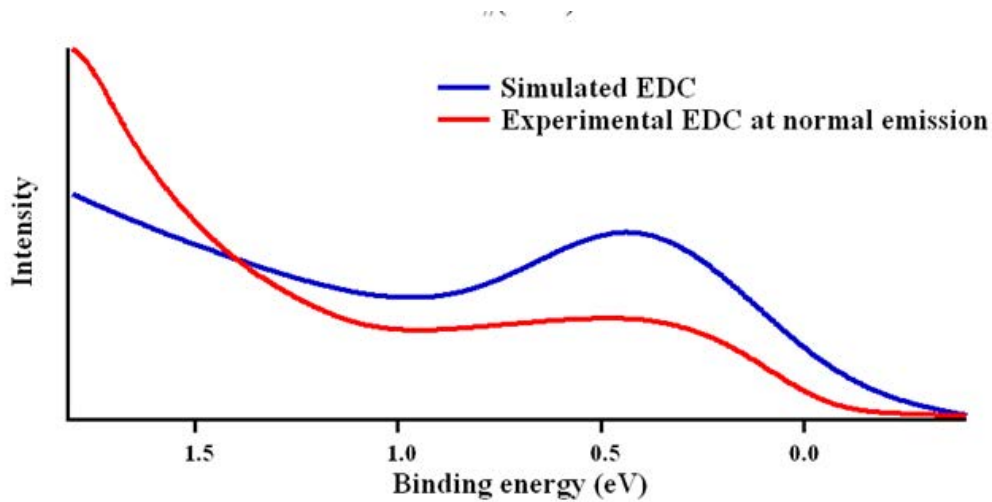


Fig.5.23 Red line: Experimental EDC at normal emission. Blue line: simulated EDC from GGA+U calculation (both, the hole lifetime and polaron effects are included)

### 5.2.5 Fermi surface map by ARPES

By integrating the spectral intensity over an energy interval of 100 meV at  $E_F$ , we map a series of MDCs measured by different photon energy from 100 eV to 200 eV in one image (Fig 5.24). Then transfer emission angle ( $\theta$ ) into  $k_{\parallel}$  ( $k_y$ ) and photon energy into  $k_{\perp}$  ( $k_z$ ), an unconventional Fermi surface plot is obtained (Fig.5.25). Although its existence has been predicted by theory, this is the first experimental evidence of this FS. It is to be noted that in this unconventional plot,  $k_z$  represents bulk electronic properties and  $k_y$  the surface properties. This gives the possibility to unravel differences between surface and bulk electronic structure. Surprisingly, these two structures give the same symmetries and periodicities indicating again that the influence of the surface states is negligible.

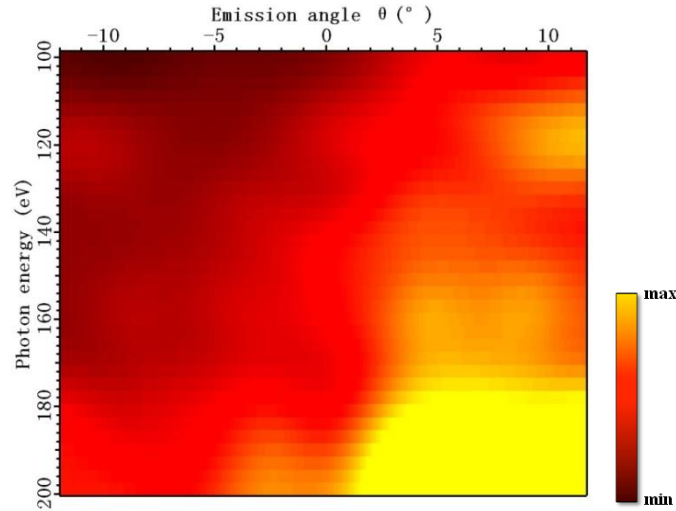


Fig.5.24 Series of MDCs at  $E_F$  measured by photon energy from 100eV to 200eV

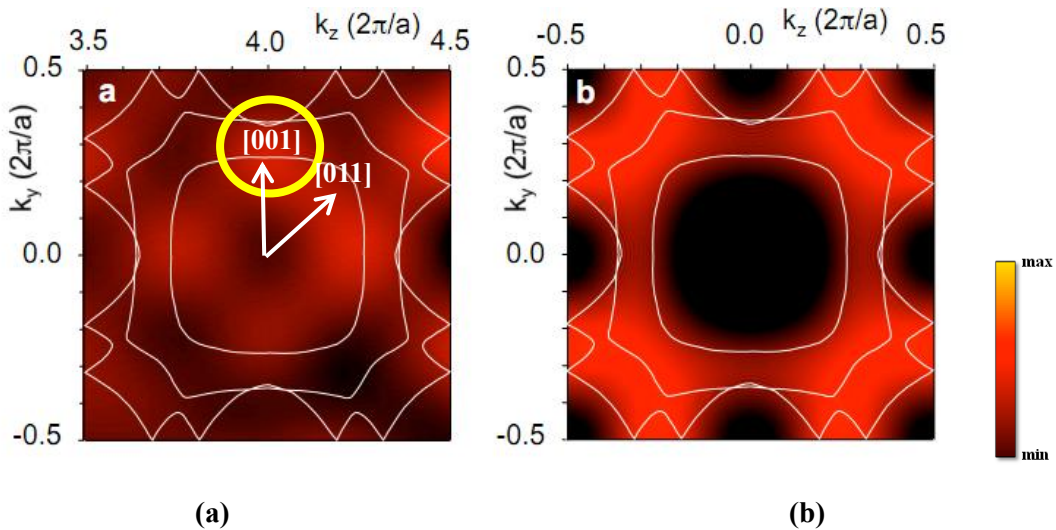


Fig.5.25 Plots of the FS intensity in which the white lines show the ground state FS contours calculated by GGA+U calculation. (a): second derivative image from ARPES data; (b) simulation by the parameters in Fig.4.9

The experimental FS fits with the overall symmetry of the underlying ground state band structure (superimposed white lines). We also performed a simulation of the FS using the procedure and the parameters mentioned in §4.3. A qualitative agreement with the experiment is achieved especially in the corners of the BZ. The major difference between the experiment and simulation is the four bumps in the central part (yellow circle). In this case, the failure of our simple model (unable to describe the spectral intensity distribution through the whole BZ) might be due to strong anisotropy of the polaron interaction [102][103] giving rise to intensity enhancement approximately in the middle of the  $\Gamma X$  high symmetry axis [001], i.e. in the particular points where the  $t_{2g}$  band cross  $E_F$ .

## 5.3 Spin-resolved photoemission

### 5.3.1 “Static” spin polarization measurement

Determination of electron spin polarization is an ultimate test of both the band calculations and our model of  $\text{Fe}_3\text{O}_4$  photoemission spectra. Spin-resolved photoemission measures not only the spin state but also the energy and momentum of such states and is therefore sensitive to spin structures in reciprocal space. In this sense, it is a complete experiment with detailed information on the exchange-split bands of itinerant ferromagnets.

The experiment was performed with a Ti-Sapphire laser and amplifier (RegA) with a high repetition rate of 250 kHz, 150fs pulse duration. Using BBO crystals, we generated 3<sup>rd</sup> harmonic (4.65eV) and 4<sup>th</sup> harmonic (6.2eV) beams. These photon energies allow us to perform single photon photoemission. The experiment was performed in an UHV chamber equipped with a Time-of-Flight spin-resolved (TOF) electron analyser having an energy resolution less than 5 meV. All electrons emitted in a small solid angle are collected in the TOF analyser and spin resolved with a Mott detector (25 kV accelerating voltage).

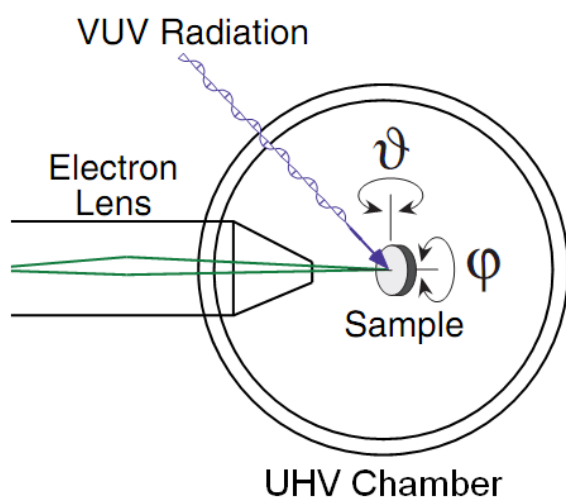


Fig.5.26 Schematic view of SRPES emission chamber

The sample can be rotated by  $\theta$  and by  $\phi$ .  $\theta$  determines the emission angle and  $\phi$  changes the magnetization direction. In a single Mott polarimeter two pairs of detectors can be placed in two orthogonal scattering planes (vertical, V, and horizontal, H), thus measuring the two spin components transverse to the beam direction. Hence, the measured asymmetry in the Mott detector depends on the spin direction of scattered electrons.

As shown in Fig. 5.27 (a), when  $\phi=0^\circ$  or  $\phi=-90^\circ$ , only one pair of detectors should obtain an asymmetry. Furthermore, considering that the laser source is linearly polarized and the beam is parallel to the magnetization direction in the case of  $\phi=0^\circ$ , the statistic is relatively low in  $\phi=-90^\circ$  geometry; when  $\phi=-45^\circ$ , both pairs of detectors obtain the same asymmetry. No clear  $\theta$ -dependent dispersion can be observed with these low photon energies and this is why we concentrate on normal emission.

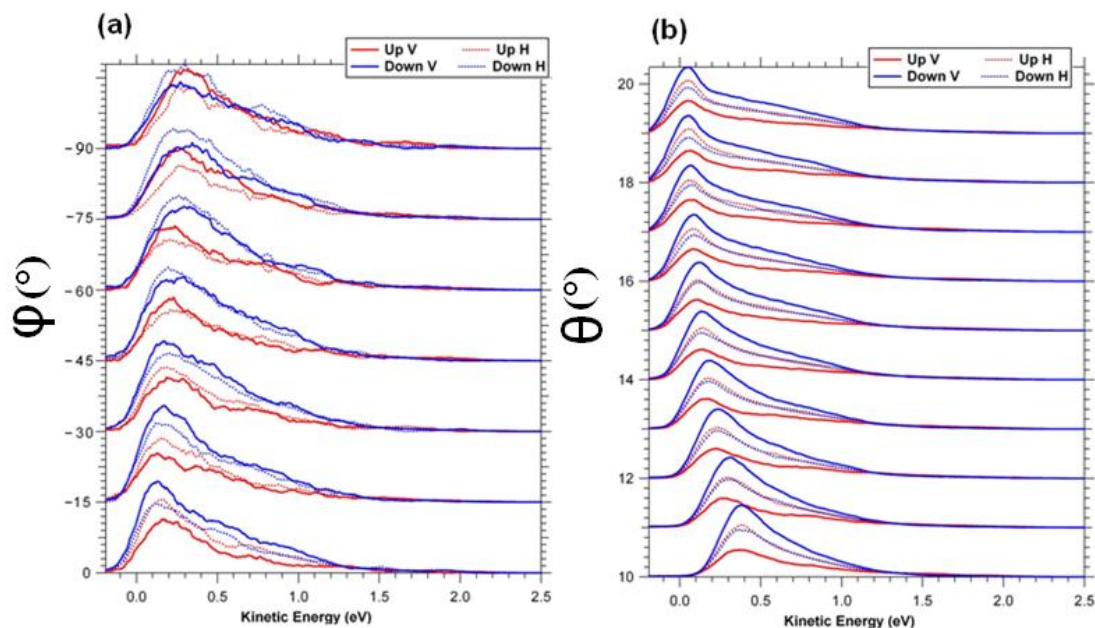


Fig. 5.27 (a) EDC in 4 channels of Mott detector changing  $\phi$ ,  $\theta=0^\circ$ . (b) EDC in 4 channels of Mott detector in  $\theta$  when  $\phi=0^\circ$ . V (vertical), H (horizontal) represents a pair of detectors.

Usually, SRPES has a fundamental difficulty: photoelectrons have a relatively short inelastic mean free path. The real photoemission intensities consist of the contribution of the intrinsic full multiple-elastic scattering photoelectron and extrinsic inelastic scattering electrons. Extrinsic inelastic processes occur along the way as photoelectrons propagate towards the surface, and collected energy losses move them from the elastic peak position to a smoothly rising inelastic background on the higher binding energy side, underneath the intrinsic spectrum. The electrons in the inelastic background do not reveal the spectral intrinsic information due to the random nature of the inelastic processes. Inelastic scattering cross sections are very high, and values of mean free path can be an important factor of influence for spin polarization measurement. However, in our case, the very low photon energy gives a large enough mean free path for photoelectron, more spin information from the bulk crystal was obtained. According to the universal curve of inelastic electron mean free path, for 4 eV and 6 eV, the estimated depth of sensitivity is around 10 nm.

It is worthwhile to mention that the same sample was used as for ARPES, requiring its transfer through air to another chamber. The sample was not subject to any cleaning procedure prior to the SRPES measurements that logically leads to a reduction of the spin polarization as a consequence of the presence of a bad layer (contamination, non-stoichiometric composition) on the surface. Even though, the spin polarization close to  $E_F$  reaches -50% and -72% for 6.20eV and 4.65eV respectively, as shown in Fig.5.28

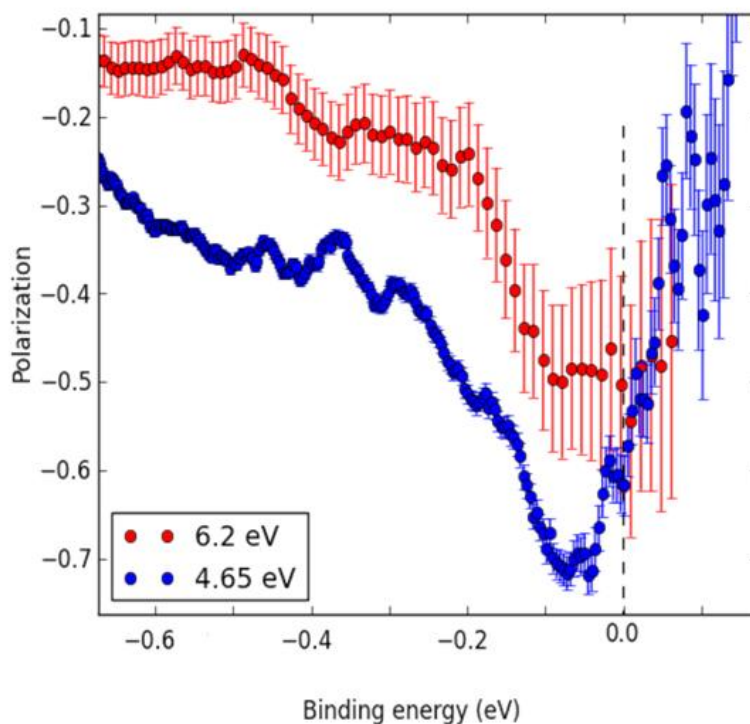


Fig.5.28 Spin polarization curve deduced from SRPES for different photon energy (red: 6.2 eV; blue: 4.65 eV) at normal emission. (Error bar reflects the statistics in experiment,  $1/\sqrt{\text{counts}}$ )

Our results can be compared to an in situ prepared (001) surface for which a polarization of - 55% was reported [65][67]. This seems to be the maximum value of polarization ever reported on the (001) surface. The reduction of the polarization as compared to -100% is explained by the reconstruction and the stabilization of the (001) surface leading to lattice distortions and consequently to strong changes in the electronic properties. To our knowledge, the only calculation of the electronic structure of the reconstructed surface is unable to give a clear description of it, the polarization at  $E_F$ , is heavily underestimated, giving the value of -40% [67]. The high value of spin polarization we observe can be explained by an increase in the inelastic mean-free path, which probes bulk properties more efficiently.

The simulation of the polarization, Fig.5.29 (b), in the  $\Gamma \rightarrow X$  direction uses the parameters and method mentioned in chapter 4. Spin-down and spin-up ground state bands are superimposed on the polarization intensity plot as red and black lines, respectively. Clearly, our spin polarization measurements are consistent with the band-like description of the electronic structure as seen from the comparison between the simulated spin-polarized spectrum in the X point (blue curve in the lower panel of Fig.5.32 a), extracted from Fig.5.29 (b) and the measurement. The maximum negative polarization value and even the point of polarization reversal (the binding energy position where the sign of spin polarization changes) are fairly well reproduced. This reversal can also be deduced from Fig.5.16.

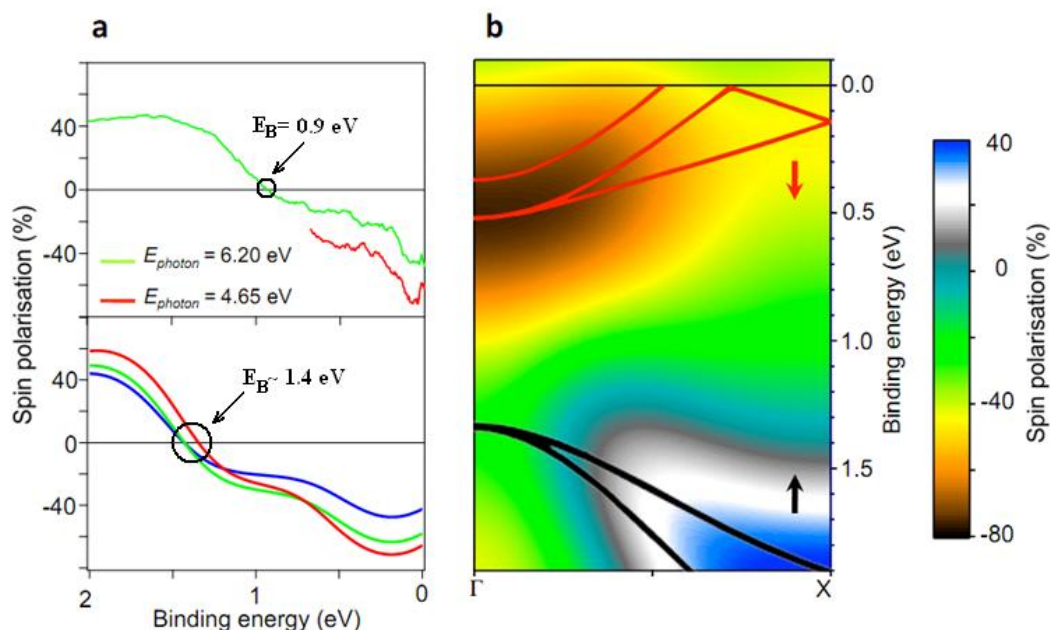


Fig.5.29 (a) Upper panel: spin polarization deduced from SRPES at normal emission of 4.65eV and 6.20eV; bottom panel: the spin polarized spectrum at X point extracted from (b). Simulations for 6.2eV (green) and 4.65eV (red) are shown for comparison. (b) Simulation for the spin polarization in  $\Gamma X$  plane. Red and black lines are spin-down and spin up ground state bands respectively

In our model, the photoemission signal is formed by adding up contributions from electron bands at all binding energies. As a consequence, values of spin polarization at  $E_F$  are less than -100% even if measured at the  $\mathbf{k}$  position where bands are predicted to cross  $E_F$ . In general, the situation can be even more complex when using “standard” photon energies, i.e. when the electron mean-free path is close to the minimum of the “universal curve”. Due to the three-dimensional nature of  $\text{Fe}_3\text{O}_4$ , the  $\mathbf{k}_\perp$ -broadening effects in the final state results in an additional contributions from all  $\mathbf{k}$  in the BZ, reducing even more the spin polarization. This complicates the analysis of the spectral function in three-dimensional systems.

Interestingly, the polarization marks a considerable increase at 4.65eV. At first sight, only the argument of electron mean free path can be put forward to justify this increase because the polarization dispersion is rather flat and changing the photon energy from 6.2eV to 4.65eV corresponds to a step in the momentum space of about 15% on the  $\Gamma \rightarrow X$  direction. Moreover, our simulation takes into account the initial-state lifetime broadening on the energy scale over a wide VB region and ignores the matrix element (blue simulation curve in Fig.5.29 (a) bottom panel). In this case, due to the width of Lorentzian function, intensities at  $E_F$  from deep BE in the VB make a considerable contribution. When applying the exact BE range covered by the given laser photon excitation energy in the simulation, higher polarization values are obtained. This is one of the most crucial points in the interpretation of spin-polarized data as measured by photoemission (red and green curve in Fig.5.29 (a) bottom panel).

Our simulation can be refined further by considering that the missing electron interacts strongly with one additional electron-hole pair in the three body scattering approximation, which augments the approach of many-body correlation. It is expanded on the configurations

obtained by adding single electron-hole pairs to the ground state of the single particle Hamiltonian. Then the correlation effects are related not only to the strength of the electron-electron interaction but also to the band occupation which decides the efficiency of scattering ( $e-h$ ,  $e-e$ ). For  $\text{Fe}_3\text{O}_4$ , the 3d band occupation of majority and minority spin is different, i.e. majority 3d band is completely filled and minority 3d band is partly filled. The creation of a majority spin hole will be followed by scattering processes involving mainly opposite spin electron-hole pairs; conversely the creation of a minority spin hole will correspond to scattering between parallel spin particles. The different strength of the interaction among opposite spin particles and parallel spin ones gives rise to spin-dependent self-energy renormalizations which affect majority spin states more than minority spin ones [104]. The effect of self-energy renormalization on majority spin states close to  $E_F$  results in increased spectral functions and thus reducing the polarization.

### 5.3.2 Measurements of the spin dynamics

#### *Introduction*

For decades, the magnetization of itinerant ferromagnets has been observed to be reduced within the first few hundred femtoseconds of relaxation. This ultrafast variation has been suggested to be due to a momentum transfer from the spin to the orbital degree of freedom and to Elliot-Yafet type spin-flip scattering. The work of Uwe Bovensiepen [105] supports the direct interaction between hot electrons and spin system for ferromagnetic metal, while Georg M. Mueller [106] et al found this scattering is blocked for half-metals because there are no spin channels for spin-flip scattering and the energy must be transferred in lattice excitation. In this section, we present one of the first experiments studying spin-resolved dynamics of a half metal by photoemission.

Using femtosecond laser pulses, we can create an excited electron distribution, however the microscopic mechanisms responsible for the relaxation of hot electrons and spins are unclear to date.

Unlike conventional photoemission, which uses one-photon photoemission (1PPE), two-photon photoemission (2PPE) measurement allows us to investigate occupied states as well as unoccupied electronic states located between the Fermi level and the vacuum level. The schematic 2PPE process for studying unoccupied state is illustrated in Fig.5.30 (a). Electrons from the VB are excited into an intermediate state with a pump pulse,  $h\nu_1$ . The probe pulse  $h\nu_2$  ejects the excited state electron by giving it energy greater than the vacuum level. The case of an occupied state is shown in Fig.5.30 (b). Without resonant excitation into a real intermediate state, 2PPE occurs via a virtual state in a coherent two-photon process.

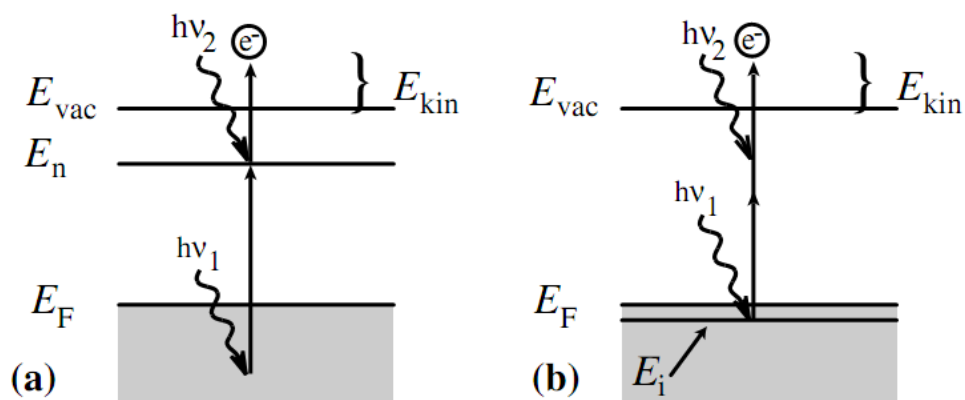


Fig.5.30 (a) Schematic energy diagram for 2PPE of an initially unoccupied state; (b) The 2PPE process for an initially occupied state.

Spin dynamic information can be obtained by Time- and Spin-resolved 2PPE. The intensity recorded from a given intermediate state as a function of the variable time delay between the sufficiently short pump and the probe pulses is determined by the lifetime of the intermediate state. To fully explore the dynamics of electrons on the surface, the experimental technique should probe the electron dynamics on the femtosecond time scale. A typical setup for time-resolved 2PPE experiment is shown in Fig.5.31.

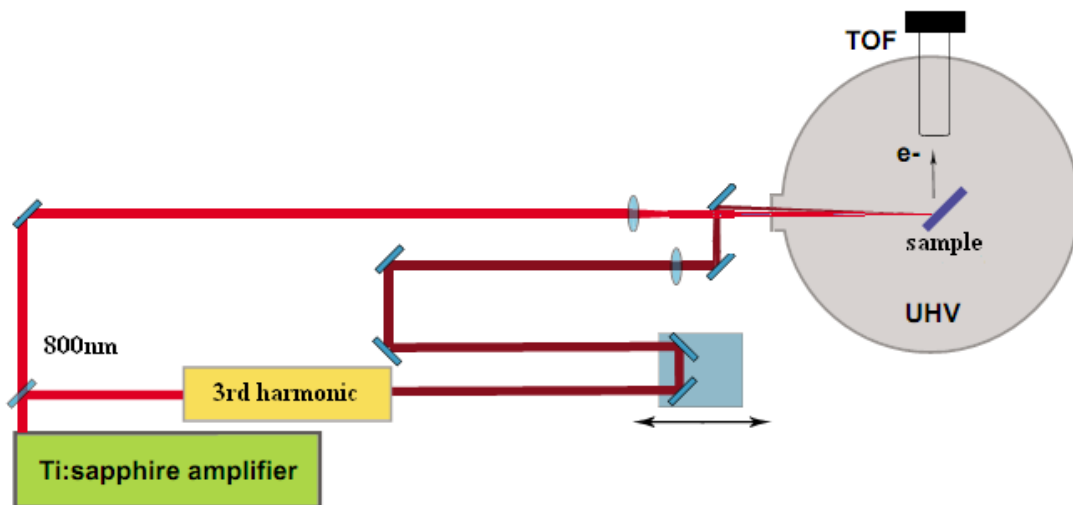


Fig.5.31 Schematic setup for time resolved 2PPE experiment. The 3<sup>rd</sup> harmonic beam is generated by an optical parametric amplifier and non-linear optical material BBO

The role of the probe pulse  $h\nu_2$  is to monitor the ultrafast changes of the electron distribution and kinetic energies. Pump and probe pulse are time delayed with respect to each other and focused onto the sample. In this way, it is possible to observe the electron decay directly in the time and momentum domain.

*Spin-integrated dynamics on  $Fe_3O_4$*

Our experiment has employed a mode-locked Ti:sapphire laser system, which operates

## Chapter 5: Results and Discussion

with 800nm near-IR light. We used this fundamental frequency (1.55eV) as the pump pulse and 3<sup>rd</sup> harmonic (4.65eV) as probe pulse. A translational stage introduces the variable delay between pump and probe pulses. The laser spot size on the sample is around 115  $\mu\text{m}$  and the fluence is 1  $\text{mJ}/\text{cm}^2$ . As introduced in chapter 2, the laser source can cause space charging effect,

A clear excitation of hot electrons is observed on the log scale EDC, see Fig.5.32

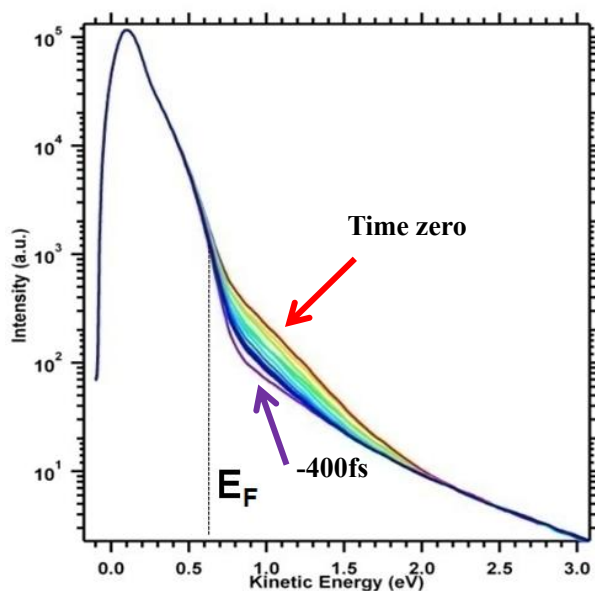


Fig.5.32 Time-resolved EDC from -400fs to 1.5ps

The high-energy tail (from 800meV to 3eV) is strongly dependent on the pump power and becomes negligible for 10 mW pump pulses in our case.

In a pump-probe configuration the  $\Delta\text{EDC}(t)$  is obtained by subtracting the unpumped EDC to each EDC measured at different time delay between the two beams. As shown in Fig.5.33, we can clearly see a loss of spectral weight below Fermi and an increase of photo-excited electrons on and above Fermi. The full mechanism at the origin of the electron below  $E_F$  is not clear yet. Interestingly the decay time is much longer than what would be expected for a Fe layer (few tens of fs). The dynamics is characterized by a fast (life time of excited states) and a slow relaxation time (phonon excitations) of the electrons. As discussed by Uwe Bovensiepen, in the 2PPE process, the excess energy is transferred to lattice and spin systems via electron-phonon scattering, and hot electron-spin wave scattering in magnetically ordered systems respectively. To be more specific, we find that a fast relaxation of the electronic system is observed in the first 200fs for three different kinetic energy regions, i.e. 0.25eV to 0.3eV (below  $E_F$ ), 0.6eV to 0.8eV (at  $E_F$ ) and 0.85eV to 1.1eV (above  $E_F$ ), which is shown in Fig.5.34 upper panel, middle panel and bottom panel respectively. The decay of electrons may occur on similar or separate timescales depending on material and optical excitation density.

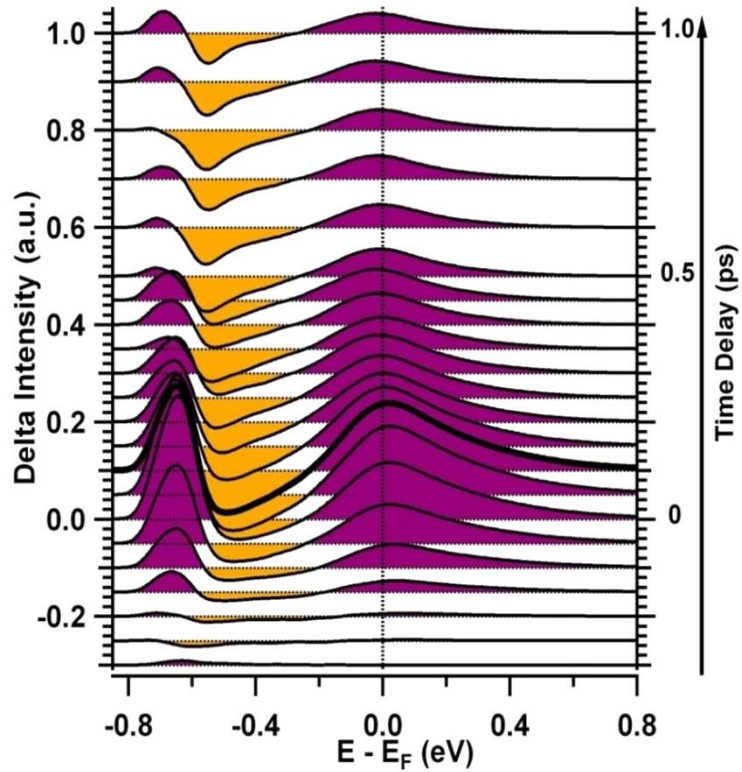


Fig.5.33 EDC dynamics  $\Delta EDC(t)$  in the time delay region -400fs to 1ps. Violet is positive which means the intensity of photoelectron increases and yellow is negative which means the intensity of photoelectron decrease.

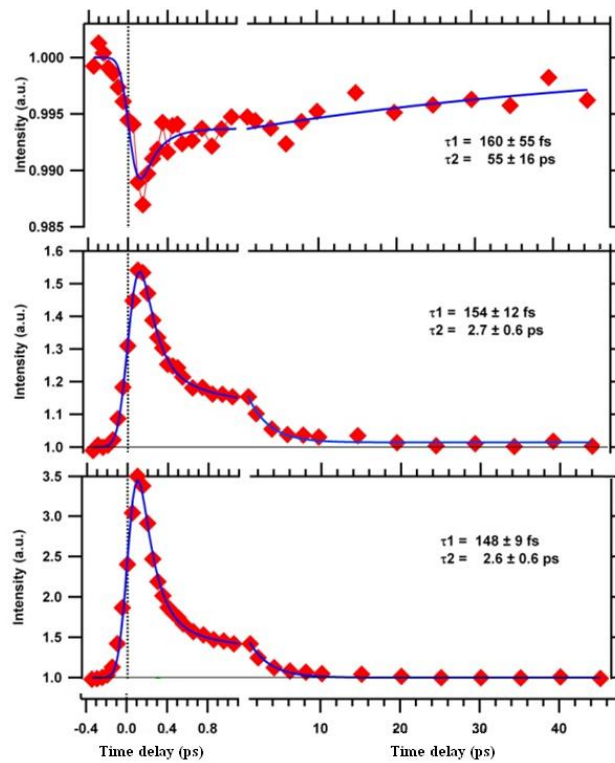


Fig.5.34 Relaxation of photoelectrons in the 2PPE pump-probe process. Upper panel: below  $E_F$  ( $E_B$  from -0.5 eV to -0.45 eV); Middle panel: around  $E_F$  ( $E_B$  from -0.05 eV to 0.05 eV); Bottom panel: above  $E_F$  ( $E_B$  from 0.1 eV and 0.35 eV)

Spin-polarized dynamics on  $Fe_3O_4$

We study further the dynamics of majority and minority spins individually. Negative polarization is obtained close to  $E_F$ . This corresponds to the GGA+U calculation which predicts a  $t_{2g}$  minority band crossing Fermi and a band gap in the majority spin band structure. Because of the polaron and three-body scattering effect in the photoemission process, there is also considerable intensity of majority spin at Fermi. As shown in Fig.5.35, a clear reduction of the spin polarization (absolute value) is observed close to Fermi (200meV) and no variation is detected at lower kinetic energy when the pump-probe process approaches “Time zero” (yellow curve) from negative time delay (-400fs, green curve). This reduction can be explained by the mechanism of 2PPE. The pump beam is 1.55eV, it can pump the electron from 1.55eV (binding energy) to the Fermi level, according to the GGA+U calculation, one majority spin band is located at around 1.4eV while from 0.8eV to 2eV is a band gap for minority spin. So it’s very reasonable that the 2PPE produces more majority than minority hot electron at Fermi which reduces the polarization at  $E_F$ .

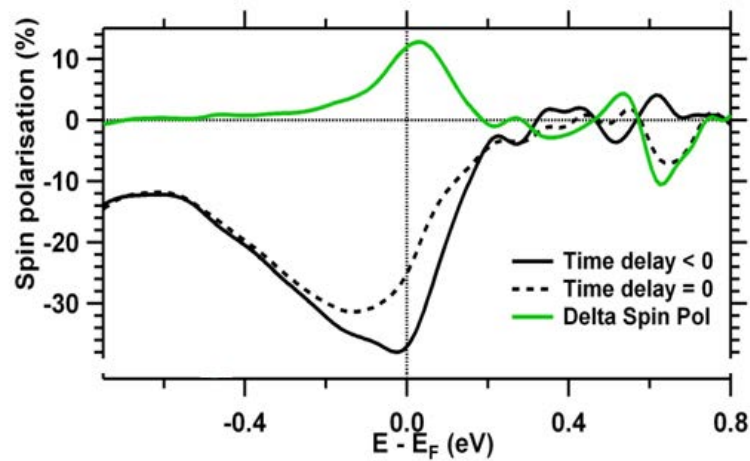


Fig.5.35 Time-resolved Spin polarization dynamic EDC. Dashed curve: time zero delay; solid curve: negative time delay, -400fs. Green curve: the spin polarization difference between time zero and negative time delay

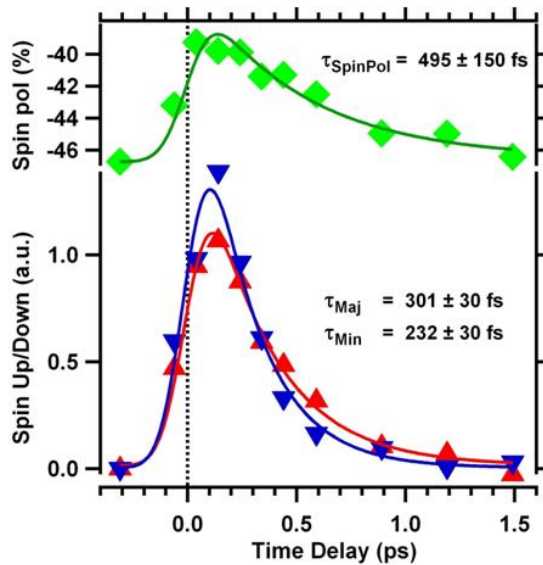


Fig.5.36 Upper panel: Relaxation of the spin polarization around Fermi level; Bottom panel: Relaxation of majority and minority spin respectively. Red presents relaxation of majority spin and blue represents relaxation of minority spin.

*Chapter 5: Results and Discussion*

If we track the electrons spin dynamic on very short time scale, we find that the spin polarization recovers on a longer time than the total intensity which indicates a spin dependent relaxation time of the electrons (Fig.5.36). By analyzing majority and minority spin intensity separately, we observe a slightly longer relaxation time for majority spins. The average life time measured here is much longer than in Fe and this should be attributed to the low DOS across Fermi and to the fact that the electron kinetic energy is very small.

## Conclusion:

Understanding the electronic structure of strongly correlated systems is always a difficult subject in solid state physics. The key to the development of spintronics is the identification of materials in which fully spin-polarized currents exist. Such a situation is met in ideal half-metallic ferromagnets that are metallic for electrons with one spin direction and have an energy gap at the Fermi energy for electrons of the opposite spin. Practical applications also require Curie temperatures higher than room temperature. Magnetite,  $\text{Fe}_3\text{O}_4$ , with a  $T_C$  of  $\sim 850$  K, has been predicted from band structure calculations to have a half-metallic character. But up to now any clear experimental evidence is lacking. The presented experimental studies fill this gap to some extent and report the low-energy electronic structure of thin films of  $\text{Fe}_3\text{O}_4(001)$  epitaxially grown on  $\text{MgO}(001)$ .

ARPES measurements close to  $E_F$  neither show a clear cut-off at  $E_F$  nor dispersion. The absence of spectral weight at  $E_F$  can be explained by strong electron-lattice coupling, along the lines of the interpretation of photoemission spectra of many transition metal oxides. In the case of  $\text{Fe}_3\text{O}_4$  the electron-lattice interaction, described in the model of small polarons, is so strong that the intensity of the quasiparticle is completely washed out. The overall behaviour of measured energy bands is in very good agreement with generalized gradient approximation plus U (GGA+U) calculations of the ground state electronic structure. Because at present the calculation of the photoemission process is hardly feasible for  $\text{Fe}_3\text{O}_4$ , we did a simulation of the spectra using a simple model. We used the free-electron approximation for the final states and the ground state data were convoluted by Lorentzian and Gaussian functions to account for the lifetime and electron-phonon coupling effects, respectively.

Fermi surface has been mapped as well and has been found to be in agreement with first principles band calculations. The measured Fermi surface plot is presented here in an unconventional way: as a function of  $k_z$ , representing  $k_\perp$  and showing bulk electronic properties (extracted from normal emission measurements) and  $k_y$  representing  $k_\parallel$  and showing both bulk and surface properties. Such a presentation gives the possibility to unravel differences between surface and bulk electronic structure. Both contributions give the same symmetries and periodicities.

Determination of electron spin polarization was the ultimate test of both the band calculations and our simulation of photoemission spectra. In our Spin-resolved ARPES experiments 4.65 and 6.20 eV photons were used and the electrons were collected at normal emission. In the first part, we report the highest polarization (-72%) ever reported in the

literature on the  $\text{Fe}_3\text{O}_4$  (001) surface. Our spin polarization measurements are consistent with the band-like description as obtained from the simulated spin-polarized spectra and the experiment.

In conclusion, three independent photoemission measurements have been performed on  $\text{Fe}_3\text{O}_4$ : band dispersion, Fermi surface mapping (both being revealed for the first time) and spin polarization. These three sets of photoemission data can be simulated starting from GGA+U bulk band structure calculations predicting  $\text{Fe}_3\text{O}_4$  to be a half-metal and taking into account the polaron and initial-state lifetime broadenings inherent to the photoemission process. This demonstrates that  $\text{Fe}_3\text{O}_4$  can be described within a band model and in particular that it is half-metallic.

## References

- [1] John Baez, Open Questions in Physics. Usenet Physics FAQ. University of California, Riverside. March 2006
- [2] M. N. Baibich, J. M. Broto, A. Fert et al, Giant Magnetoresistance of (001)Fe/(001)Cr Magnetic Supperlattices, PRL. **61**,2472 (1988)
- [3] G. Binasch, P. Grünberg, F. Saurenbach et al, Enhanced magnetoresistance in layered magnetic structures with antiferromagnetic interlayer exchange, PRB. **39**, 4828 (1989).
- [4] R. A. de Groot and F. M. Mueller, New Class of Materials: Half-Metallic Ferromagnets, Phys. Rev. Lett., **50**, 2024 (1983)
- [5] C. Kittel, Introduction to Solid State Physics, (1953)
- [6] F. Bloch. Z. Phys, **52**, 555, (1928)
- [7] H. J. Schulz, Fermi liquids and non-Fermi liquids, in "Proceedings of Les Houches Summer School LXI", p.533 (1995)
- [8] A.J. Schofield, Non Fermi liquids (1998)
- [9] J.H. deBoer and E.J.E. Verwey, Proc. Phys. Soc. London, **A**, 49, (1937)\
- [10] Kyle Michael Shen, thesis: Angle resolved photoemission spectroscopy studies of the Mott Insulator to superconductor evolution in  $\text{Ca}_{2-x}\text{Na}_x\text{CuOCl}_2$ . (2005)
- [11] K.E.H.M. Hassen and P.E. Mijnaerends, Positron-annihilation study of half-metallic ferromagnet NiMnSb: Theory, Phys. Rev. B. **34**, 5009 (1986)
- [12] K.E.H.M. Hassen, P.E. Mijnaerends and L.P.L.M. Rabou, Positron-annihilation study of half-metallic ferromagnet NiMnSb: Experiment, Phys. Rev. B. **42**,1533 (1990)
- [13] V. Yu. Irkhin and M. I. Katsnelson, Ground state and electron-magnon interaction in an itinerant ferromagnet: half-metallic ferromagnets, J. Phys.: Condens. Matter, **2**, 7151 (1990)
- [14] F. Bloch, Zur Theorie des Ferromagnetismus, Z. Physik, **61**, 206 (1930)
- [15] A. A. Knowlton and O. C. Clifford, The Heusler alloys, Trans. Faraday Soc., **8**, 195-206 (1912)
- [16] G.L. Zhao, J. Callaway and M. Hayashibara, Electronic structure of iron and cobalt pyrites, Phys. Rev. B. **48**,15781 (1993)
- [17] I.I. Mazin, Robust half metallicity in  $\text{Fe}_x\text{Co}_{1-x}\text{S}_2$ , Appl. Phys. Lett. **77**,3000 (2000)
- [18] L. Wang, K. Umemoto and R.M. Wentzcovitch et al,  $\text{Fe}_x\text{Co}_{1-x}\text{S}_2$ : A Tunable source of Highly spin-polarized Electrons, Phys. Rev. Lett. **94**, 056602 (2005)
- [19] C. Leighton, M. Manno and A. Cady et al, Composition controlled spin polarization in  $\text{Fe}_x\text{Co}_{1-x}\text{S}_2$  alloys, J. Phys.: Condens. Matter **19**, 315219 (2007)
- [20] J. J. Attema, G. A. de Wijs and R. A. de Groot, The continuing drama of the half-metal/semiconductor interface, J. Phys. D: Appl. Phys. **39**, 793 (2006)
- [21] Roman Kováčik\* and Claude Ederer, Correlation effects in p-electron magnets: Electronic structure of  $\text{RbO}_2$  from first principles, Phys. Rev. B, **80**, 140411 (2009)
- [22] H. van Leuken and R. A de Groot, Electronic structure of the chromium dioxide (001) surface, Phys. Rev. B. **51**, 7176 (1995)
- [23] K.P. Kamper, W. Schmitt and G. Guntherodt,  $\text{CrO}_2$ -A New Half-Metallic Ferromagnet? Phys. Rev. Lett. **59**, 2788 (1987)
- [24] A. M. Bratkovsky, Tunneling of electrons in conventional and half-metallic systems:

- Towards very large magnetoresistance, Phys. Rev. B 56, 2344 (1997)
- [25] Y. Ji, G. J. Strijkers and F. Y. Yang et al, Determination of the Spin Polarization of Half-Metallic CrO<sub>2</sub> by Point Contact Andreev Reflection, Phys. Rev. Lett. **86**, 5585 (2001)
- [26] Yu. S. Dedkov, M. Fonin, C. Konig et al, Room-temperature observation of high-spin polarization of epitaxial CrO<sub>2</sub> (100) island film at the Fermi energy, App. Phys. Lett. **80**, 22, 4181 (2002)
- [27] A. Yanase and K. Siratori, Band structure in the High Temperature Phase of Fe<sub>3</sub>O<sub>4</sub>, J. Phys. Soc. Jpn. 53 pp. 312-317 (1984)
- [28] V. Yu Irkhin and M. I. Katsnelson, J. Phys. C: Solid State Phys. **18**, 4173 (1985)
- [29] L. Landau, The theory of a Fermi liquid, Soviet Physics JETP, **3**, 920 (1957)
- [30] V. Yu Irkhin and M. I. Katsnelson, Usp. Fiz. Nauk, **164**, 705 (1994)
- [31] L. Chioncel, E. Arrigoni, M. I. Katsnelson et al, Majority-spin nonquasiparticle states in half-metallic ferrimagnet Mn<sub>2</sub>VAl, Phys. Rev. B, **79**, 125123 (2009)
- [32] V. Yu. Irkhin, M. I. Katsnelson and A. I. Lichtenstein, Nonquasiparticle states in half-metallic ferromagnets, Lecture Notes in Physics, **678**, 217-243 (2005)
- [33] P.A. Dowben and R. Skomski, Finite-temperature spin polarization in half-metallic ferromagnets, J. Appl. Phys. **93**, 7948 (2003)
- [34] Y. J. Kim, Y. Gao and S. A. Chambers, Selective growth and characterization of pure, epitaxial α-Fe<sub>2</sub>O<sub>3</sub>(0001) and Fe<sub>3</sub>O<sub>4</sub>(001) films by plasma-assisted molecular beam epitaxy, Surface Science A, **371**, 358-370 (1997)
- [35] R. Moriya, Spin Fluctuation in Itinerant Electron Magnetism, Berlin: Springer (1985)
- [36] M. I. Katsnelson, V. Yu. Irkhin, L. Chioncel et al, Half-metallic ferromagnets : From band structure to many body effects, cond-mat.mtrl-sci, 6 Nov. (2007)
- [37] G. Baym and L. P. Kadanoff, Conservation Laws and Correlation Functions, Phys. Rev., **124**, 287 (1961)
- [38] J. M. Luttinger and J. C. Ward, Ground-State Energy of a Many Fermion System. II, Phys. Rev. **118**, 1417 (1960)
- [39] W. Kohn and L. J. Sham, Self-Consistent Equations In Exchange and Correlation Effects, Phys. Rev. **140**, A1133 (1965)
- [40] A. I. Lichtenstein and M. I. Katsnelson, Ab initio calculation of quasiparticle band structure in correlated systems: LDA++ approach, Phys. Rev. B, **57(12)**, 6884 (1998)
- [41] G. Mariotto, S. Murphy and I. V. Shvets, Charge ordering on the surface of Fe<sub>3</sub>O<sub>4</sub> (001), Phys. Rev. B, **66**, 245426 (2002)
- [42] M. L. Rudee, David J. Smith and D. T. Margulies, Evidence for charge ordering at room temperature in Fe<sub>3</sub>O<sub>4</sub>, Phys. Rev. B, **59**, R11633 (1999)
- [43] R. Pentcheva, W. Moritz, J. Rundgren et al, A combined DFT/LEED-approach for complex oxide surface structure determination: Fe<sub>3</sub>O<sub>4</sub>(001), Surface Science **602** 1299-1305 (2008)
- [44] V. N. Antonov, B. N. Harmon and V. P. Antropov, Electronic structure and magneto-optical Kerr effect of Fe<sub>3</sub>O<sub>4</sub> and Mg<sup>2+</sup>- or Al<sup>3+</sup>-substituted Fe<sub>3</sub>O<sub>4</sub>, Phys. Rev. B, **64**, 134410 (2001)
- [45] S. K. Arora, Han-Chun Wu, R. J. Choudhary et al, Giant magnetic moment in epitaxial Fe<sub>3</sub>O<sub>4</sub> thin films on MgO(100), Phys. Rev. B, **77**, 134443 (2008)
- [46] V. N. Petrov and A. B. Ustinov, Magnetic Properties of Fe<sub>3</sub>O<sub>4</sub> Surface, Journal of Surface

- Investigation: X-ray, Synchrotron and Neutron Techniques, **4**, Number 3, 395-400 (2010)
- [47] P. Kuiper, B.G. Searle, L.-C. Duda et al, Fe  $L_{2,3}$  linear and circular magnetic dichroism of  $Fe_3O_4$ , Journal of Electron Spectroscopy and Related Phenomena, **86**, 107-113 (1997)
- [48] S. A. Chambers, S. Thevuthasan and S. A. Joyce, Surface structure of MBE-grown  $Fe_3O_4(001)$  by X-ray photoelectron diffraction and scanning tunneling microscopy, Surface Science Letter, **450**, L273-L279 (2000)
- [49] H. -J. Kim, J. -H. Park and E. Vescovo,  $Fe_3O_4(111)/Fe(110)$  magnetic bilayer: Electronic and magnetic properties at the surface and interface, Phys. Rev. B, **61**, 15288 (2000)
- [50] D. J. Huang, C. F. Chang, H. -T. Jeng et al, Spin and Orbital Magnetic Moments of  $Fe_3O_4$ , Phys. Rev. Lett. **93**, 077204 (2004)
- [51] Y. X. Lu, J. S. Claydon and Y. B. Xu, Epitaxial growth and magnetic properties of half-metallic  $Fe_3O_4$  on GaAs(100), Phys. Rev. B, **70**, 233304 (2004)
- [52] A. Yanase and K. Siratori, Band structure in the High Temperature Phase of  $Fe_3O_4$ , J. Phys. Soc. Jpn. **53** pp. 312-317 (1984)
- [53] Z. Zhang and S. Satpathy, Electron states, magnetism, and the Verwey transition in magnetite, Phys. Rev. B, **44**, 13319 (1991)
- [54] V. N. Antonov, B. N. Harmon and V. P. Antropov, Electronic structure and magneto-optical Kerr effect of  $Fe_3O_4$  and  $Mg^{2+}$ - or  $Al^{3+}$ -substituted  $Fe_3O_4$ , Phys. Rev. B, **64**, 134410 (2001)
- [55] A. Yanase and N. Hamada, Electronic Structure in High Temperature Phase of  $Fe_3O_4$ , J. Phys. Soc. Jpn. **68**, 1607-1613 (1999)
- [56] J. P. Wright, J. P. Attfield and P. G. Radaelli, Long Range Charge Ordering in Magnetite Below the Verwey Transition, Phys. Rev. Lett. **87**, 266401 (2001)
- [57] I. Leonov, A. N. Yaresko, V. N. Antonov et al, Charge and Orbital Order in  $Fe_3O_4$ , Phys. Rev. Lett. **93**, 146404 (2004)
- [58] Robert J. Lad and Victor E. Henrich, Photoemission study of the valence band electronic structure in  $Fe_xO$ ,  $Fe_3O_4$  and  $\alpha-Fe_2O_3$  single crystals, Phys. Rev. B, **39**, 13478 (1989)
- [59] Y. Q. Cai, M. Ritter, W. Weiss et al, Valence band structure of epitaxially grown  $Fe_3O_4(111)$  films, Phys. Rev. B, **58**, 5043 (1998)
- [60] Yuriy Dedkov, thesis: Spin-resolved photoelectron spectroscopy of oxidic half-metallic ferromagnets and oxide/ferromagnet interfaces (2004)
- [61] R. J. Soulen Jr., J. M. Byers et al, Measuring the Spin Polarization of a Metal with a Superconducting Point Contact, Science, **282**, 5386 (1998)
- [62] M. J. M. de Jong and C. W. J. Beenakker, Andreev Reflection in Ferromagnet-Superconductor Junctions, Phys. Rev. Lett., **74**, 1657 (1995)
- [63] S. F. Alvarado, W. Eib, F. Meier et al, Observation of Spin-Polarized Electron Levels in Ferrites, Phys. Rev. Lett. **34**, 319 (1975)
- [64] Yu. S. Dedkov, U. Ruediger and G. Guntherodt, Evidence for the half-metallic ferromagnetic state of  $Fe_3O_4$  by spin resolved photoelectron spectroscopy, Phys. Rev. B, **65**, 064417 (2002)
- [65] D. J. Huang, C. F. Chang, J. Chen et al, Spin-resolved photoemission studies of epitaxial  $Fe_3O_4(100)$  thin films, J. Magn. Magn. Mater. **239** (2002)
- [66] M. Fonin, Yu. S. Dedkov, J. Mayer et al, Preparation, structure, and electronic properties

- of Fe<sub>3</sub>O<sub>4</sub> films on the Fe(110)/Mo(110)/Al<sub>2</sub>O<sub>3</sub>(1120) substrate, *Phys. Rev. B*, **68**, 045414 (2003)
- [67] M. Fonin, R. Pentcheva, Yu. S. Dedkov et al, Surface electronic structure of the Fe<sub>3</sub>O<sub>4</sub> (100): Evidence of a half-metal to metal transition, *Phys. Rev. B*, **72**, 104436 (2005)
- [68] M. Fonin, Yu. S. Dedkov, R. Pentcheva et al, Magnetite: a search for the half-metallic state, *J. Phys.: Condens. Matter* **19** 315217 (2007)
- [69] J. G. Tobin, S. A. Morton, S. W. Yu et al, Spin resolved photoelectron spectroscopy of Fe<sub>3</sub>O<sub>4</sub>: the case against half-metallicity, *J. Phys.: Condens. Matter* **19**, 315218 (2007)
- [70] J. R. Cullen and E. Callen, Collective Electron Theory of the Metal-semiconductor Transition in Magnetite, *J. Appl. Phys.* **41**, 879 (1970)
- [71] B. K. Chakraverty, Charge ordering in Fe<sub>3</sub>O<sub>4</sub>, Ti<sub>4</sub>O<sub>7</sub> and bipolarons, *Philosophical Magazine Part B*, Volume 42, Issue **3**, 473-478 (1980)
- [72] Y. Yamada, Molecular polarons and valence fluctuations in Fe<sub>3</sub>O<sub>4</sub>, *Philosophical Magazine Part B*, Volume 42, Issue **3**, page 377-385 (1980)
- [73] A. Chainani, T. Yokoya, T. Morimoto et al, High-resolution photoemission spectroscopy of the Verwey transition in Fe<sub>3</sub>O<sub>4</sub>, *Phys. Rev. B*, **51**, 17976 (1995)
- [74] Robert J. Lad and Victor E. Henrich, Photoemission study of the valence band electronic structure in Fe<sub>x</sub>O, Fe<sub>3</sub>O<sub>4</sub> and α-Fe<sub>2</sub>O<sub>3</sub> single crystals, *Phys. Rev. B*, **39**, 13478 (1989)
- [75] J. -H. Park, L. H. Tjeng, J. W. Allen et al, Single-particle gap above the Verwey transition in Fe<sub>3</sub>O<sub>4</sub>, *Phys. Rev. B*, **55**, 12813 (1997)
- [76] K. Jordan, A. Cazacu, G. Manai et al, Scanning tunneling spectroscopy study of the electronic structure of Fe<sub>3</sub>O<sub>4</sub> surfaces, *Phys. Rev. B*, **74**, 085416 (2006)
- [77] D. Schrupp, M. Sing, M. Tsunekawa et al, High energy photoemission on Fe<sub>3</sub>O<sub>4</sub>: Small polaron physic and the Verwey transition, *Europhys. Lett.*, **70**, 789 (2004)
- [78] Masato Kimura, Hidenori Fujiwara, Akira Sekiyama et al, Polaronic behavior of photoelectron spectra of Fe<sub>3</sub>O<sub>4</sub> revealed by both hard X-ray and extremely low energy photons, *J. Phys. Soc. Jpn.* **79**, 064710-1-5 (2010)
- [79] C. Cacho, V. R. Dhanak, L. B. Jones et al, Spin-resolved two-photon photoemission on Fe<sub>77</sub>B<sub>16</sub>Si<sub>5</sub> alloy, *Journal of Electron Spectroscopy and Related Phenomena*, 169, 62 (2009)
- [80] Stefania Pizzini, X-ray Magnetic Circular Dichroism (XMCD): basic concepts and theory for rare earths and 3d metals, *Ecole Franco-Roumaine: Magnétisme des systèmes nanoscopiques et structures hybrides*. (2003)
- [81] J. Stohr, Exploring the microscopic origin of magnetic anisotropies with X-ray magnetic circular dichroism (XMCD) spectroscopy, *J. M. M. M.*, **200**, 470 (1999)
- [82] B.T. Thole, P. Carra, F. Sette et al, X-ray circular dichroism as a probe of orbital magnetization, *Phys. Rev. Lett.*, **68**, 1943 (1992)
- [83] C. Cacho, S. Vlaic, M. Malvestuto et al, Absolute spin calibration of an electron spin polarimeter by spin-resolved photoemission from the Au (111) surface states, *Rev. Sci. Instrum.* **80(4)**, 043904 (2009)
- [84] N. M. Buckanie, J. Goehre, P. Zhou et al, Space charge effect in photoemission electron microscopy using amplified femtosecond laser pulses, *J. Phys.: Condens. Matter*, **21** 314003 (2009)
- [85] Timothy J. Giese and Darrin M. York, Density-functional expansion methods: Evaluation of LDA, GGA and meta-GGA functionals and different integral approximations, *J. Che. Phys.*,

- 133**, 244107 (2010)
- [86] John P. Perdew, Kieron Burke, Matthias Ernzerhof, Generalized Gradient Approximation Made Simple, *Phys. Rev. Lett.*, **77**, 18 (1996)
- [87] Arma Peles, GGA+U method from first principles: application to reduction-oxidation properties in ceria-based oxides, *J. Mater. Sci.*, Springer (2012)
- [88] V. N. Strocov, Intrinsic accuracy in 3-dimensional photoemission band mapping, *J. E. S. R. Ph.* **130**, 65 (2003)
- [89] C. T. Chen, Y. U. Idzerda, H. -J. Lin et al, Experimental Confirmation of the X-Ray Magnetic Circular Dichroism Sum Rules for Iron and Cobalt, *Phys. Rev. Lett.*, **75**, 152-155 (1995)
- [90] P. Szymanski, S. Garrett-Roe and C. B. Harris, Time- and angle resolved two-photon photoemission studies of electron localization and solvation in interfaces, *Surf. Sci.* **78**, 1-39 (2005)
- [91] P. Thiry. La photoémission angulaire dans les solides: structure électronique de volume et de surface du cuivre. PhD thesis, Université de Paris-Sud (1981)
- [92] Eric R. Ylvisaker, Warren E. Pickett and Klaus Koepnik, Anisotropy and magnetism in the LSDA+U method, *Phys. Rev. B*, **79**, 035103 (2009)
- [93] A. I. Liechtenstein, V. I. Anisimov and J. Zaanen, Density-functional theory and strong interactions: Orbital ordering in Mott-Hubbard insulators, *Phys. Rev. B*, **52**, R5467 (1995)
- [94] A. N. Andriotis, R. Michael Sheetz and M. Menon, LSDA+U method: A calculation of the U values at the Hartree-Fock level of approximation, *Phys. Rev. B*, **81**, 245103 (2010)
- [95] A. S. Alexandrov and J. Ranninger, Polaronic effects in the photoemission spectra of strongly coupled electron-phonon systems, *Phys. Rev. B*, **45**, 13109 (1992)
- [96] Stephen Elliott, *The Physics and Chemistry of Solids*
- [97] H. Wadati, T. Yoshida, A. Chikamatsu et al, Angle-resolved photoemission spectroscopy of perovskite-type transition-metal oxides and their analyses using tight-binding band structure, *Phase Transitions* **79**, 617 (2008)
- [98] J. Chaloupka and G. Khaliullin, Spin polaron theory for the photoemission spectra of layered cobaltates, *Phys. Rev. Lett.*, **99**, 256406 (2007)
- [99] N. V. Smith, Higher-Derivative Photoemission Spectra and the Relativistic Band Structure of Gold, *Phys. Rev. B*, **5**, 1192 (1972)
- [100] J. E. Ortega and F. J. Himpsel, *Very High Resolution Electron Spectroscopy* (ed. by S. Hüfner), *Lectures Notes in Physics* 715, 147 (2007)
- [101] M. Ogawa, P. M. Sheverdyaeva, P. Moras et al., Electronic structure study of ultrathin Ag (111) films modified by a Si (111) substrate and  $\sqrt{3} \times \sqrt{3}$ -Ag<sub>2</sub>Bi surface, *J. Phys.: Condens. Matter*, **24**, 115501 (2012).
- [102] K. M. Shen, F. Ronning, W. Meevasana et al, Angle-resolved photoemission studies fo lattice polaron formation in the cuprate Ca<sub>2</sub>CuO<sub>2</sub>Cl<sub>2</sub>, *Phys. Rev. B*, **75**, 075115 (2007)
- [103] Vasili Perebeinos and Philip B. Allen, Franck-Condon-Broadened Angle-Resolved Photoemission Spectra Predicted in LaMnO<sub>3</sub>, *Phys. Rev. Lett.*, **85**, 5178 (2000)
- [104] S. Monastera, F. Manghi, C. A. Rozzi et al, Quenching of majority-channel quasiparticle excitation in cobalt, *Phys. Rev. Lett.*, **88**, 236402 (2002)
- [105] Uwe Bovensiepen, Coherent and incoherent excitation of the Gd(0001) surface on ultrafast timescales, *J. Phys.: Condens. Matter* **19**, 083201 (2007)

- [106] G. M. Muller, J. Walowski, M. Djordjevic et al, Spin polarization in half-metals probed by femtosecond spin excitation, *Nature materials*, **k**, 56 (2009)
- [107] S. A. Krasnikov, A. S. Vinogradov, K. -H. Hallmeier et al, Oxidation effects in epitaxial  $\text{Fe}_3\text{O}_4$  layers on MgO and  $\text{MgAl}_2\text{O}_4$  substrates studied by X-ray absorption, fluorescence and photoemission, *Mater. Sci. En. B*, **109**, 207 (2004)
- [108] C. L. Chang, G. Chern, Y. R. Chean, Growth and structural studies of  $\text{Fe}_3\text{O}_4/\text{MgO}$  superlattice, *Appl. Surf. Sci.* **161**, 448 (2000)

---

Publication:

Magnetite Half-Metallicity Uncovered by Angle- and Spin- Resolved Photoemission

W. Wang, J.-M. Mariot, M.C. Richer, O. Heckmann, W. Ndiaye, P. De Padova, A. Taleb-Ibrahimi, P. Le Fevre, F. Bertran, F. Bondino, E. Magnano, J. Krempasky, P. Blaha, C. Cacho, F. Parmigiani, and K. Hricovini

Submitted in Physical Review B

---

Poster:

Electron dynamics in Fe<sub>3</sub>O<sub>4</sub>(100)/MgO(100) thin layers investigated by spin-resolved photoemission

Weimin Wang, C. M. Cacho, O. Heckmann, M. C. Richter, J. Krempasky,

W. Ndiaye, P. De Padova, J.-M. Mariot, F. Parmigiani and K. Hricovini

18th International Vacuum Congress, Beijing, China, August 2010

(Best poster award)

t<sub>2g</sub> band dispersion on the (100) surface of magnetite

W. Wang, M. C. Richter, O. Heckmann, W.Ndiaye, J.-M. Mariot, P. De Padova, A.

Taleb-Ibrahimi, P. Le Fèvre, F. Bertran, and K. Hricovini

SOLEIL, Users Meeting, January 2011

Spin and Angle- Resolved Photoemission on LSMO and magnetite

K. Hricovini , , J.-M. Mariot, M. C. Richter, O. Heckmann, W. Ndiaye, P. De Padova, F. Bondino, E. Magnano, W. Wang J. Krempask'y, C. Cacho, F. Parmigiani, and

Workshop "Probing Magnetic Dynamics with Ultrashort Coherent X-Ray Pulses" (Trieste), December 16-18, 2009:

Dynamics in Fe<sub>3</sub>O<sub>4</sub>(100)/MgO(100) thin layers

M. C. Richter, Weimin Wang, C. M. Cacho, O. Heckmann, J. Krempasky,

W. Ndiaye, P. De Padova, J.-M. Mariot, F. Parmigiani and K. Hricovini

NANO2010, Rome, Italy, Set. 2010

ARPES studies of Bi/InAs(111) interfaces

K. Hricovini, M.C.Richter, O.Heckmann, W. Wang, T. Balasubramanian, M.

Leandersson, C. Cacho, J.-M. Mariot

E-MRS, Warsaw, Poland, Sept 2011

Angle- resolved photoemission on Mn<sub>5</sub>Ge<sub>3</sub>/Ge(111) thin films

W.Ndiaye, M.C.Richter, O.Heckmann, W. Wang, P. De Padova, J.-M. Mariot, A.

Taleb-Ibrahimi, P. Le Fèvre, F. Bertran, T. Balasubramanian, M. Leandersson, C. M. Cacho, K. Hricovini

EcoSS28, Wrocław, Poland, 28 08 - 02 09 2011

Magnetic moment of thin Fe<sub>3</sub>O<sub>4</sub> films grown on MgO(100) and BaTiO<sub>3</sub>(100)

O. HECKMANN, N. BARRETT, J. RAULT, M.-C. RICHTER, W. WANG, F. BONDINO, M. MALVESTUTO, E. MAGNANO, F. PARMIGIANI, K. HRICOVINI

EcoSS28, Wrocław, Poland, 28 08 - 02 09 2011

Angle and spin-resolved photoemission on Mn<sub>5</sub>Ge<sub>3</sub>/Ge(111)

W.Ndiaye, M.C.Richter, O.Heckmann, W. Wang, P. De Padova, J.-M. Mariot, A. Taleb-Ibrahimi, P. Le Fèvre, F. Bertran and K. Hricovini

SOLEIL, Users Meeting, January 2011

## APPENDIX A

### *Fermi Golden Rule and intensity measured in ARPES*

The Hamiltonian of one electron in a system can be described by a potential  $V(\mathbf{r})$  and a applied external electromagnetic field:

$$H = \frac{1}{2m} \left( \vec{p} - \frac{e}{c} \vec{A}(\vec{r}) \right)^2 + V(\vec{r}) = \frac{p^2}{2m} + V(\vec{r}) - \frac{e}{2mc} \left| \vec{A}(\vec{r}) \cdot \vec{p} + \vec{p} \cdot \vec{A}(\vec{r}) \right| + \frac{e^2}{2mc^2} \left| \vec{A}(\vec{r}) \right|^2$$

Where  $\mathbf{A}(\mathbf{r})$  is the vector potential associated with the field. Splitting the Hamiltonian into two terms ( $H = H_0 + V_I$ ), such that  $V_I$  describes the excitation:

$$H_0 = \frac{p^2}{2m} + V(\vec{r})$$

$$V_I = -\frac{e}{2mc} \left| \vec{A}(\vec{r}) \cdot \vec{p} + \vec{p} \cdot \vec{A}(\vec{r}) \right| + \frac{e^2}{2mc^2} \left| \vec{A}(\vec{r}) \right|^2$$

For low intensities of the external field, first order perturbation theory can be used to study the interaction between the electromagnetic radiation and the system. Thus, applying the Fermi Golden Rule to calculate the photocurrent, we obtain:

$$I(\varepsilon_f) = \left| M_{i,f} \right|^2 = \left| \langle \Psi_f | V_I | \Psi_i \rangle \right|^2$$

where the one-electron wave function  $\psi_i$  and  $\psi_f$  are eigen-functions of the Hamiltonian  $H_0$ , and the final wave function  $\psi_f$  behaves as an outgoing wave at infinity. The flexibility introduced by the gauge choice in the theory of electrodynamics facilitates the calculation of the matrix element. A common choice is to work in the Coulomb gauge, in which  $\nabla \cdot \mathbf{A}(\mathbf{r}) = 0$ , and consequently:

$$(\vec{A}(\vec{r}) \cdot \vec{p} - \vec{p} \cdot \vec{A}(\vec{r})) = i\hbar \nabla \cdot \vec{A}(\vec{r}) = 0$$

The interaction potential  $V_I$  can thus be expressed as:

$$V_I = -\frac{e}{mc} \left| \vec{A}(\vec{r}) \cdot \vec{p} \right| + \frac{e^2}{2mc^2} \left| \vec{A}(\vec{r}) \right|^2$$

So far, the most important approximations introduced in the theoretical formalism are the restriction to a one-electron picture, and the use of only first-order perturbation theory to calculate the interaction between the incident radiation and the system. The latter approximation is equivalent to neglecting terms of order  $\sim |A|^2$  in the calculation of the photocurrent. In order to be consistent with this approximation, the term of order  $\sim |A|^2$  in the interaction potential  $V_I$  is omitted as well. This approximation remains valid provided that the flux of incident photons is relatively low. For higher intensities of the external field these terms cannot be neglected and the theoretical formalism becomes more intricate. The matrix element  $M_{i,f}$  after keeping only the lowest-order terms can be written as:

$$M_{i,f} = \langle \Psi_f | V_I | \Psi_i \rangle = -\frac{e}{mc} \langle \Psi_f | \vec{A}(\vec{r}) \cdot \vec{p} | \Psi_i \rangle = \frac{i e \hbar}{mc} \langle \Psi_f | \vec{A}(\vec{r}) \cdot \vec{\nabla} | \Psi_i \rangle$$

where  $\mathbf{p}$  is replaced by  $-i\hbar \nabla$ . This way of writing the matrix element has been usually called in the literature the velocity form of the matrix element.

For strongly correlated system, there is a challenging problem of many-body physics inside. Considering electron-electron, electron-phonon and electron magnon interaction, the photoemission intensity measured can be written as:

$$I(\epsilon_f) \sim |M_{i,f}| \times \mathbf{A}(\mathbf{k}_i, E) \times \delta(\mathbf{k}_i - \mathbf{k}_f + \mathbf{G}) \times \delta(\epsilon_f + E_f^0 + E - E_i - \hbar\nu)$$

The two  $\delta$ -functions represent energy and momentum conservation. In a one electron picture where excitations of the many-body system are neglected ( $E = 0$ ), the total-energy difference  $E_f^0 - E_i$  equals to the binding energy. The second  $\delta$ -function connects the wave vectors  $\mathbf{k}_i$  and  $\mathbf{k}_f$ : In the case of itinerant states in crystalline solids, it is conserved in the photoemission process up to a reciprocal lattice vector  $\mathbf{G}$ , because the photon momentum can usually be neglected in a typical ARPES experiment. A complication arises due to the fact that the photoelectron is measured in vacuum, i.e. it left the potential range of the sample. The detection angles  $\theta_m$  and  $\phi_m$ , together with a kinetic energy value  $\epsilon_f$  define a wave vector  $\mathbf{k}$  of a free electron in vacuum:

$$\vec{k} = \frac{\sqrt{2m\epsilon_f}}{\hbar} \times (\sin \theta_m \cos \phi_m, \sin \theta_m \sin \phi_m, \cos \theta)$$

where  $m$  is the electron mass. The crystal periodicity parallel to the surface ensures that the wave vector components parallel to the surface plane are conserved:  $\mathbf{k}_{//} = \mathbf{k}_{f, //} + \mathbf{g}$ . In the direction perpendicular to the surface, the periodicity of the crystal lattice is truncated abruptly by the surface potential step, where the average potential rises from the inner potential  $-V_0$  in the solid to zero in vacuum. In free-electron final state approximation, the photoelectron state in the solid is treated like a single plane wave with vector:

$$\vec{k}_f = \frac{\sqrt{2m(\epsilon_f + V_0)}}{\hbar} \times (\sin \theta_m \cos \phi_m, \sin \theta_m \sin \phi_m, \cos \theta)$$

This may seem like a crude approximation for a photoelectron propagating through a periodic potential, but it has nevertheless proven to be quite successful.

## APPENDIX B

### *Three step model VS One step model*

The three-step model dates back to Berglund and Spicer on angle resolved photoemission from solids. It is a purely phenomenological approach, which has nonetheless proved to be quite successful. The photocurrent is decomposed into three separate factors: the probability of excitation in the bulk solid; the probability of scattering of the excited electron on its path to the surface by the atoms constituting the solid, and the probability of transmission through the surface for its final acceptance in the detector. The essential point is to calculate separate parts which are easily accessible if they do not interfere with each other. In our case, valence level spectroscopy is the goal, then the focus of attention is on the excitation process from an occupied band state and the photocurrent shows the energy levels at specific directions which are identified with the value (i.e. the electron momentum in the bulk). The two remaining factors, scattering and transmission, are considered to be less important: they may even be set to unity by neglecting those effects. By contrast, photoelectron diffraction might be very important, as for instance in core level spectroscopy: the dependence of the occupied states is trivial but the scattering by bulk and surface determines the angle variation of the photocurrent. Then, the first factor, excitation, becomes rather unimportant whereas the other two dominate the interpretation.

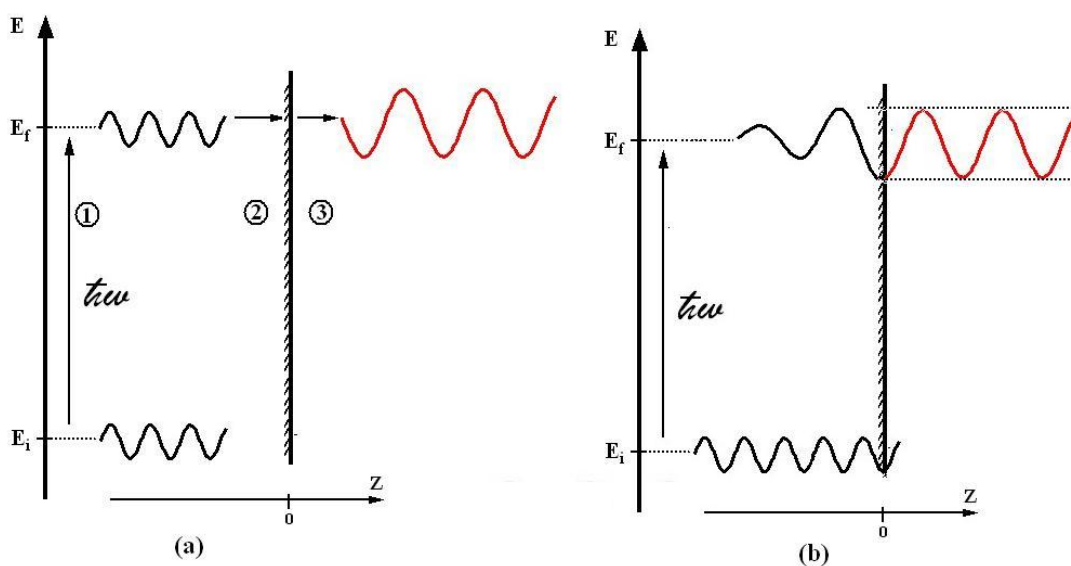


Fig.A1 Illustration of the three step (a) and one step (b) model in PES. The three step model consists of (1) photo-excitation of an electron; (2) its travel to the surface and (3) its transmission through the surface into the vacuum; In the one step model, a Bloch wave electron is excited into a wave that propagates freely in the vacuum but decays away from the surface into the solid

The three step model and its relation to the correct one-step model are sketched in Fig.A1. In the one-step model, one considers the excitation from an initial state into a damped final state near the surface, the damping taking care of the short mean free path of the electrons in the solid. Nowadays, state-of-the-art calculations of photocurrents use the one-step model, even though some valuable short cuts exist. The incorporation of “true” final states which correctly describe the scattering and propagation near and outside a surface is required by the physical situation of

accepting the excited electron in the detector at infinite times away from the sample: this is the essential ingredient of the one-step model. The model exists at several levels of sophistication, depending on the extent to which many-body effects are taken into account. Originally, the one-step model was designed as a one-particle theory applying the Fermi Golden Rule for one-particle states. The many-body formulation according to the considerations in principle should use correct final states as well, and thus fits into the concept of the one-step model.

## APPENDIX C

### *Effective electron mass*

In solid state physics, a particle's effective mass is the mass it seems to carry in the semi-classical model of transport in a crystal. It can be shown that electrons and holes in a crystal respond to electric and magnetic fields almost as if they were particles with a mass dependence in their direction of travel, an effective mass tensor. In a simplified picture that ignores crystal anisotropies, they behave as free particles in a vacuum, but with a different mass.

When an electron is moving inside a solid material, the force between other atoms will affect its movement and it will not be described by Newton's law. So we introduce the concept of effective mass to describe the movement of electron in Newton's law. The effective mass can be negative or different due to circumstances.

Effective mass is defined by analogy with Newton's second law  $F = ma$ . Using quantum mechanics it can be shown that for an electron in an external electric field  $E$ , the acceleration  $a_\ell$  along coordinate direction  $\ell$  is:

$$a_\ell = \frac{1}{\hbar^2} \sum_m \frac{\partial^2 \varepsilon(\vec{k})}{\partial k_\ell \partial k_m} qE_m$$

For a free particle, the dispersion relation is a quadratic, and so the effective mass would be constant (and equal to the real mass). In a crystal, the situation is far more complex. The dispersion relation is not even approximately quadratic, in the large scale. However, wherever a minimum occurs in the dispersion relation, the minimum can be approximated by a quadratic curve in the small region around that minimum.

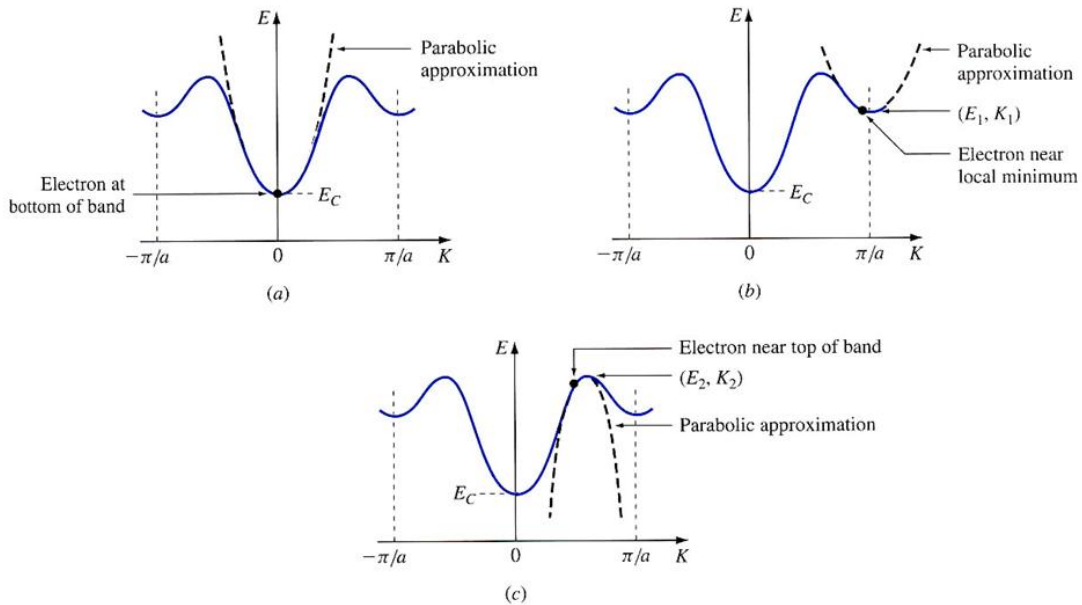


Fig. A2 The dispersion relation for (a) an electron at the bottom of the conduction band at  $k=0$ , where effective mass equals to the real mass; (b) an electron in a local minimum, where it has a different effective mass. (c) an electron far away from a minimum, where it has a negative effective mass.

A simplification can be made, however, for electrons which have energy close to a minimum,

and where the effective mass is the same in all directions, the mass can be approximated as a scalar  $m^*$  :

$$m^* = \hbar^2 \cdot \left[ \frac{d^2 \epsilon}{dk^2} \right]^{-1}$$

In energy regions far away from a minimum, effective mass can be negative or even approach infinity. Effective mass, being generally dependent on direction (with respect to the crystal axes), is a tensor. However, for many calculations the various directions can be averaged out.

# Abstract:

Magnetite ( $\text{Fe}_3\text{O}_4$ ) is a promising candidate for application in spintronic devices. This ferrimagnet with a high Curie temperature has been theoretically predicted to be a half-metal with a conductive minority-spin ( $\downarrow$ ) channel and a semiconductive majority-spin ( $\uparrow$ ) channel, resulting in 100 % spin polarization at the Fermi level. But up to now, any clear experimental evidence is lacking.

This thesis presents spin- and angle-resolved photoemission studies on the magnetic and electronic structure of  $\text{Fe}_3\text{O}_4$  (001) epitaxially grown on MgO (001). A band structure calculation using generalized gradient approximation plus U (GGA+U) to the density functional theory (DFT) is proposed to explain the experimental results.

Although the PES intensity at Fermi level is very low because of the role played by polarons, a dispersion of the Fe 3d- $t_{2g}$  states is observed. The overall behaviour of these bands is in good agreement with the calculation of ground state electronic structure. In order to simulate the spectra, we used the free electron approximation for the final states, ignoring the matrix elements. Calculated ground state data are convoluted by Lorentzian and Gaussian functions to account for the lifetime and electron-phonon coupling effects, respectively.

By integrating the spectral intensity over an energy interval of 100meV at Fermi level, we obtained the first experimental evidence of the Fermi surface plot.

Determination of electron spin polarization is an ultimate test of both the band calculations and our model of  $\text{Fe}_3\text{O}_4$  photoemission spectra. In our spin-resolved photoemission experiments 4.65 and 6.20 eV photons were used. The same sample was used as for spin-integrated ARPES, requiring its transfer through air to another chamber. It was not subject to any cleaning prior to the SRPES measurements that lead to a reduction of the spin polarization as a consequence of the presence of a dead layer on the surface. Nevertheless the spin polarization close to  $E_F$  reaches - 50% and -72% for 6.20 and 4.65 eV photons respectively. We conclude that  $\text{Fe}_3\text{O}_4$  can be described within a band model and in particular that it is half-metallic.

We also used femtosecond laser pulses in pump-probe experiments to investigate ultrafast dynamics on atomic scale. Our results show that the lifetime of excited electrons in  $\text{Fe}_3\text{O}_4$  is much longer than in an “ordinary” metal. From the spin analysis of excited electrons, we deduce that the demagnetization does not occur in the femtosecond range, which is compatible with half-metallic properties of magnetite.

# Résumé :

La magnétite ( $\text{Fe}_3\text{O}_4$ ) est un candidat prometteur pour des applications dans des dispositifs en spintronique. Ce ferrimagnétique avec une température de Curie élevée a été théoriquement prévu pour être un demi-métal avec un canal conducteur pour les spins minoritaire et un semi-conducteur pour les spins majoritaires, résultant en 100% de polarisation en spin au niveau de Fermi. Cependant, jusqu'à présent, aucune preuve expérimentale claire sur ce sujet n'a été faite.

Cette thèse présente des études en photoémission résolue en angle et en spin sur la structure électronique et magnétique de couches minces de  $\text{Fe}_3\text{O}_4$  (001) épitaxiées sur  $\text{MgO}$ (001). Un calcul de la structure de bande utilisant l'approximation du gradient généralisé (GGA + U) est proposé pour expliquer les résultats expérimentaux.

Bien que l'intensité de photoémission au niveau de Fermi soit très faible en raison du rôle joué par les polarons, une dispersion de la bande  $\text{Fe } 3d-t_{2g}$  est observée. Le comportement global de cette bande est en bon accord avec le calcul de la structure état électronique représentant état fondamental. Pour simuler les spectres de photoémission, nous avons utilisé l'approximation de l'électron libre à l'état final, tout en ignorant les éléments de matrice de la transition électronique. Dans la simulation, les bandes calculées sont convoluées respectivement par la lorentzienne et la gaussien pour tenir compte de la durée de vie et des effets de couplage électron-phonon.

En intégrant l'intensité spectrale sur un intervalle d'énergie de 100 MeV au niveau de Fermi, nous avons obtenu la première preuve expérimentale de la surface de Fermi.

Détermination de la polarisation de spin des électrons est un test ultime des calculs de bandes et des spectres de photoémission modélisés. Dans nos expériences de photoémission résolue en spin, nous avons utilisé des photons de 4.65 et 6.20 eV. Le même échantillon comme pour la photoémission intégré en spin a été mesuré, nécessitant son transfert par l'air dans une autre chambre. L'échantillon n'a pas été soumis à un nettoyage avant les mesures résolues en spin ce a conduit à une réduction de la polarisation en spin à cause de la présence d'une couche polluée sur la surface. Néanmoins, une polarisation de spin de - 50% et -72 % a été mesurée au voisinage de  $E_F$  respectivement pour les photons de 6.20 et de 4.65 eV. Nous en concluons que  $\text{Fe}_3\text{O}_4$  peuvent être décrits par un modèle de bande et en particulier qu'il est demi-métallique.

Nous avons également utilisé des impulsions femtoseconde laser dans une expérience pompe-sonde pour étudier la dynamique ultra-rapide à l'échelle atomique. Nos résultats montrent que la durée de vie des électrons excités dans  $\text{Fe}_3\text{O}_4$  est beaucoup plus longue que dans un métal «ordinaire». L'analyse de la polarisation en spin des électrons excités montre que la désaimantation ne se produit pas dans le domaine de la femtoseconde, ce qui est compatible avec des propriétés demi-métalliques de la magnétite.